THESIS

STRUCTURAL EVOLUTION OF THE POTOSÍ UPLIFT, SIERRA MADRE ORIENTAL, NORTHEASTERN MEXICO

Submitted by

Stewart Alexander Williams

Department of Geosciences

In partial fulfillment of the requirements

For the Degree of Master of Science

Colorado State University

Fort Collins, Colorado

Fall 2019

Master's Committee:

Advisor: John Singleton

John Ridley
Melinda Laituri

ABSTRACT

STRUCTURAL EVOLUTION OF THE POTOSÍ UPLIFT, SIERRA MADRE ORIENTAL, NORTHEASTERN MEXICO

The Jurassic Minas Viejas Formation is host to a Late Cretaceous to early Paleogene-aged décollement in the Sierra Madre Oriental, Mexico. The Minas Viejas Formation is dominated by rheologically-weak evaporite that accommodated thin-skinned deformation, forming the Sierra Madre Oriental fold-thrust belt with minimal deformation to the underlying Triassic-Jurassic red beds. Thin-skinned shortening above the décollement temporally transitioned to thick-skinned shortening, resulting in exhumation of the décollement and development of the Potosí uplift, one of the largest and well exposed thick-skinned uplifts in the orogen. Detailed geologic mapping and structural analysis provide insight into the geometry and kinematics of the Potosí uplift, and (U-Th)/He thermochronometry and vitrinite reflectance record the burial history and timing of exhumation associated with the uplift.

Thick-skinned deformation involved folding of sub-décollement strata into a NNW-SSE-striking anticlinorium, development of cleavage, ENE-WSW directed thrust faulting, conjugate strike-slip faulting, and formation of ENE-WSW-striking extension fractures associated with barite mineralization. These structures consistently record ENE-directed subhorizontal shortening. Shortening is directed ~062° in the southern part of the uplift and ~077° in the northern part of

the uplift. Thick-skinned deformation modified pre-existing geometries of thin-skinned folds involving Cretaceous overburden strata above the Jurassic evaporite décollement.

Zircon (U-Th)/He cooling dates (ZHe) and vitrinite reflectance data indicate that the entire evaporite décollement was buried to ≥185°C, consistent with development of phyllitic fabrics in the basal part of the Minas Viejas Formation. Paleocene to mid-Eocene zircon (U-Th)/He cooling dates in the Triassic-Jurassic red beds below the evaporite décollement directly record the timing of exhumation associated with thick-skinned deformation, and suggest that the thick-skinned uplift was a continuation of earlier thin-skinned shortening as opposed to a distinct tectonic event. A zircon (U-Th)/He date from the southern Potosí uplift is ~66 Ma, whereas ZHe dates in the northern part of the uplift range from ~49–43 Ma. Two samples from the nearby Aramberri uplift to the south of the Potosí uplift have mean ZHe dates of ~63–54 Ma.

The transition from thin- to thick-skinned shortening may be attributed to the evolution of mechanical stratigraphy in the décollement. Thin-skinned detachment folding resulted in significant migration of evaporite away from synclinal keels, effectively eliminating a planar weak zone at the base of the décollement and creating salt welds between carbonates or shales within the décollement with underlying red beds. The along-strike differences in timing of thick-skinned exhumation and the shortening directions may also be attributed to differences in mechanical stratigraphy. Thicker intervals of evaporite in the northern part of the uplift allowed thin-skinned shortening to continue while the southern part of the uplift transitioned to thick-skinned shortening as the weak evaporite décollement was exhausted. As a result, stress-strain trajectories in the northern part of the uplift refracted clockwise towards the area with more propagation of deformation.

Our findings provide a new insight into the geometry, kinematics, and timing of deformation associated with the Potosí uplift, and may provide a framework for studying other thick-skinned uplifts in the Sierra Madre Oriental, and more generally orogenic belts that record a transition in deformation styles.

ACKNOWLEDGEMENTS

First and foremost, unbelievably huge thanks to Dr. John Singleton, my advisor. He was an invaluable resource, a wealth of knowledge, and constantly pushed to make the project better. He taught me there were always more measurements to take to strengthen the dataset, and to strive to present the best possible product I could. His constant optimism was a necessary aspect to this project.

I thank my committee members, Dr. John Ridley and Dr. Melinda Laituri, for providing feedback on the thesis, elevating this project to a higher level through their experience and expertise.

I thank the Singleton Research Group, my dear friends Skyler Mavor, Nikki Seymour, and Mike Prior, for being examples of extraordinary geologists and for being wonderful friends.

Special thanks to Crossy for coming out and showing us around Mexico. He laid the foundations for this project and showed me just how wild evaporite structures can be.

I thank my field assistants, Blake Franklin, Mike Wyatt, and Oscar Vazquez, for joining me in the middle of Mexico to look at some rocks, get stung by cacti, and live amongst the goats for weeks at a time.

I thank Aliza Risby, my partner and anchor, for standing by me through thick and thin.

I owe thanks to the graduate students in the Department of Geosciences for providing me with valuable friendship and support.

And finally, this project wouldn't have been possible if not for the American Chemical Society Petroleum Research Fund's New Directions Grant.

DEDICATION

I dedicate this thesis to my sister, who has always been there for me.

TABLE OF CONTENTS

LIST OF TABLES

LIST OF FIGURES

INTRODUCTION

In contractional settings, salt horizons or evaporite layers commonly form décollements and may play a critical role in the development of a fold-thrust belt. The unique rheologic properties of evaporites allow for not only decoupling between underlying and overlying units, but also allow flow into detachment folds that form with progressive contraction (Davis and Engelder, 1985). While this general concept is well understood, few field studies have addressed the distribution or localization of strain within a ductile evaporite décollement. A major factor in the lack of study is that good surficial exposures of evaporite décollements and sub-décollement rocks are rare.

In some orogens thin-skinned fold-thrust belts involving an evaporite décollement progressed to a new deformational regime or underwent a secondary shortening event. The Zagros Mountains in Iran (Lacombe and Bellahsen, 2016) and the Jura Mountains in the Swiss-French Alps (Jordan, 1992; Lacombe and Bellahsen, 2016) are notable examples of thin-skinned fold-thrust belts associated with an evaporite décollement that were temporally synchronous with or transitioned to thick-skinned shortening involving subdécollement rocks. In cases like these, one could potentially study not only the décollement itself, but also the overlying and underlying strata with the goal of understanding the evolution of contractional deformation associated with either a progressive transition in contractional style or two different contractional events within the same region.

The Potosí uplift in northeastern Mexico is located within the Sierra Madre Oriental orogen (Figure 1). Thin-skinned development of a fold-thrust belt was accommodated by a

décollement within a Jurassic evaporite sequence. This décollement was later exhumed by thick-skinned uplift which resulted in exposure of sub-décollement Triassic-Jurassic red beds.

This project addresses the structural evolution of the Potosí uplift. The main research questions include:

1) How was deformation distributed through the evaporite décollement?
2) What are the kinematics of both the thin-skinned shortening and the thick-skinned uplift?
3) What are the structures associated with the thin-skinned shortening and the thick-skinned uplift events?
4) When did these events occur, and was there a progressive transition from thin-skinned to thick-skinned deformation, or are they two distinct events?
5) What caused the shift in deformation style?
6) How does the Potosí uplift compare to other thick-skinned uplifts within the Sierra Madre Oriental?

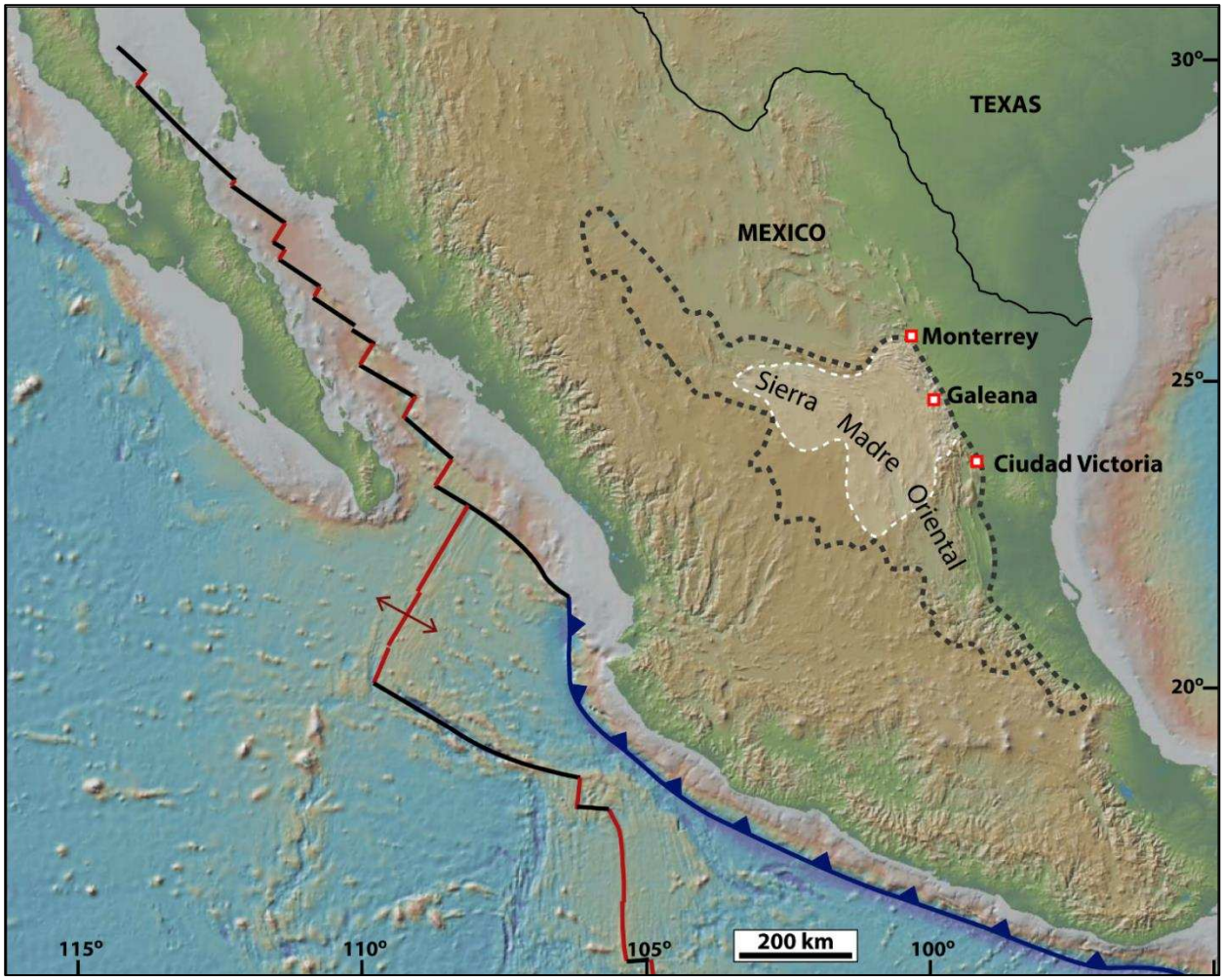

Figure 1. Shaded relief map of Mexico (from GeoMapApp, www.geomapapp.org). Highlighted is the Sierra Madre Oriental within the black dotted outline. Within the white dashed outline is the extent of Minas Viejas Formation evaporite found within the Sierra Madre Oriental. Notable locations are shown: Monterrey, Galeana, and Ciudad Victoria. Also annotated is the current plate boundary orientations on the western coast, with transform faults shown in black, spreading ridges in red, and subduction zone boundaries in blue.

GEOLOGIC BACKGROUND

1. Thin-skinned Shortening

The development of the Sierra Madre Oriental fold-thrust belt in northeastern Mexico was a result of Late Cretaceous to Paleogene E- to NE-directed shortening. Though previous studies have equated this shortening with the Laramide orogeny (Campa, 1985; Eguiluz de Antuñano et al., 2000; Gray et al., 2001; Marrett and Aranda-García, 2001; Zhou, 2005; Cuéllar-Cárdenas et al., 2012), differences in timing (Lawton et al., 2009; Gray and Lawton, 2011; Fitz-Díaz et al., 2016; Ramírez-Peña and Chávez-Cabello, 2017), deformation styles (Dickinson and Snyder, 1978; Yonkee and Weil, 2015), and tectonic influences (Liu et al., 2010) suggest that the Sierra Madre Oriental should be classified as its own tectonic entity separate from the Laramide orogen (Fitz-Díaz et al., 2017). The Sierra Madre Oriental developed primarily as a thin-skinned fold-thrust belt, characterized by a subhorizontal décollement kinematically linked with low-angle thrust faults and folds in Jurassic and Cretaceous marine strata. The orogen is ~1,000 km long and up to ~400 km wide (Marrett and Aranda-García, 2001; Fitz-Díaz et al., 2017). In the central part of the Sierra Madre Oriental regional-scale folding developed above a décollement within Upper Jurassic evaporites in the Minas Viejas Formation. The Minas Viejas Formation is 800–1,500 m thick (Marrett and Aranda-García, 2001; Cross, 2012) and composed predominantly of Ca-sulphate as gypsum near the surface and anhydrite at depth, interbedded with carbonates. This décollement formed in shales or carbonates at similar stratigraphic levels farther west and south (Tardy et al., 1975; Gray et al., 2001; Marrett and Aranda-García, 2001; Zhou, 2005; Barboza-Gudiño et al., 2012), but the thinned-skinned deformation in these parts of

the orogen was much more dominated by gently-dipping thrust faults, highlighting the importance of the Minas Viejas Formation in the development of fold structures (Figure 2) (Marrett and Aranda-García, 2001). The rheologically weak evaporite intervals were ideal for the formation of a thin-skinned décollement allowing for extensive detachment folding in overlying Jurassic-Cretaceous strata. The fold-thrust belt above the evaporite décollement is comprised primarily of upright horizontal, tight to isoclinal folds. Typical fold amplitudes within the overburden Cretaceous strata are 2–3 km, and wavelengths are 5–6 km (Padilla y Sánchez, 1985; Ramírez-Peña and Chávez-Cabello, 2017). Horizontal shortening estimates within the fold-thrust belt ranges from 20% to 57% (Padilla y Sánchez, 1985; Marrett and Aranda-García, 2001). The Monterrey Salient, estimated to have undergone 33% shortening, developed the arcuate orogenic front of the Sierra Madre Oriental as a result of a mechanically weaker wedge compared to areas where evaporite is thinner or not present (Figure 3) (Marrett and Aranda-García, 2001). The formation of the prominent evaporite décollement allowed for minimal-to-no deformation in the underlying Triassic sandstone red beds or Paleozoic/Precambrian basement rocks (Marrett and Aranda-García, 2001).

Timing of deformation in the Sierra Madre Oriental varies regionally and remains disputed, ranging from 93–40 Ma (Lawton et al., 2009; Fitz-Díaz et al., 2016, 2017; Centeno-García, 2017; Ramírez-Peña and Chávez-Cabello, 2017). Near Saltillo, deformation is thought to have initiated ~92 Ma based on syn-orogenic sedimentary rocks displaying growth strata (Vega-Vera et al., 1989; Ocampo-Díaz et al., 2016) and ended ~71.5 Ma based on post-tectonic pluton emplacement (Ramírez-Peña and Chávez-Cabello, 2017). $^{40}Ar/^{39}Ar$ illite dating of gouge along flexural slip surfaces suggests that folding near Monterrey occurred between ~56–46 Ma (Fitz-

Díaz et al., 2016). Fitz-Díaz et al. (2017) interpret the discrepancy between published studies to record regional differences in the timing of shortening, where the oldest deformation initiated to the southwest and progressed northeastward as the Sierra Madre Oriental matured.

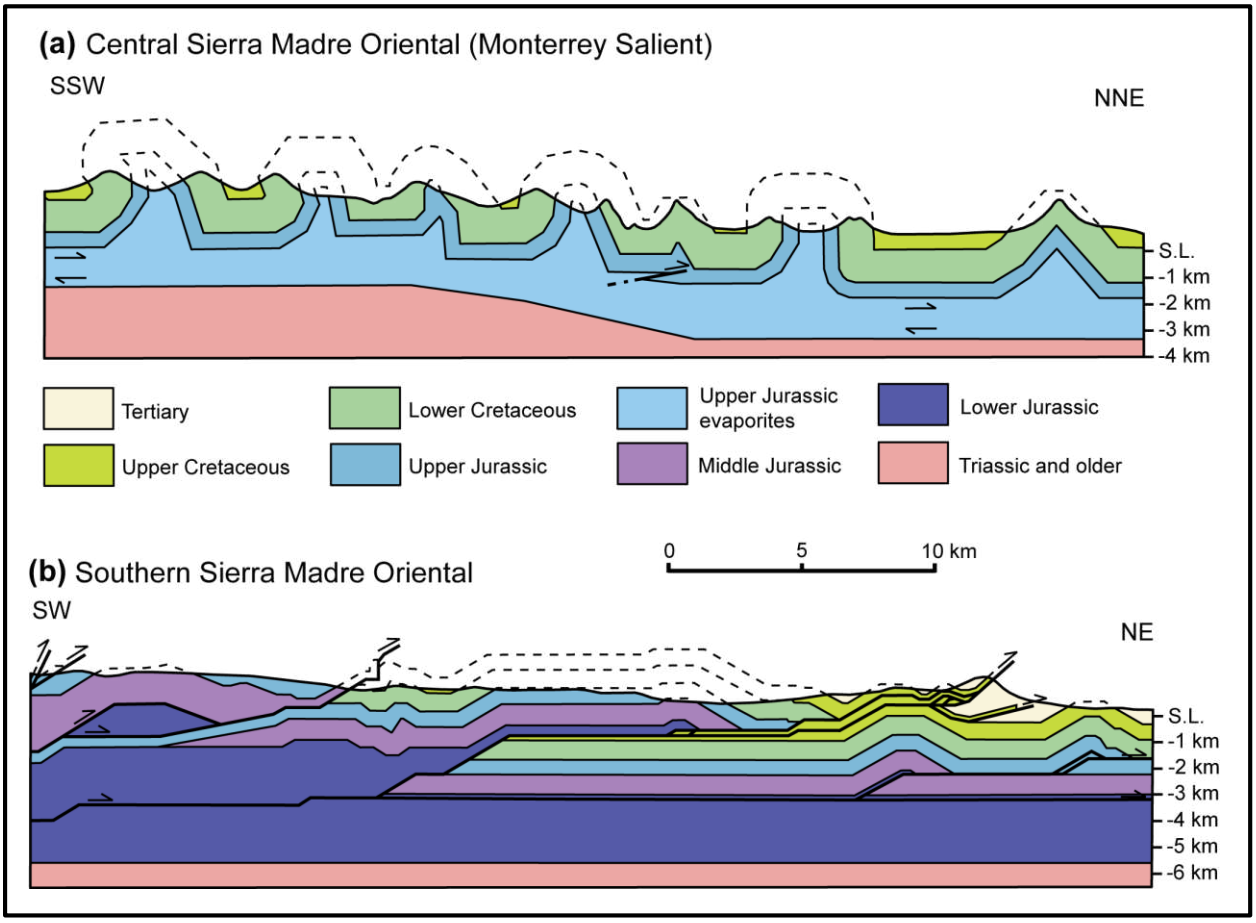

Figure 2. Fold styles within the Sierra Madre Oriental. Where evaporites were present, symmetrical box-folds formed with minimal thrust faults as a result of a ductile décollement, evident in the Monterrey Salient. To the west and south of the Monterrey Salient, a lack of evaporite resulted in brittle thrust fault complexes. Figure from Marrett and Aranda-García (2001); Cross (2012). Constraints on cross-section geometries at depth are not expanded upon.

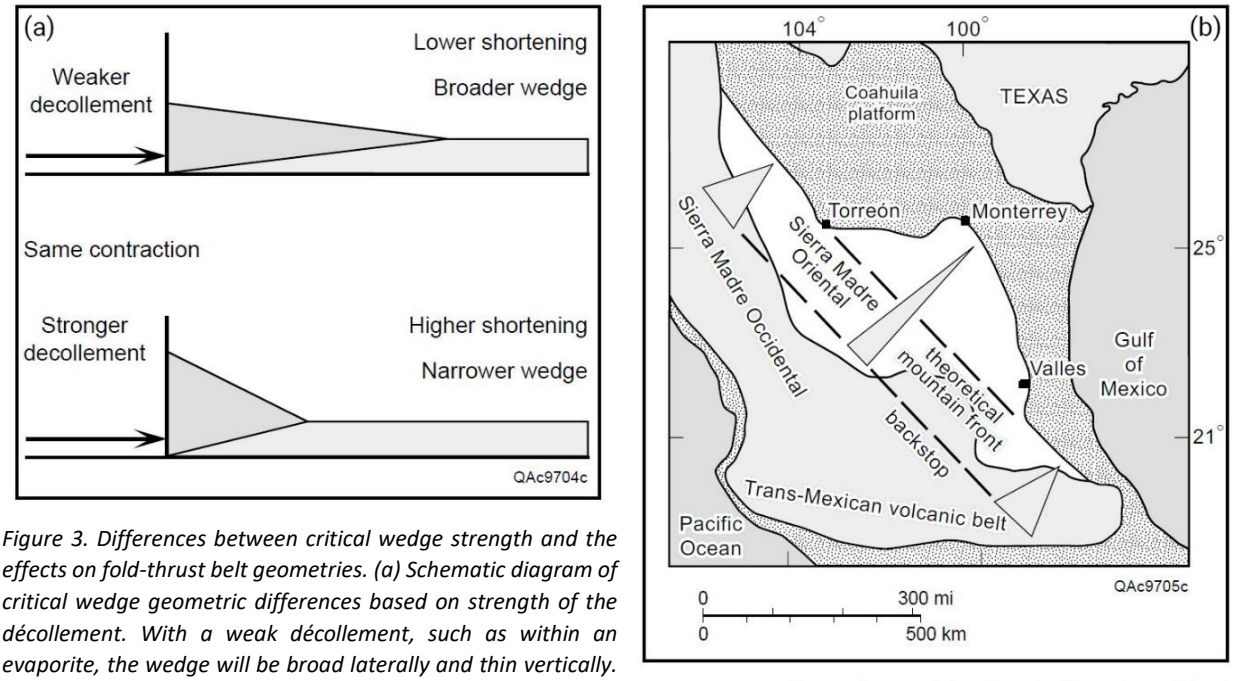

Figure 3. Differences between critical wedge strength and the effects on fold-thrust belt geometries. (a) Schematic diagram of critical wedge geometric differences based on strength of the décollement. With a weak décollement, such as within an evaporite, the wedge will be broad laterally and thin vertically. With a strong décollement, such as with siliciclastics or igneous rocks, the wedge will be vertically thick and laterally thin. It is due to this concept that basement-involved shortening typically results in large magnitudes of exhumation while thin-skinned sedimentary decollements results in laterally extensive fold-thrust belts but not a large magnitude of exhumation. (b) The result of critical wedge strength differences within the Sierra Madre Oriental. As a result of the evaporite extent, the Monterrey Salient developed from a weak décollement resulting in a broad lateral reach. Figure from Marrett and Aranda-García (2001).

2. Thick-skinned Uplift

Exposure of décollements and sub-décollement strata worldwide are rare due to a lack of exposure, typically from tectonic thickening of overlying strata. While overburden structures associated with a décollement can be studied, the décollement itself is usually is buried at depth (Fletcher and Gay, 1971). Given the solubility of evaporites, exposures commonly lack high-quality outcrops. In the Sierra Madre Oriental, however, multiple thick-skinned uplifts throughout the fold-thrust belt have exhumed the décollement along with underlying Triassic-Jurassic sandstone “red beds” and/or Paleozoic/Precambrian basement. Most notable examples are the Potosí uplift (Götte, 1988; Huízar-Alvarez and Oropeza-Orozco, 1989; Davis, 2005; Cross, 2012; Fitz-Díaz et al., 2017), Huizachal-Peregrina Anticlinorium (Zhou, 2005; Rubio-Cisneros and

Lawton, 2011), Sierra de Catorce uplift (Barboza-Gudiño et al., 2012), San Julian uplift (Anderson et al., 1991; Reid and Marrett, 2002), and the Aramberri uplift (Meiburg et al., 1987). Given these exposures (Figure 4), correlations across the Sierra Madre Oriental can be made involving the stratigraphic level of the thin-skinned décollement, underlying and overlying strata, and associated structures.

The timing, kinematics, and geometries of these thick-skinned uplifts have not been extensively studied. It is clear that thick-skinned deformation postdated thin-skinned shortening given that the décollement has been uplifted several kilometers above the expected regional levels in some areas (Zhou, 2005; Cross, 2012). Previous researchers suggest that high-angle reverse faults bound the uplifts, which may represent reactivated normal faults associated with the opening of the Gulf of Mexico, prior to or coeval with Triassic-Jurassic "red bed" deposition (Götte, 1988; Davis, 2005; Zhou, 2005; Cross, 2012). If this were the case, stratigraphic relationships and detailed structural mapping would yield evidence of high-angle faults along the margins of the thick-skinned uplifts. The basement uplift of the Huizachal-Peregrina anticlinorium, located West of Ciudad Victoria in the state of Tamaulipas and extensively studied by Zhou (2005), Zhou et al., (2006), and Rubio-Cisneros and Lawton (2011) is a well-known example a thick-skinned uplift likely associated with tectonic inversion. The Huizachal-Peregrina anticlinorium exposes Triassic-Jurassic rift-basin deposits of the La Boca and La Joya Formations, forming the Huizachal Group, overlying Paleozoic (meta)sedimentary rocks and Precambrian crystalline basement (Rubio-Cisneros and Lawton, 2011). Prior to thick-skinned uplift, thin-skinned shortening associated with a detachment between the Huizachal Group and the overlying Upper Jurassic Zuloaga Limestone Formation formed detachment folds with a typical

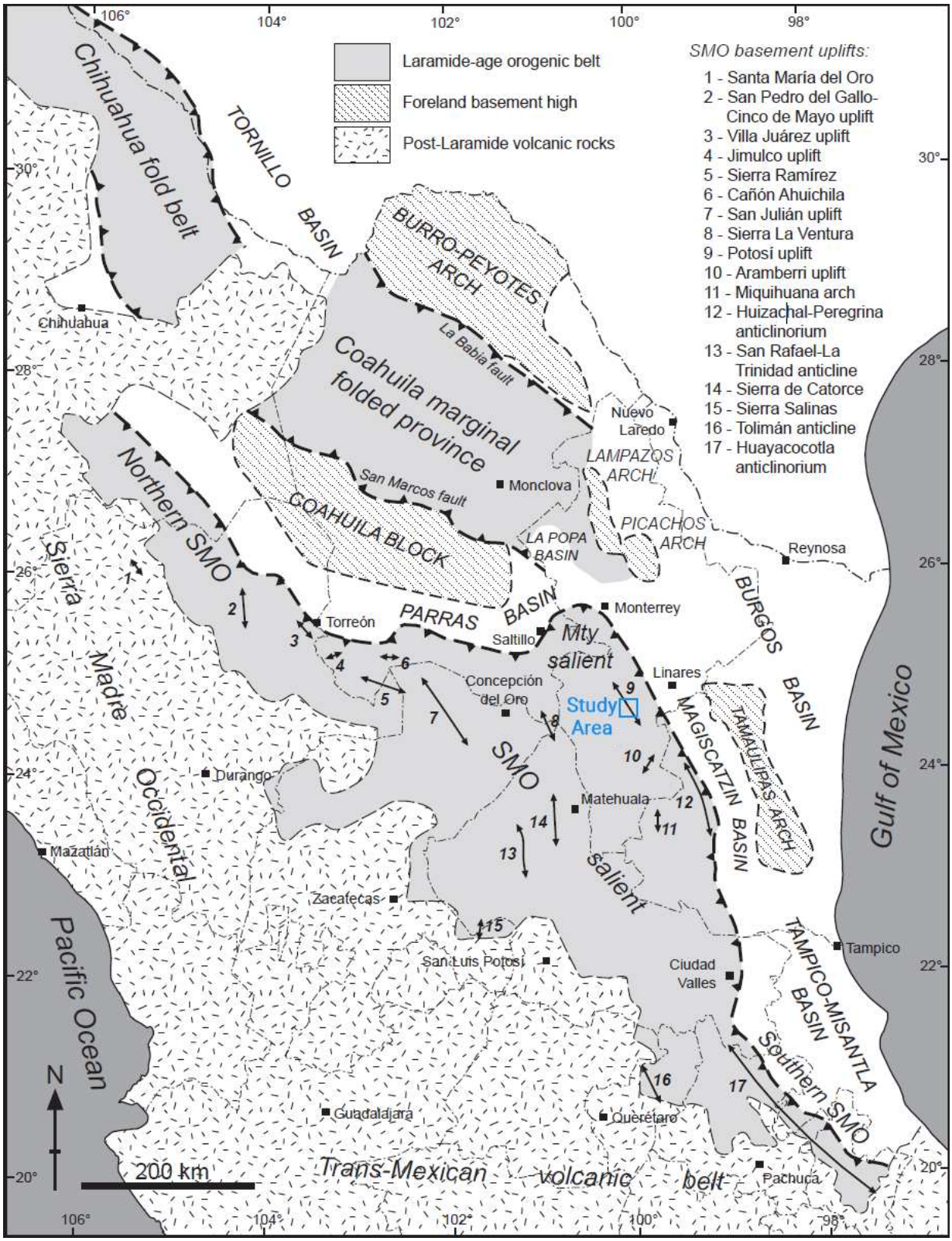

Figure 4. Thick-skinned uplifts found within the Sierra Madre Oriental. The project study area is highlighted in blue. Arrows identify overall trends of thick-skinned uplifts. Modified from Cross (2012), containing data from multiple previous studies. See Fig 1.7 of Cross (2012) for complete list of studies.

wavelength of ~3.3 km (increasing away from the uplift), which were accommodated by bedding-parallel slip and thrust faults with ramp-flat geometries (Zhou et al., 2006). Subsequent thick-skinned deformation exhumed Mesozoic sedimentary strata and lifted the detachment to ~3–4 km higher than the surrounding regional levels. Zhou et al. (2006) suggest that uplift occurred via reactivation of pre-existing normal faults within the basement as high-angle reverse faults. Though not exposed, interpreted orientations of rift-related normal faults would fit the orientations of the hypothesized reverse faults given the trend of the anticlinorium (Zhou et al., 2006).

3. The Potosí Uplift

This study focuses on the core of the thick-skinned Potosí uplift, also known as the Galeana uplift, located ~100 km south of Monterrey, Nuevo Leon, Mexico (Figure 4, 5). The Potosí uplift includes exposures of the fold-thrust belt involving Cretaceous "overburden" strata, a thick Jurassic evaporite and carbonate sequence within the Minas Viejas Formation, which acted as the décollement during thin-skinned shortening, as well as exposure into the sub-décollement Triassic-Jurassic red beds. Red bed exposures within the core of the uplift occur as isolated windows through the Minas Viejas Formation in a NNW-SSE trend (Plate 1). These exposures span ~36 km parallel to the trend, and ~9.5 km wide perpendicular to the trend (Plate 1). Given the large amount of sub-décollement exposure, the Potosí uplift offers a unique opportunity to investigate the kinematics, timing, and structural style of thick-skinned uplift within a dominantly thin-skinned orogen.

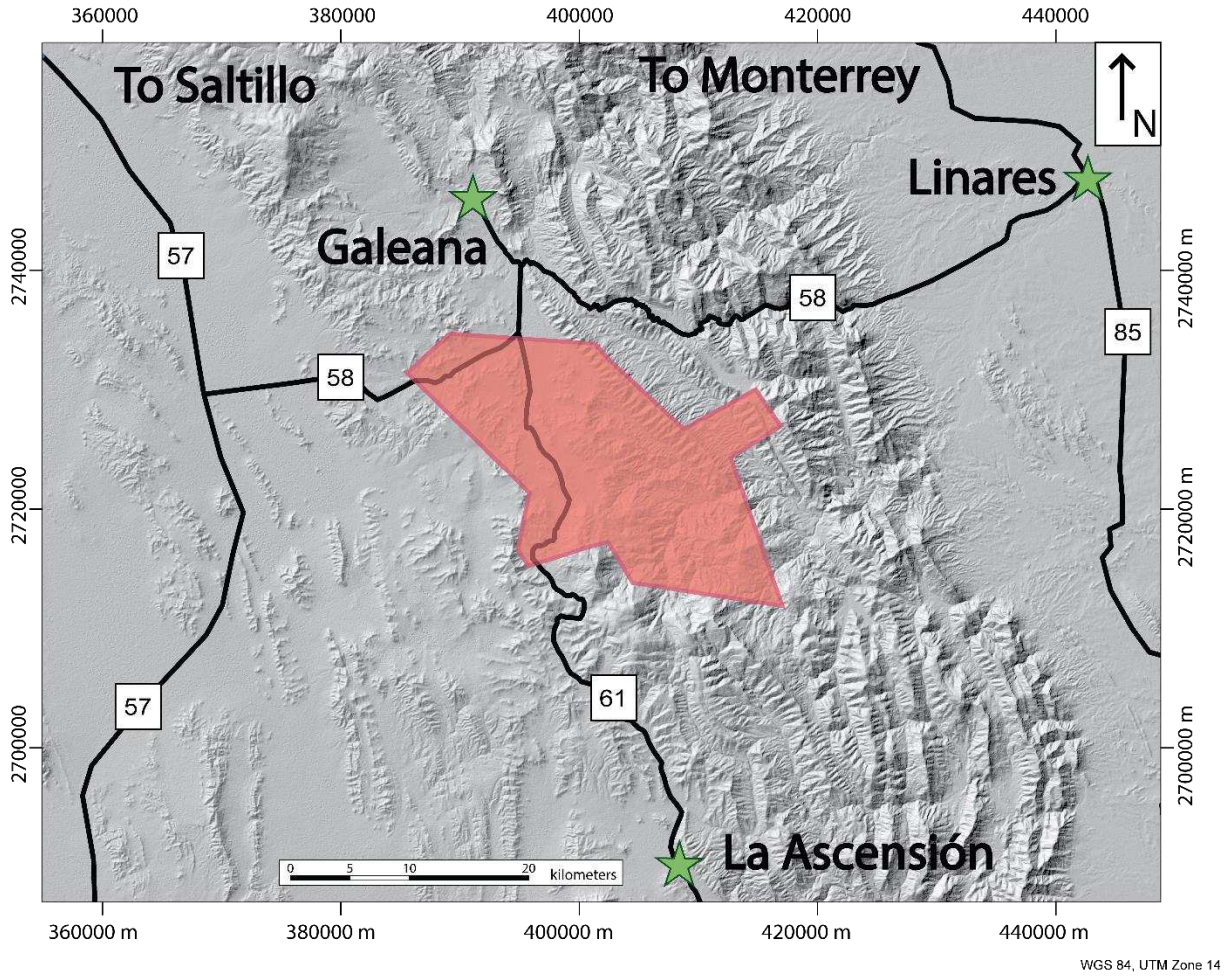

Figure 5. The study area highlighted in red, highways in blue. Major cities and towns are marked by green stars, being Galeana, La Ascensión, and Linares. To road to the northeast leads to Monterrey, northwest to Saltillo.

Previous work in the area includes detailed stratigraphic studies of both the sub-décollement Triassic-Jurassic red beds (Mixon, 1963; Belcher, 1979; Michalzik, 1991; Barboza-Gudiño et al., 2010), as well as the Jurassic evaporite (Götte, 1990; Cross, 2012) and the various Jurassic-Cretaceous overburden formations (Ocampo-Díaz et al., 2008). Several structural studies have also been conducted (Padilla y Sánchez, 1978, 1985; Moor, 1980; Götte, 1988; Kroeger and Stinnesbeck, 2003; Laubach and Ward, 2006; Cross, 2012), but these studies have not addressed the structures, kinematics, and timing of thick-skinned deformation in detail.

Padilla y Sánchez (1985) previously conducted a broad-scale study of the Monterey salient, including the northern part of the Potosí uplift, focusing on Jurassic-Cretaceous overburden fold structures. Götte (1988) mapped the Galeana area at 1:50,000-scale and created multiple cross sections, highlighting key structures in the uplift. Davis (2005) conducted reconnaissance structural mapping (1:50,000-scale) in the Tranquitas area (Plate 1), which was further studied in detail and mapped at 1:10,000-scale by Cross (2012). The Servicio Geológico Mexicano (SGM, 2010b, 2010c) conducted broad-scale regional mapping encompassing the entire study area at 1:50,000-scale.

Previous studies have proposed that the broad "Potosí anticline" forms the Potosí uplift (Padilla y Sánchez, 1978; Moor, 1980), Subsequent studies suggest that the Potosí uplift is structurally controlled by high-angle reverse faults (Götte, 1988; Cross, 2012), similar to the Huizachal-Peregrina uplift to the southeast, or formed as a horst flanked by two extensional grabens (Padilla y Sánchez, 1985). Götte (1988) mapped the eastern boundary of the uplift as a high-angle, west-dipping reverse fault within the town of Galeana, adjacent to a large down-dropped graben. Cross (2012) calculated that the uplift bounding reverse fault has a net vertical offset of at least 3.1 km. Cross (2012) also inferred a similar structure on the western flank with net vertical offset of at least 1.9 km. A cross-section by Fitz-Diaz et al. (2017) using data from Chávez-Cabello (unpublished) interpreted the uplift to be bound by a W-dipping normal fault on the west side and a W-dipping reverse fault on the east side. Mapping conducting by Servicio Geológico Mexicano (SGM, 2010b, 2010c) suggests the Potosí uplift was the result of extensive folding within the red beds, potentially associated with blind high-angle, ENE-vergent reverse faults.

Apart from the inferred graben near Galeana (Götte, 1988), the study area and surrounding region does not contain any other known normal fault-bound Cenozoic basins, and is considered to be outside of the Mexican extent of the Basin and Range province (Stewart, 1998). While the study area is located too far south to be associated with the Río Grande Rift, it is relatively proximal to the accepted boundary of the Chihuahua and Mexican Altiplano region, an area of relatively small-magnitude extension (Stewart, 1998). It is possible that Cenozoic extensional features associated with the Basin and Range province could be observed within the study area as smaller-scale structures.

Triassic-Jurassic red beds in the Potosí uplift commonly host large barite veins. Many of the larger veins have been mined, comprising the Galeana Barite District (Kesler et al., 1988; Kroeger and Stinnesbeck, 2003). Barite mineralization follows structural controls, commonly observed as large extension opening-mode fractures, most often striking E-W to NE-SW (Kesler et al., 1988). These fractures can rarely be traced into the overlying Jurassic evaporite, which typically lacks even minor brittle deformation. Using strontium/rubidium isotopic ratios of the barite, the Jurassic evaporite, and underlying Triassic red beds, Kesler et al. (1988) suggest that mineralization occurred at roughly ~30 Ma as a result of fluid mixing between the Jurassic evaporite and Triassic red beds.

Multiple phosphorite, lead, zinc, gold, and silver mines can also be found in the study area, though the dominant resource is barite, making up 35 of 47 of the recorded mines within the study area as of 2010 (SGM, 2010b, 2010c). Of the remaining 12 mines, 5 are phosphorite mines, 2 are Pb/Zn/Ag mines, 1 is a Pb/Zn/Au mine, 2 are shale quarries, and 1 is a gypsum quarry.

METHODS

4. Geologic Mapping of the Potosí Uplift

The Potosí uplift was mapped at 1:20,000-scale across an area of 394 km^2 by the primary author over the span of 6 non-consecutive weeks, from July 2017 to October 2018. Each visit included a different combination of field assistants, including the primary advisor, Dr. John Singleton, a postdoctoral assistant also studying the Potosí uplift, Dr. Michael Prior, a fellow graduate student in the Singleton Research Group, Skyler Mavor, recent Colorado State University (CSU) graduates, Michael Wyatt and Blake Franklin, CSU undergraduate Omar Gomez, and recently graduated University of Nevada – Las Vegas student, Oscar Vazquez. Gareth Cross, who had previously studied the stratigraphy and structures of the Jurassic Minas Viejas Formation in the northern study area (Cross, 2012), accompanied the author on the first trip to assist with identification of geologic units and the structural style of deformation in the décollement.

Geologic contacts, all measurements, and sample locations were recorded on Garmin Oregon 650t or Garmin eTrex 20x handheld GPS devices, which typically have ~3–4 m accuracy. The orientations of structures, nature of contacts, outcrop characteristics, mineralization, etc., were recorded in field notebooks and tied to a GPS waypoint. These data, in conjunction with aerial imagery provided by Esri (2017), were then used to create the geologic map with Esri's *ArcMap* software. This software was also used to create custom topographic basemaps from global DEMs. Finally, the map was imported into *Adobe Illustrator* for final touches, including

label placement, polygon opacity, and symbol adjustments. *Adobe Illustrator* was also used in creating cross sections.

5. Geometric and Kinematic Analysis

Structural measurements were analyzed in Rick Allmendinger's (2019) *Stereonet* and/or *Faultkin* software programs. Measurements were sorted and analyzed based on age of formations, distinguishing the Triassic-Jurassic red beds, the Jurassic Minas Viejas Formation, and the Jurassic-Cretaceous formations which overlie the décollement. Measurements from the Triassic-Jurassic red beds were then further separated into distinct geographic locations to evaluate how thick-skinned deformation varied across the NNW-SSE-trending uplift.

Measurements of bedding and foliation orientations were supplemented from Cross (2012) with 66 measurements of the Triassic-Jurassic El Alamar Formation and 14 measurements of foliation within the La Nieve Member shear zone, and 39 measurements of bedding across all strata from the Servicio Geológico Mexicano (SGM) (2010a, 2010b). Due to space constraints, only 35 of the 66 El Alamar Formation bedding measurements from Cross (2012) are present on the produced geologic map (Plate 1).

Planar structural measurements are presented in the following format: right-hand rule strike°/dip°, e.g. “125°/14°”, a plane striking 125° and dipping 14°. Linear structural measurements are presented in the following format: trend°, plunge°, e.g. “028°, 55°”, a line trending 028° and plunging 55°.

Bingham axial distributions are calculated through the *Stereonet* program (Allmendinger, 2019). This calculation determines the cylindrical best fit of axial density within a specific dataset,

outputting eigenvalues (magnitude) and eigenvectors (axes orientations) (Allmendinger et al., 2011). Eigenvalues are commonly denoted by: ' λ_1 , λ_2 , λ_3 ' (Vollmer, 1990), though are output in the *Stereonet* as: E_1 , E_2 , E_3 , with the eigenvalue magnitudes adding up to 1.0000. Eigenvectors output as three perpendicular lines with trend and plunge orientations representing the principal axes of a tensor, in this case looking at measurement vectors and their distributions (Allmendinger et al., 2011). Eigenvectors can then be used to interpret the orientations of fold axes (E_3) and the mean orientations of structures such as bedding, cleavage, foliation, etc. (E_1). Eigenvalues can further be used to calculate PGR values, or Point, Girdle, and Random values (Vollmer, 1990), using the following equations:

$$P = E_1 - E_2$$

$$G = 2(E_2 - E_3)$$

$$R = 3(E_3)$$

PGR values are a classification scheme with 3 end-members, often displayed as a ternary diagram, to describe the distribution and spread of data within a stereonet. High point (P) values indicate a single dominant orientation, or a high point maxima; high girdle (G) values indicate a spread of points along a plane; and high random (R) values indicate a non-systematic spread of data. These values can be used to identify structural patterns and consistency of orientations.

6. Analysis of Burial and Exhumation History

6.1. (U-Th)/He Thermochronometry

This study was part of a joint effort to research the Potosí uplift, with an additional component of research focusing on low-temperature thermochronometry to constrain timing of

uplift, led by Dr. Michael Prior. Samples were collected in conjunction with field work in the study area on an uplift-parallel transect within exposures of Triassic-Jurassic red beds, Jurassic Minas Viejas Formation, and Jurassic-Cretaceous La Casita Formation for (U-Th)/He zircon analysis. In addition, two samples were collected from subdécollement rocks in the Aramberi uplift, ~55 km south of the study area. The (U-Th)/He thermochronometric system is based on the retention of radiogenic helium within the mineral lattice, which is dependent on the thermal history of the sample. Results can then be used to interpret an exhumation history of the region. For the purposes of this study, a simplified concept of closure temperature will be applied (Dodson, 1973). The zircon closure temperature is typically ~180–190°C assuming a standard grain size of ~60–100 µm (Reiners et al., 2002, 2004; Wolfe and Stockli, 2010). Analyses were done at the University of Texas at Austin on 6 samples from the Potosí uplift and two samples from the nearby Aramberri uplift to the south of the study area for a total of 44 zircon single-grain aliquots from a total of 8 samples. The zircon (U-Th)/He date for each sample is reported as the mean of 4 to 5 individual aliquot dates with a 2 standard error. Standard error is chosen over standard deviation as standard deviation measures variability regardless of distribution, while standard error is the reproducibility of the mean, taking distribution patterns into account and not simply range of distribution (Altman and Bland, 2005). Overall, forty-four zircon single-grain aliquots from a total of 8 samples were analyzed. See Prior et al. (2016) for detailed analytical methods.

6.2. Vitrinite Reflectance

An organic-rich shale interval found within the Jurassic Minas Viejas Formation was analyzed for vitrinite reflectance, a metric which determines thermal maturity based on

maximum temperature (Barker and Pawlewicz, 1994; Bird et al., 1999; Cardott, 2012). This metric may constrain the maximum temperature achieved through burial at that specific structural level, assisting in the interpretation of burial temperatures for the underlying and overlying strata when used in conjunction with a geothermal gradient. Burial temperature calibrations are variable in published studies and there is no widespread accepted calibration of vitrinite reflectance values and temperatures that is used by a large majority of academic or industry entities. For the use of this study, temperatures and the correlative vitrinite reflectance values will be based on Barker and Pawlewicz (1994). Analysis was conducted by National Petrographic Service Inc.

STRATIGRAPHY

The Potosí uplift contains exposures of Triassic-Jurassic fluvial red beds, Jurassic evaporite and carbonates, and Jurassic-Cretaceous marine shales and carbonate platform sequences that make up the prominent fold-thrust belt exposed through the Sierra Madre Oriental. Crystalline basement is not exposed in the study area, but based on exposures near Aramberri ~55 km south of the Potosí uplift, Paleozoic and Precambrian basement most likely underlies the Triassic-Jurassic red beds. This basement is composed of low-grade metamorphic rocks, including phyllite, metagraywacke, and meta-diabase (Meiburg et al., 1987). Stratigraphic descriptions in the following section are ordered from oldest to youngest and are present in a simplified stratigraphic column (Figure 6).

7. Upper Triassic El Alamar Formation

The stratigraphically-lowest exposures in the study area consist of mudstone, sandstone, and conglomerate of the Upper Triassic El Alamar Formation. These siliciclastic strata were deposited by continental fluvial systems, evident by both in-depth facies analysis (Barboza-Gudiño et al., 2010) and the presence of abundant petrified logs. The formation is characterized by red-brown to dark red color (Figure 7), but it often appears tan or light brown as well on more weathered surfaces. Fine-grained siliciclastics (siltstone and shale) within the El Alamar Formation commonly have cleavage oriented at a high angle to bedding. Sandstone within the formation ranges from fine-grained to coarse-grained lithic and feldspathic arenites. Historically, this succession of red beds has been named the La Boca Formation or the Huizachal Group.

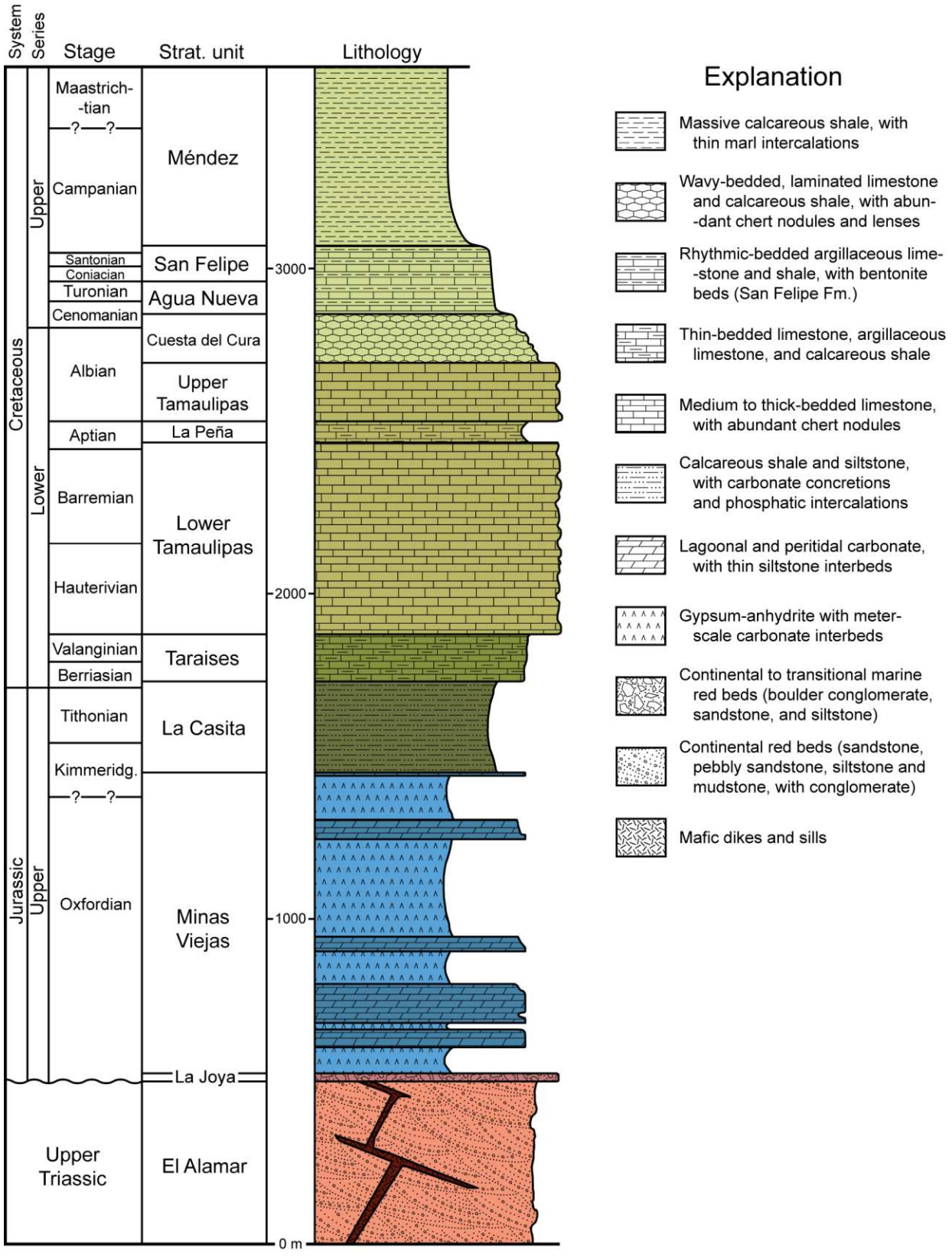

Figure 6. Simplified stratigraphic column of all units exposed within the study area of the Potosí uplift, figure modified from Cross (2012). *See Cross (2012) for full list of sources.*

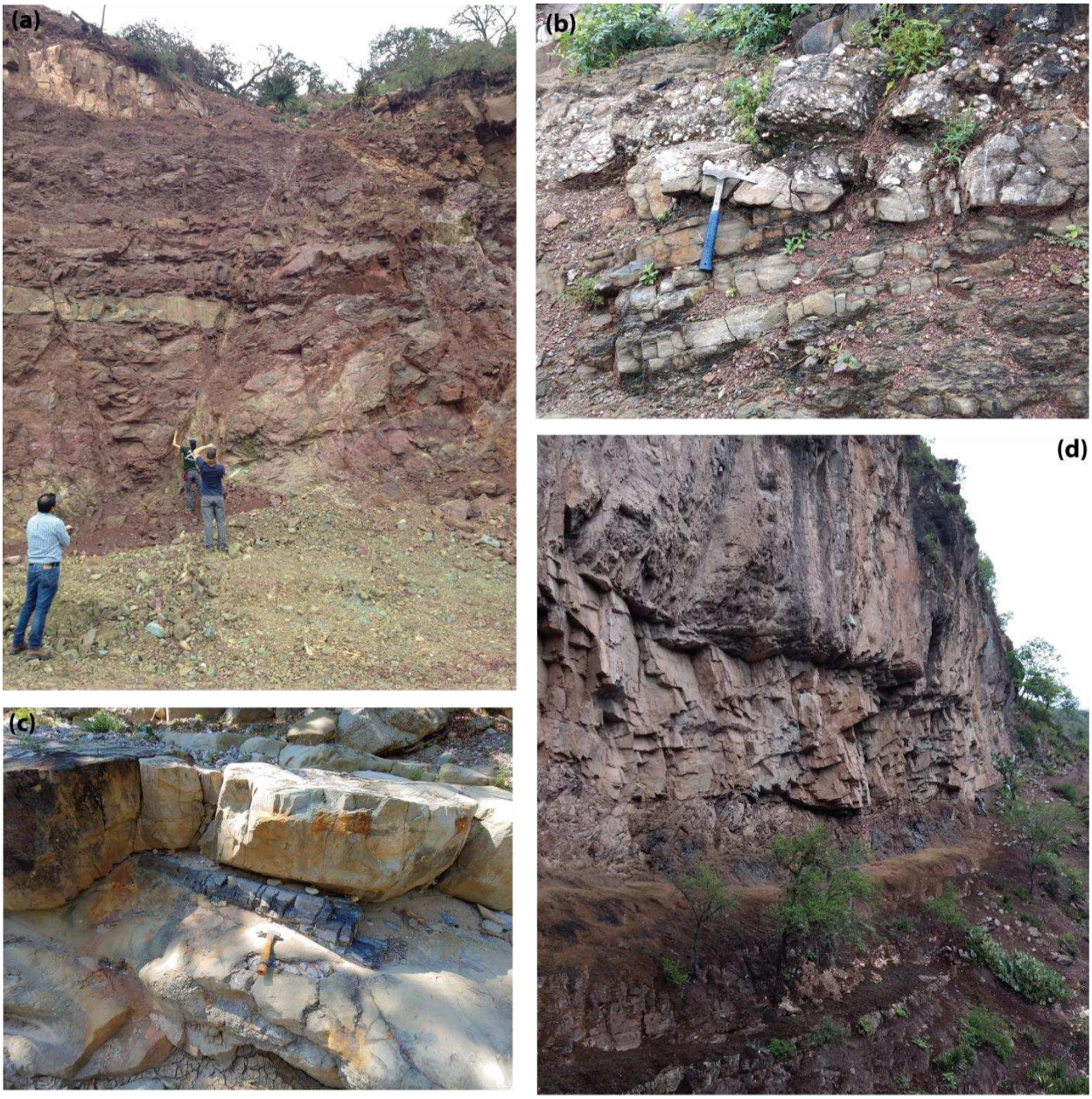

Figure 7. Outcrop styles of Upper Triassic El Alamar Formation. (a) Exposure of the El Alamar Formation in Tranquitas at an active barite mine. The formation exhibits evidence of abundant fluid mobilization and alteration resulting in copper and sulfide mineralization (pyrite, chalcopyrite, malachite), and host rock has developed a "waxy" texture. (b) Internal stratigraphy within the El Alamar Formation includes varying grain-size lithologies as well as abundant angular unconformities, rock hammer for scale. (c) Petrified logs within the El Alamar Formation in Cañón El Alamar with characteristic tan and brownish-red coloring, rock hammer for scale. (d) Blocky nature of outcrops along cliff and canyon walls in Cañón El Alamar. This stratigraphic interval is characteristic of the upper-most section of the El Alamar Formation and is found on both the east and west side of Cañón El Alamar. See Plate 1 for locations.

Several studies indicate that the El Alamar Formation is both different in age and composition to the La Boca Formation or Huizachal Group located elsewhere in the Sierra Madre Oriental (Mixon, 1963; Belcher, 1979; Michalzik, 1991; Barboza-Gudiño et al., 2010). Detrital zircon U-Pb analysis by Barboza-Gudiño et al. (2010) yielded a maximum depositional age of 230–225 Ma based on ~100 grains analyzed (with only 3 grains between 237 and 209 Ma), suggesting the El Alamar Formation is Late Triassic in age and older than then La Boca Formation and Huizachal Group. The proposed type locality of the El Alamar Formation is located within the study area along Cañón El Alamar near Río de San José (Plate 1).

8. Upper Jurassic La Joya Formation

The Upper Jurassic La Joya Formation, where present, can be up to 65 m thick (Cross, 2012), though is usually either not present, unexposed, or <2 m thick. The La Joya Formation contains clast-supported pebble- to cobble-sized conglomerates, typically fining upwards, with interbeds of medium- to coarse-grained lithic and feldspathic sandstones (Figure 8). The La Joya Formation unconformably overlies the Triassic El Alamar Formation. Conglomerate clasts are sub-rounded to sub-angular and appear to be derived primarily from the Triassic El Alamar Formation.

The La Joya Formation is not regionally continuous, appearing only at certain localities. One of the most prominent exposures of La Joya Formation is in the northern part of the Potosí uplift, near the community of Tranquitas (Plate 1). This area was previously mapped by Cross (2012), who noted a 5°–15° angular unconformity between the La Joya Formation and the

Figure 8. Outcrop of the Upper Jurassic La Joya Formation, located northwest of Cañón El Alamar (Plate 1). The conglomeratic lithology and typical dark-brown-red coloration is characteristic of the La Joya Formation, pencil for scale. Conglomerate clasts are identical to sandstone intervals found within the underlying Upper Triassic El Alamar Formation.

underlying El Alamar Formation and a gradational contact between the La Joya Formation and overlying Minas Viejas Formation evaporite.

Given the thickness and lack of stratigraphic continuity and exposure throughout the study area, the Jurassic La Joya Formation is combined with the Triassic El Alamar Formation and hereto referred to as “Triassic-Jurassic red beds”.

9. Upper Jurassic Minas Viejas Formation

The Upper Jurassic Minas Viejas Formation is composed of predominantly gypsum-anhydrite with intervals of carbonate. The only evaporite exposed at the surface is gypsum as a result of hydration. Cross (2012) conducted a detailed stratigraphic study in the northern part of the Potosí uplift, identifying and characterizing different members of the Minas Viejas Formation. The formation in the northern part of the uplift contains ~350 m of carbonate, including five prominent intervals, the Tranquitas Member, the La Chimenea Member, the Los Cuervos Member, the Loma Largo Member, and the El Potosí Member. These carbonate intervals are typically thin- to thick-bedded micritic carbonates and locally contain calcareous shale. The basal evaporite sequence, the La Nieve Member, typically has a banded, mylonitic appearance and is the stratigraphic level containing the highest concentration of non-coaxial shear according to Cross (2012). A distinctive volcaniclastic interval of welded and reworked tuff approximately 50 m thick called the La Primavera Member is located ~400 m stratigraphically above the base of the formation. Between the underlying Jurassic La Joya Formation and the La Primavera Member is ~215 m of carbonate and ~185 m of evaporite (Cross, 2012). While many of the described members are present to the south and southeast, internal stratigraphy and basal sections vary.

Deciphering the internal stratigraphy of the Minas Viejas Formation in similar detail to that of Cross (2012) fell outside the scope of this project, but overall observations will be described.

The thickness of the Minas Viejas Formation is highly variable. Rheologic weakness of the substantial evaporite found within the formation allowed for ductile flow into anticlinal hinges and out of synclinal hinges of overburden detachment folds. Underneath synclines in the Potosí uplift, the formation is dominated by carbonate and can be as thin as ~500 m, whereas in the cores of anticlines it is ~2,000–3,500 m thick.

Unstrained or low-strain gypsum within the Minas Viejas Formation commonly appears with a nodular fabric as a result of the growth pattern of the crystals during deposition (Warren, 2006), often referred to as “chicken-wire” texture (Figure 9a). Nodules are composed of gypsum-anhydrite rimmed by fine-grained calcareous and/or silty sediments. Nodule preservation and/or observation in outcrops is dependent on both initial presence of large gypsum crystals as well as degree of strain within that particular interval of the Minas Viejas Formation, where high-strain gypsum may have mylonitic fabrics in which original nodular fabric cannot be observed (Figure 9b; 9c; 9d).

Carbonate intervals in the Minas Viejas Formation in the southern part of the Potosí uplift vary in thickness and lithology and occur at different stratigraphic levels than in the north. The vast majority of carbonate beds are mudstones composed predominantly of micrite, though scarce fossiliferous wackestones and packstones are present as well. Centimeter-scale interbeds of carbonates are common within gypsum-dominated intervals and can appear as boudinaged clasts or highly folded continuous or discontinuous beds (Figure 10).

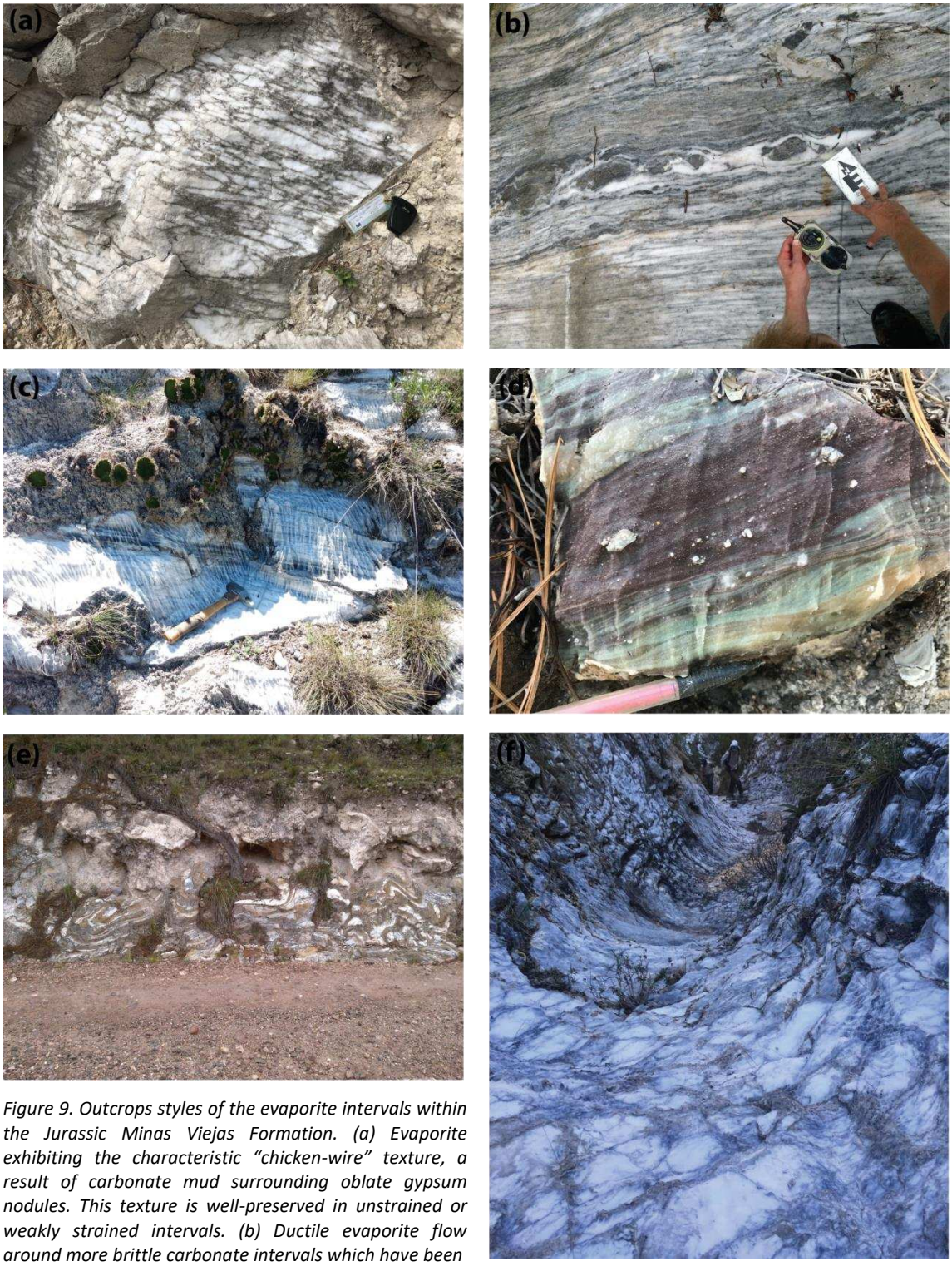

Figure 9. Outcrops styles of the evaporite intervals within the Jurassic Minas Viejas Formation. (a) Evaporite exhibiting the characteristic "chicken-wire" texture, a result of carbonate mud surrounding oblate gypsum nodules. This texture is well-preserved in unstrained or weakly strained intervals. (b) Ductile evaporite flow around more brittle carbonate intervals which have been boudinaged through décollement strain. Foliation is bedding parallel. This sample belongs to the La Nieve Member shear zone. (c) High strain evaporite mylonite surrounded by gypsophile fauna. This is the typical appearance of gypsum outcrop outside of canyons within the evaporite. (d) High strain evaporite mylonite with color banding as a result of fine-grained siliciclastics. (e) Ductile evaporite folds. The folds are typically non-cylindrical and do not share a consistent vergence, fold axis, or fold geometry characteristics such as interlimb angles or orientations. (f) A gypsum canyon south of Cañón Santa Barbara (Plate 1). Large gypsum nodules surrounded by carbonate seams are clearly visible and the erosional style of the evaporite canyons in the area give insight into their geometries.

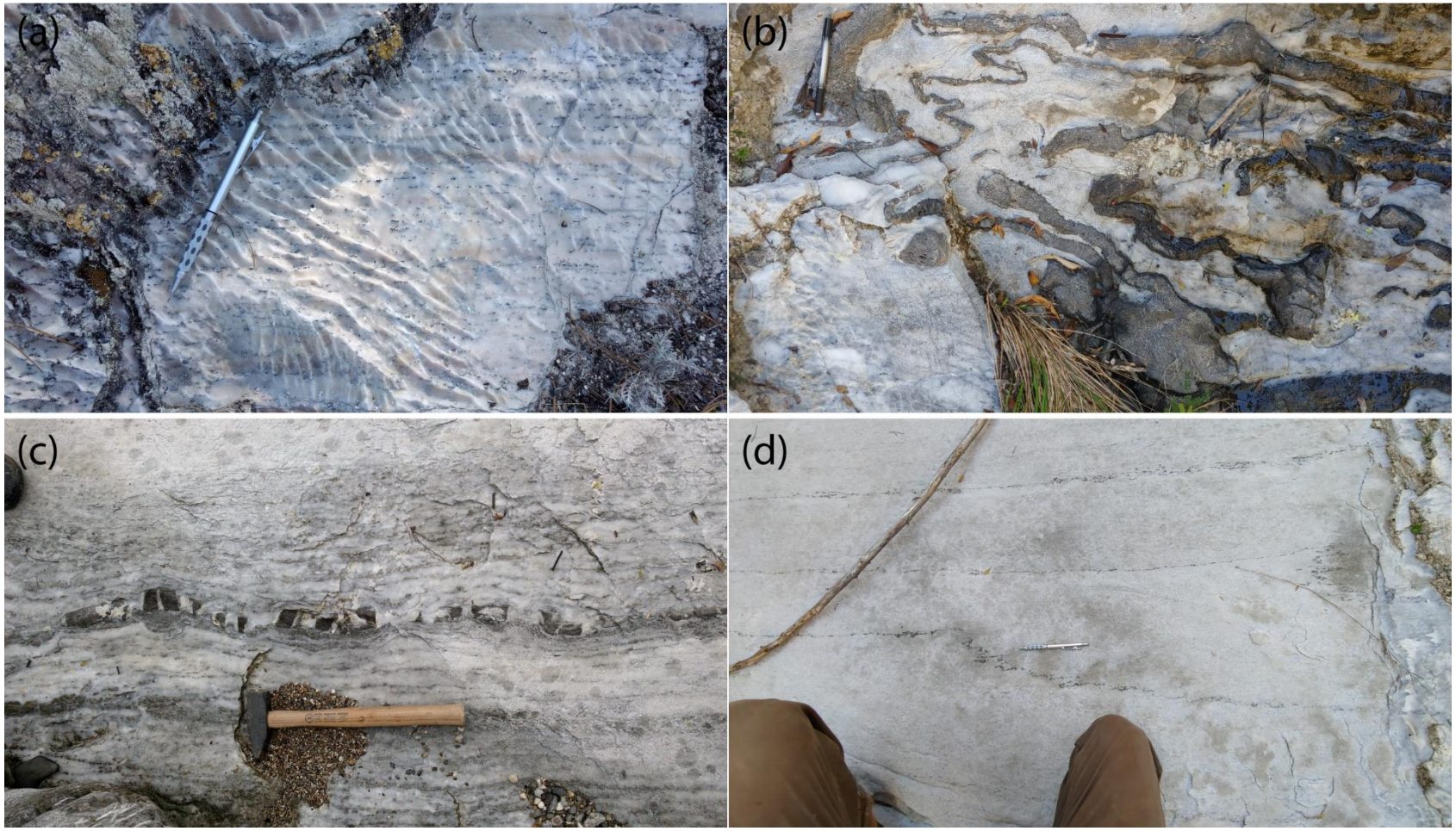

Figure 10. Carbonate boudinage and discordant folding in the Jurassic Minas Viejas Formation. (a) thin (~1 mm) seams of carbonate boudins in a dominantly gypsum outcrop. (b) Extensive folding of a carbonate interval within gypsum. Parasitic folds in different carbonate intervals are visible, but folding is overall discordant and records the ductility of the evaporite. (c) boudinaged carbonate interval (~2 cm thick) with high strain gypsum above and below it. Gypsum laminations deflect into the space created by the extending carbonate boudins as the gypsum flowed around the brittle strata. (d) Discordant folding in carbonate seams in a predominantly gypsum interval.

The most laterally continuous carbonate member of the Upper Jurassic Minas Viejas Formation is the El Potosí Member, which caps the formation throughout the entire study area (Figure 11). This member has historically been assigned its own formation, the "Zuloaga Formation" or "Zuloaga Limestone", as it has been correlated as far north as Monterrey. Cross (2012) argues for the inclusion of the Zuloaga Formation into the Minas Viejas Formation instead, and introduces it as the "El Potosí Member". Cross (2012) states that 1) though the capping carbonate can be correlated to the Zuloaga Formation, it is drastically different in both lithology and thickness to the type section, and 2) the Minas Viejas Formation has multiple carbonate members which are substantially thicker than the capping carbonate, and as such it does not warrant a distinction. For this reason, the capping carbonate will be referred to as the El Potosí Member of the Minas Viejas Formation.

Biostratigraphy within the Jurassic Minas Viejas Formation suggests the depositional age is from upper Oxfordian to lower Kimmeridgian (Zell et al., 2015), consistent with known ammonite biostratigraphy within the overlying La Casita Formation, which has a middle Kimmeridgian depositional age near the base (Cross, 2012).

9.1. Basal Stratigraphy of the Minas Viejas Formation – The La Nieve and Río de San José Members

The basal stratigraphy of the Jurassic Minas Viejas Formation varies across the Potosí uplift. In the north surrounding Tranquitas, the La Nieve Member is present, lithologically

Figure 11. The upper contact between the Jurassic Minas Viejas Formation (the El Potosí Member) and the overlying Jurassic-Cretaceous La Casita Formation. The El Potosí Member is a ~2-3m thick carbonate interval underlain by gypsum evaporite to the west and black shales and carbonates of the La Casita Formation to the west and forms a prominent ridge parallel and within the

gradational from the underlying Jurassic La Joya Formation red beds to predominantly gypsum-anhydrite. This basal evaporite forms the lower décollement shear zone, consisting primarily of banded mylonites (Figure 9d). The La Nieve Member is ~80 m thick at the type-section, but ranges from ~15 m to ~360 m thick near Tranquitas alone (Cross, 2012).

Throughout the southern Potosí uplift, the lowest section of the Minas Viejas Formation commonly contains calcareous black to gray shale (Figure 12), resembling the Jurassic-Cretaceous La Casita Formation (See 10.1) which overlies the Minas Viejas Formation. Given the similarity and lack of detailed mapping in this area, this basal shale has previously been misidentified as the La Casita Formation (Michalzik, 1991; Barboza-Gudiño et al., 2010; Cross, 2012), requiring significant structural omission to explain the lack of Minas Viejas Formation between the shale and the Triassic-Jurassic red beds. Though highly variable in thickness, ranging from a few cm to ~100–125 m, it is consistently present across the southern study area and most likely represents a distinct depositional facies within the Minas Viejas Formation. Underlying and overlying strata varies across the uplift, but is locally underlain by Minas Viejas carbonate, red beds, or thin evaporite intervals (cm- to m-scale surrounding the northern part of Cañón El Alamar). It is typically overlain by Minas Viejas carbonate or evaporite, evaporite thickness also variable locally. Accordingly, I propose this shale interval to be named the Río de San José Member. This interval often has a phyllitic sheen due to due to aligned fine-grained white mica from low-grade metamorphism.

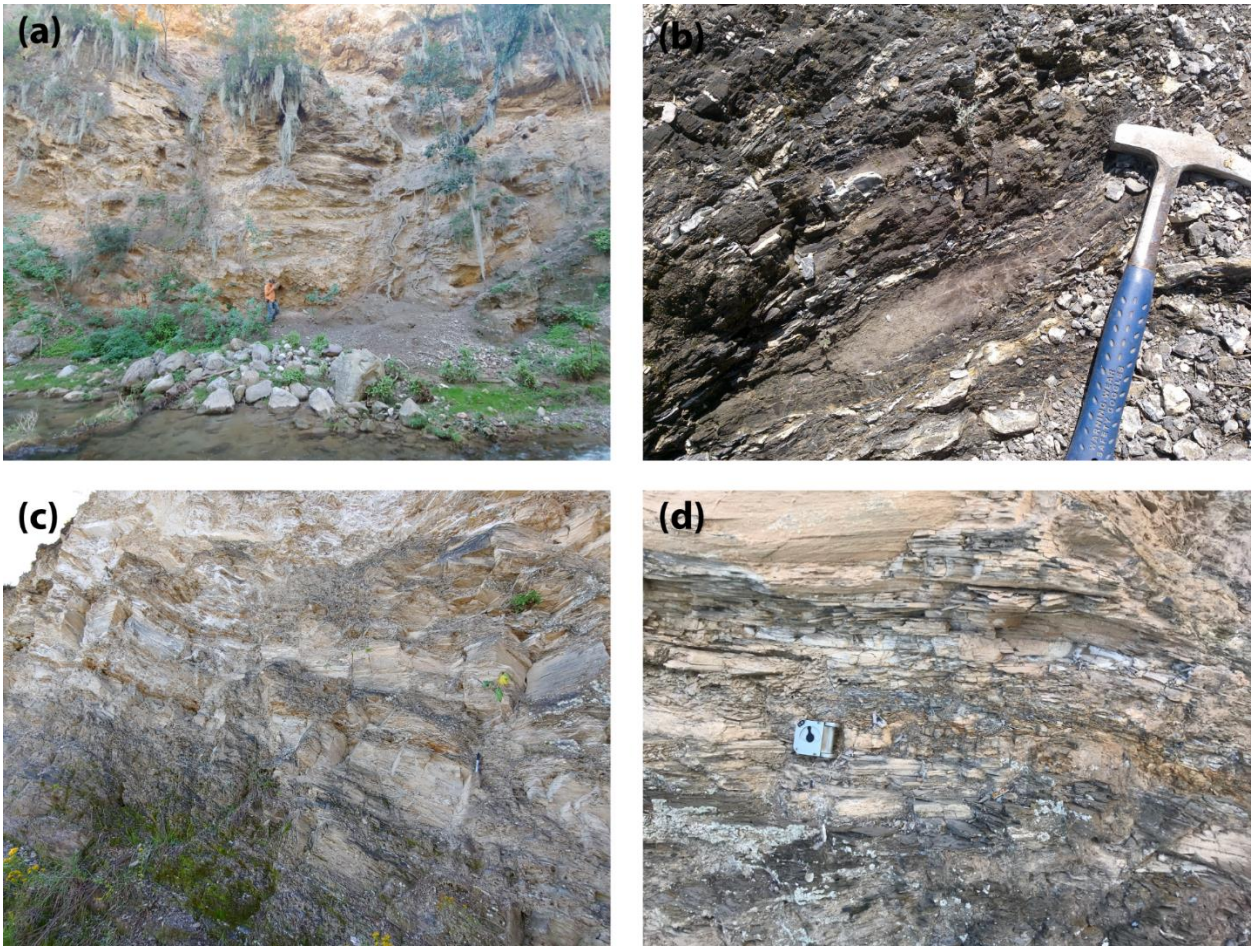

Figure 12. Typical outcrops of the Río de San José Member of the Jurassic Minas Viejas Formation. This basal shale interval is typically black to tan and calcareous. (a) Located at the mouth of Cañón El Alamar (Plate 1), the Río de San José Member has most likely been structurally thickened as a result of a sub-horizontal thrust fault. Cleavage is well developed and typically SW dipping, and both upper and lower contacts are concealed. (b) Black shale interval within the Río de San José Member, easily mistaken for the La Casita Formation. This outcrop, located on the west side of Cañón El Alamar, is ~1-2 m thick, and is underlain by a thin interval of evaporite (~1-2 m), and overlain by a thicker interval of evaporite (>10 m). (c) Outcrop of the Río de San José Member in the southern Cañón El Alamar. This interval overlies basal carbonates which are in stratigraphic contact over Triassic-Jurassic red beds. The Río de San José Member at this locality records subhorizontal and bedding parallel thrust faults associated with oxidation and alteration. (d) Alteration and oxidation fault zone, Brunton compass for scale. Shale appears more brittle and recessive in the fault zone and appears to be associated with iron oxidation.

10. Upper Jurassic – Cretaceous Strata

Strata overlying the Jurassic Minas Viejas Formation are described in this section and are collectively referred to within the subsequent text as: “overburden”. These units are predominantly carbonate platform sequences, often interbedded with shale, deposited during the Cretaceous.

10.1. Upper Jurassic – Lower Cretaceous La Casita Formation

The Upper Jurassic – Lower Cretaceous La Casita Formation is roughly 150 m thick and is characterized by its distinct calcareous black to gray to tan shale intervals and abundant fossil-bearing carbonate nodules, along with minor thin interbeds of carbonate. Tan calcareous shale may also be present as black shale that has since been altered through exposure to surficial weathering (Figure 13). Locally, calcareous medium-to-coarse-grained sandstone intervals may be present near the boundary with the overlying Cretaceous Taraises Formation.

Calcareous nodules are typically oblate and up to ~30 cm long. Carbonate nodule formation is most likely a result of early diagenesis, as surrounding bedding is often deflected as a result of post-nodular compaction (Marshall and Pirrie, 2013). As the nodules tend to form around organic matter due to interactions of methane, organic matter, microorganisms, and the water geochemistry (Marshall and Pirrie, 2013), the La Casita Formation nodules often contain abundant fossil assemblages including whole ammonites, gastropods, partial fish skeletons, and/or fossil hash. Ammonite biostratigraphy within the Jurassic-Cretaceous La Casita Formation suggests deposition from the Kimmeridgian to the Berriasian (lowermost Cretaceous) (Michalzik and Schumann, 1994).

Figure 13. Jurassic-Cretaceous La Casita Formation along a riverbed. Fresh outcrop, located near the bottom of the picture, is typically black and calcareous. More weathered outcrop, center of the picture, has been oxidized and is frequently a tan color. This outcrop is located in the subvertical to overturned limb of the Synclinal Providencia, south of the Río El Alamar (Plate 1). Cleavage has been refolded, creating the gently dipping fabric, while bedding is near-vertical. Dr. Michael Prior for scale.

10.2. Lower Cretaceous Taraises Formation

The Lower Cretaceous Taraises Formation is ~155 m thick and is comprised of well-bedded micritic carbonate beds of moderate thickness (~5–20 cm). The lack of chert nodules and its thinner beds distinguish the carbonate interval of the Taraises Formation from the overlying Cretaceous Tamaulipas Formation. The boundary between the two is a 2 to 4-m-thick shale-rich

interval that caps the Taraises Formation. Ammonite biostratigraphy suggests a Berriasian to Hauterivian depositional age for the Taraises Formation (Humphrey and Díaz, 2003).

10.3. Lower Cretaceous Tamaulipas Group

The Lower Cretaceous Tamaulipas Group is composed of the Lower Tamaulipas Formation, the La Peña Formation, and the Upper Tamaulipas Formation. The group overlies the Cretaceous Taraises Formation. According to previous stratigraphic studies and mapping (Humphrey and Díaz, 2003; SGM, 2010b), the Lower Cretaceous La Peña Formation separates the Cretaceous Lower Tamaulipas Formation and Upper Taumaulipas Formation. The shale-dominated La Peña Formation ranges from 5–100 m thick, and previous mapping in the study area suggests a thickness in the range of 50–70 m (Humphrey and Díaz, 2003; SGM, 2010b). However, I never observed La Peña Formation in the study area despite multiple transects to locate it. For this reason, the Lower and Upper Tamaulipas formations have been grouped together into the Tamaulipas Group and will presumably include the intermediate La Peña Formation as an unobserved interval. An alternate explanation for the lack of observance for the La Peña Formation is that the formation was not originally deposited in this area, which is unlikely given the extent and continuity of the formation across northeastern Mexico (Humphrey and Díaz, 2003).

The Tamaulipas Group carbonate beds are typically ~30 cm thick and contain abundant chert nodules, commonly in anastomosing and interconnected bedding-parallel forms. Fossil-rich beds are infrequent, but can be found containing an abundance of ammonite bioclasts. The complete thickness of this unit was not measured in the field, but it is approximated to be ~830

m thick based on previous mapping of the overlying Upper Cretaceous carbonates by the Servicio Geológico Mexicano (SGM, 2010b). Correlative units to the Lower Tamaulipas Formation have been assigned a Berriasian to Valanginian age based on ammonite biostratigraphy (Humphrey and Díaz, 2003). Biostratigraphy indicates a Lower Aptian age for La Peña Formation (Barragán and Maurrasse, 2008) and a Lower and Middle Albian age for the Upper Tamaulipas Formation (Humphrey and Díaz, 2003).

10.4. Undifferentiated Upper Cretaceous Carbonates

Upper Cretaceous carbonate formations are present within Sierra Tapias (Plate 1). The included formations are: the Cuesta del Cura Formation, Agua Nueva Formation, San Felipe Formation, and Mendez Formation (SGM, 2010b). A lack of exposure, difficulty in accessibility, and little-to-no observation resulted in grouping these formations into an undifferentiated Upper Cretaceous Carbonates group. These various formations are typically carbonates with intervals of finer-grained shales (SGM, 2010b). The Cuesta del Cura Formation is estimated to be 110 m thick, the Agua Nueva Formation ~103 m thick, and the San Felipe Formation and Mendez Formation between ~500–1000 m thick, though they do not exhibit full thickness as they are the youngest strata in the area and have been eroded (Humphrey and Díaz, 2003).

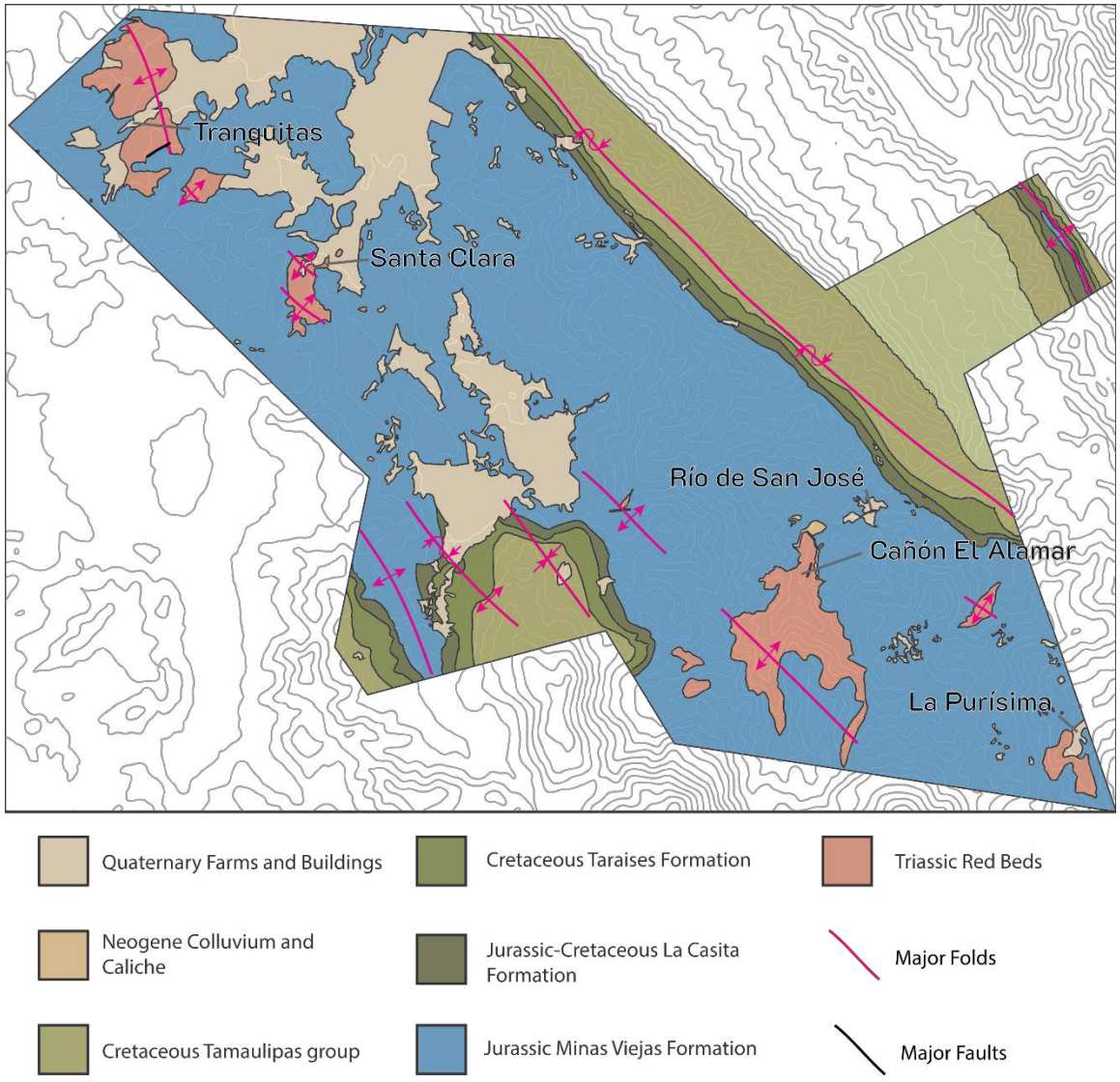

Figure 14. Simplified geologic map produced by this study, with depositional contacts, fault contacts, folds, and geographic locations indicated. See Plate 1 for full detailed version.

11. Structures within the Jurassic-Cretaceous Overburden

The largest structural features in the study area, and across the northern and central Sierra Madre Oriental, are detachment folds composed of the prominent Cretaceous carbonate

platform formations. These folds typically have a wavelength of 5–6 km with an average amplitude of 2–3 km throughout the Sierra Madre Oriental (Padilla y Sánchez, 1985; Ramírez-Peña and Chávez-Cabello, 2017). Due to the underlying décollement within the Jurassic Minas Viejas Formation, these folds involve only the Minas Viejas Formation and overlying Jurassic-Cretaceous strata. Though the fold belt within the northern and central Sierra Madre Oriental consists primarily of upright, tight to isoclinal box folds which lack clear or consistent vergence, overburden folds within the Potosí uplift are locally asymmetric, ranging from upright to recumbent and open to isoclinal (most frequently tight), with overturned limbs and variably-plunging fold axes (Plate 1; Figure 11, 14, 15). The Jurassic-Cretaceous overburden strata are only exposed along the eastern and western flanks of the Potosí uplift.

Strata along the western flank of the uplift mostly dip shallowly (~10–35°) southwest (Plate 1). Small-scale chevron folds and overturned kink folds are present at an outcrop scale and appear discontinuous along strike. Within the study area, the youngest formation exposed on the western flank is the Lower Cretaceous Tamaulipas Group. Major regional folds can be found on the western flank: the Anticlinal San Felipe, a symmetric anticline exposing Jurassic Minas Viejas gypsum in the core, and the Synclinal Cienuguillas, a symmetric syncline with Lower Cretaceous Tamaulipas Group in the exposed core. A smaller-scale fold, the Anticlinal Giro Pequeño, is locally overturned in a moderately-inclined tight chevron fold.

Strata along the eastern flank of the uplift dip much more steeply than on the western flank, with near-vertical and overturned Upper Jurassic Minas Viejas and Lower Cretaceous strata (Plate 1). The overturned anticline/syncline pair involving the limb of the Synclinal Providencia, as well as the more distant Anticlinal Iturbide, are upright to steeply-inclined open-to-tight

horizontal folds. The Synclinal Providencia hosts a series of recumbent to moderately inclined chevron folds on its western overturned limb bounding the uplift; these chevrons are horizontal and range from open-to-tight (Figure 15). These chevrons are incompatible as parasitic folds to the larger scale overburden folds. The most prominent chevron folds, the Pliegues Agudo, can be traced for ~42 km from east of Río de San José to north of Galeana. They are horizontal recumbent folds that becomes tighter to the south. Major regional folds include the aforementioned Synclinal Providencia and the Anticlinal Iturbide, a horizontal upright isoclinal near-symmetric anticline with the El Potosí Member of the Minas Viejas Formation exposed in the core (Plate 1).

Stylolites are common in the carbonate beds, particularly in the Cretaceous Tamaulipas Group. They are consistently found perpendicular to bedding, even in steeply-tilted strata. Extensional fractures (joints and veins) can be found in practically every carbonate bed and several shale intervals. The most dominant extension fracture set strikes east-northeast and commonly has calcite mineralization (Figure 16). This set has also been observed cutting across stylolites, indicating the relative timing of forming after tectonic pressure-dissolution (Figure 16).

Carbonate-dominated strata, such as the Cretaceous Tamaulipas Group, often contain thin cm-scale interbeds of fine-grained siliciclastics. The contacts between them may vary from planar to undulatory and rippled. These shaly interbeds locally acted as flexural slip and detachment horizons, resulting in detachment folds (Figures 17, 18).

Cleavage in the Jurassic-Cretaceous overburden is locally well-developed within the La Casita Formation. Measurements of poles to cleavage (n=14) are scattered in a girdle distribution

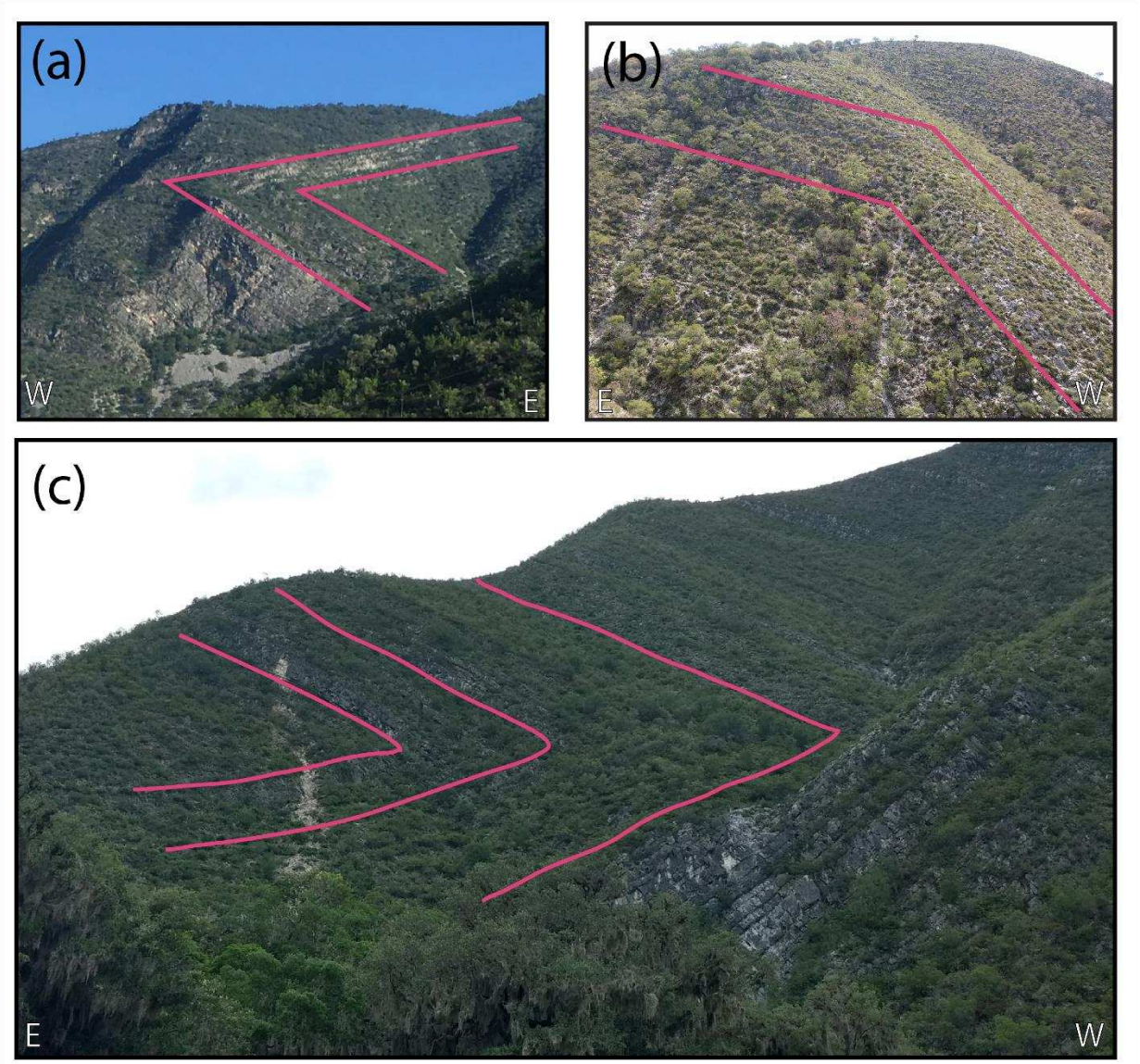

Figure 15. Chevron folds within the Synclinal Providencia (Plate 1). Fold geometry varies based on location along strike of the fold and can locally be open to tight. Multiple chevrons folds are locally present instead of a single hinge, forming a series of chevrons defining the overturned synclinal keel. The hinge of the chevron folds typically do not crop out, likely a result of a high concentration of strain and subsequent weathering. (a) This chevron fold is visible looking north in Cañón de Tomates south of Cañón Santa Barbara. (b) This open chevron fold is located on the cross-section line of B-B' (Plate 1) looking south. It is paired with another chevron fold to the west, forming the hinge of the Synclinal Providencia (Plate 1) and is nearly completely overturned. (c). This chevron fold is located along the Río El Alamar (Plate 1) looking southward.

Figure 16. Joints, veins, and stylolites in the Cretaceous Tamaulipas group. Veins parallel the joints, typically oriented ENE-WSW, and postdate stylolites.

Figure 17. Detachment fold along a shale horizon in the Cretaceous Tamaulipas group. These detachments likely helped accommodate the larger chevron folds (Figure 14). Field assistant Blake Franklin for scale.

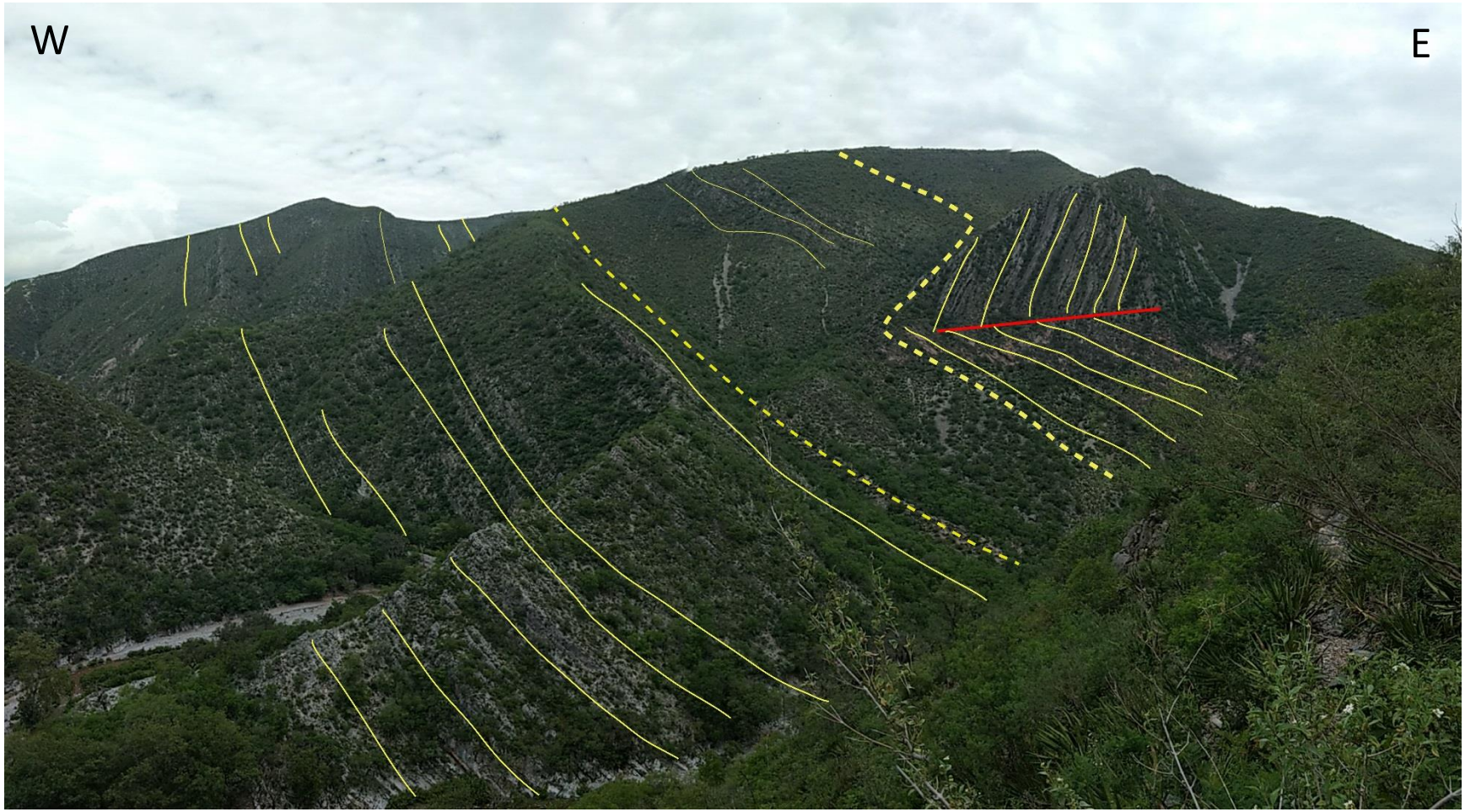

Figure 18. Chevron detachment folding in the hinge of the Synclinal Providencia, looking north near the Río El Alamar (Plate 1). Bedding highlighted in yellow, axial trace of the chevron fold marked in red, and inferred detachment planes marked with dashed yellow lines. These detachment folds likely accommodate the required volume displacement within the inside of a fold hinge.

with a high G-value (0.44), suggesting some dispersion due to folding along an axis oriented 147°, 12° (Figure 19b). Exposure of variably dipping cleavage is apparent within Cañón de Tomates adjacent to overturned Cretaceous strata in the limb of the Synclinal Providencia.

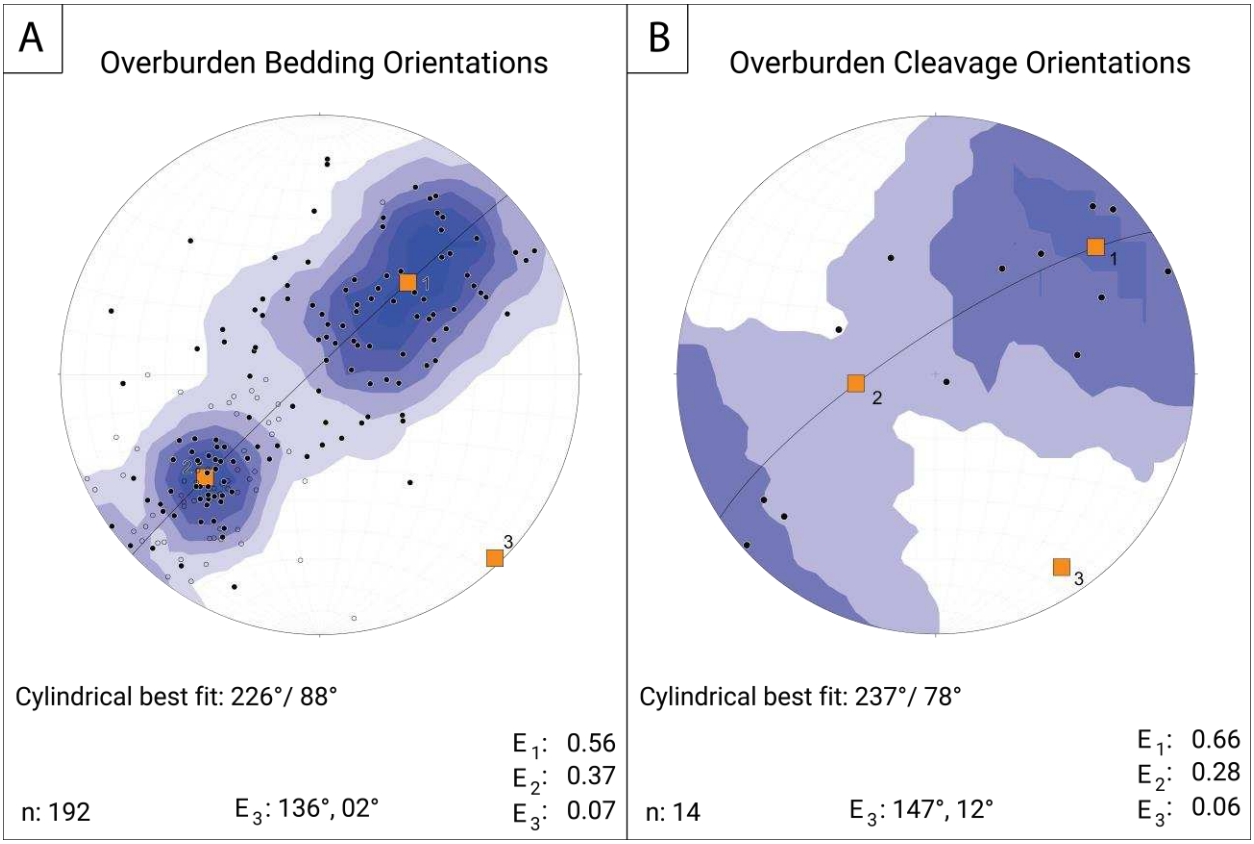

Figure 19. Stereoplots of overburden structural orientations, shown are poles-to-planes, best fit great circle, and eigenvectors. Annotated below are number of samples, eigenvalues, and orientations of E_3. (A) Overburden bedding orientations, upright bedding as solid circles, overturned bedding as hollow circles. (B) Overburden cleavage orientations.

Bedding (n=192) in the Jurassic-Cretaceous overburden strata has been drastically folded, in some localities nearly 180° overturned (Plate 1; Figure 15). Folding was consistent about a subhorizontal NW-SE trending axis, with a mean axis oriented 136°, 02° (Figure 19a). A relatively small P-value (0.19) and large G-value (0.60) corroborates the magnitude and consistency of folding found within the overburden. Overall, axial traces trend NNW-SSE. These orientations are similar to the trend of overburden fold axial traces mapped by the Servicio Geológico Mexicano

(SGM, 2010b, 2010c) at 1:50,000-scale. These maps reveal the variability in overburden fold axial trace orientations, trending between ~124° to ~193°. Eighty fold axial trace orientations recorded from geologic maps were analyzed to determine overall trends of folds, and cumulatively 109 km of fold axial traces mapped by SGM (2010b, 2010a) yielded a mean trend of 150°.

12. Structures within the Minas Viejas Formation Décollement

The thin-skinned décollement throughout the study area lies entirely within the Jurassic Minas Viejas Formation. The lower décollement contact directly overlies the Triassic-Jurassic red beds and parallels the underlying strata. The décollement interior is structurally chaotic with complex fold geometries. The upper ~500–700 m of the Minas Viejas Formation lies above the décollement, striking parallel to the overlying Jurassic-Cretaceous La Casita Formation. Within this supradécollement interval both foliation (defined by flattened evaporite nodules) and bedding parallel the NW-SE structural grain of overburden folds. In discussing structural orientations, the term “bedding” will be reserved for carbonate intervals within the Minas Viejas Formation, and “foliation” will be reserved for layering in evaporite intervals. Structural data in the Minas Viejas Formation are grouped based on these three domains: supradécollement, décollement interior, and lower décollement.

12.1. Supradécollement

The supradécollement interval in the Minas Viejas Formation is characterized by harmonic conformity with the overlying Jurassic-Cretaceous strata. This distinction between the supradécollement and disharmonic layering in the décollement interior is an inferred planar

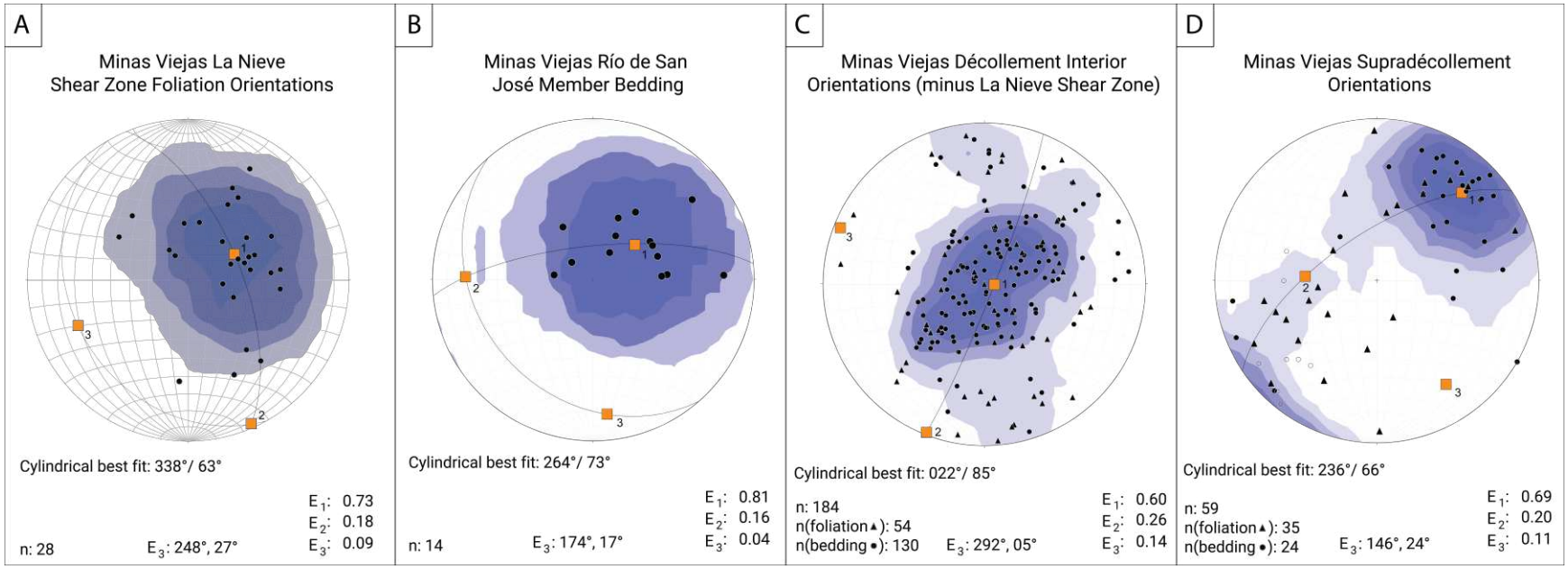

Figure 20. Jurassic Minas Viejas structural orientations, shown as poles-to-planes with best fit great circles and eigenvectors. Annotated below are the great circle orientations, eigenvalues, number of measurements, and orientation of E_3. (A) Foliation orientations within the basal La Nieve Member shear zone. (B) Bedding measurements within the Río de San José Member basal shale. (C) Décollement interior structural orientations, both foliation and bedding displayed. For more detailed stereoplots of the décollement interior, see Figure 21. (D) Foliation and bedding measurements within the supradécollement.

contact that strikes NNW-SSE. This interval is best exposed along Cañón de Tomates, where bedding and foliation parallel NE-dipping, overturned beds in the El Potosí Member and overlying Casitas Formation (Figure 11). This supradécollement interval is roughly 500-700 m thick on average (Plate 1), but thickness varies as a result of flow associated with overlying folds, previously described in Section 9.

Compared to the décollement interior, foliation and bedding appear much more coherent and harmonic with one another, and foliation is commonly bedding-parallel. Bedding and foliation have only been observed as discordant near fold hinges within the evaporite, where foliation appears axial planar (Figure 21). The average bedding plane (n=24) within the supradécollement is oriented 121°/55°, while the average foliation plane (n=35) is oriented 138°/66° (Figure 20d).

The strata within the supradécollement appear to have been folded along an axis oriented 146°, 24° (Figure 20d). The fold axis trend within the supradécollement is similar with that of the overburden strata (146° vs. 136°, respectively), though the plunge is quite different (24° vs. 02°). This variation may reflect a location bias as the majority of the supradécollement measurements come from Cañón de Tomates, whereas overburden bedding orientations were measured over a wider area.

Boudinaged carbonate beds and strained gypsum nodules were analyzed as strain markers. Three different cm-scale carbonate interbeds within gypsum in the mouth of Cañón Santa Barbara record extension magnitudes of 93%, 180%, and 670% along the NW-SE to NNW-SSE strike direction. The latter two values come from beds similar in thickness at the same outcrop, highlighting the extremely heterogeneous nature of strain within the Minas Viejas

Figure 21. In most intervals of the Jurassic Minas Viejas, foliation is parallel to bedding. Surrounding fold hinges, however, foliation may be discordant and perpendicular to oblique to bedding. This outcrop, located in Cañón Santa Barbara (Plate 1) records foliation axial planar to the folded bedding, indicated by the compositionally variable layer.

evaporite. The orientations and ellipticity of strained gypsum nodules were measured on multiple proximal planes to determine 3D strain geometry. However, strain analysis software *EllipseFit* (Vollmer, 2018) was unable to resolve a best fit ellipsoid due to the heterogeneity in strain at even an outcrop scale. Measured long-axis to short-axis ratios of nodules vary between 3.5:1 to 14.4:1. Larger strain magnitudes are most likely common, but identification of nodule boundaries at such high magnitudes of strain is impractical.

12.2. Décollement Interior

Whereas the supradécollement is characterized by harmonic coherency with the Jurassic-Cretaceous overburden folds, the décollement interior is notably more chaotic and disharmonic. The Minas Viejas evaporite within this zone does not appear as a singular discrete shear zone, but rather strain appears distributed and heterogenous. Locally, high-strain zones with mylonitic gypsum are interlayered with lower-strain gypsum. Folds within both the evaporite and thin carbonate intervals are commonly disharmonic and non-cylindrical (Figure 10b, 10d) and range from cm-scale to hundreds-of-m-scale, though especially large carbonate intervals are commonly folded about an apparent cylindrical fold axis.

Orientations of carbonate bedding (n=130) and evaporite foliation (n=54) collected within the décollement interior highlight the aforementioned chaos (Figure 10b, 10d). Poles to bedding have a relatively high R-value (0.33), but retain a moderate P- and G-value (0.45 and 0.22, respectively), with the mean orientation corresponding to a plane oriented 164°/ 04° (Figure 20c). By contrast, poles to foliation has a very high R-value (0.54) with lower P- and G-values

overall (0.08 and 0.38, respectively), highlighting the chaotic nature of deformation in the evaporite. The discrepancy between the foliation and bedding PGR values captures the rheological differences and discordance between the evaporite foliation and carbonate beds (Figure 22), where the evaporite behaved completely ductilely and was prone to heterogeneous strain, whereas the more rigid carbonate beds are locally conformable with overburden strata. A cylindrical best fit to poles of bedding and foliation in the décollement interior indicate folding along an axis oriented 292°, 05° (Figure 20c).

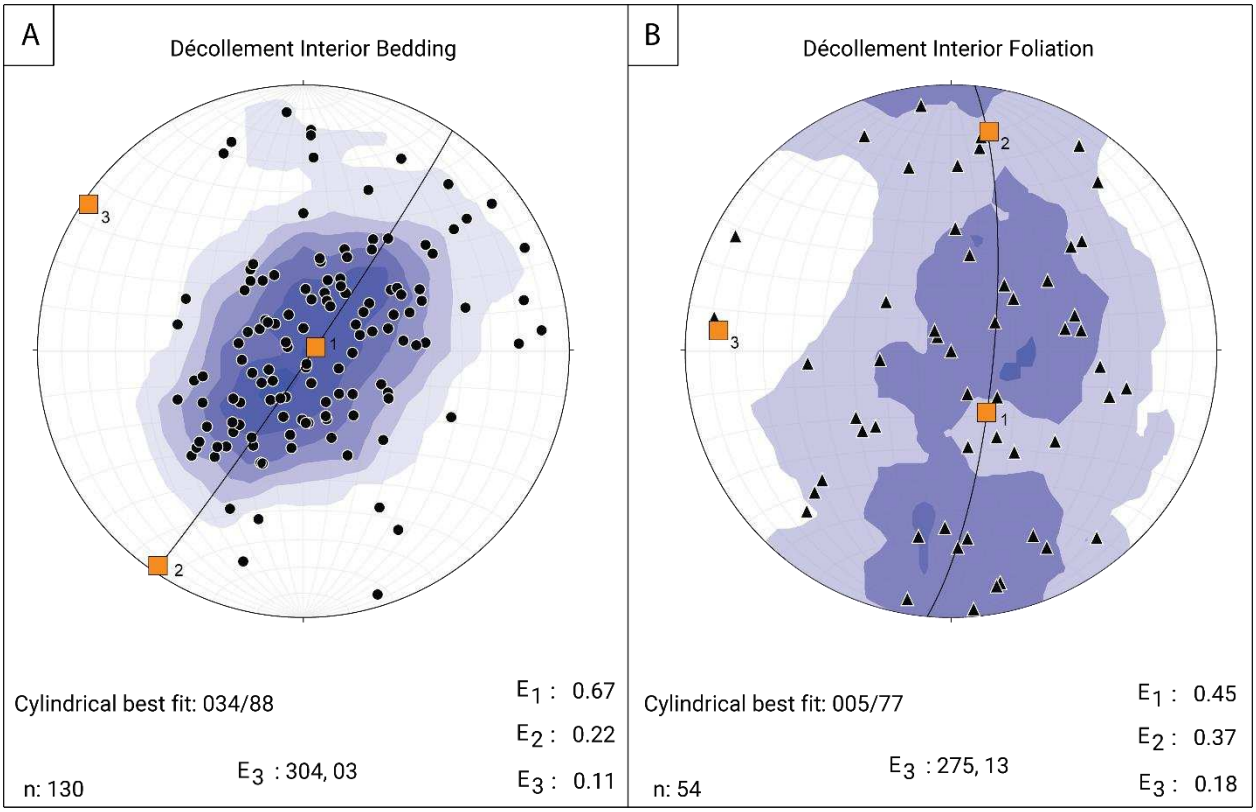

Figure 22. Stereoplots highlighting structural variability between bedding and foliations in the décollement interior. (A) Bedding appears mostly coherent forming a moderate P- and G-value (0.45 and 0.22, respectively) with a relatively moderate R-value (0.33). (B) foliation appears much more chaotic and randomly distributed, an R-value of 0.54.

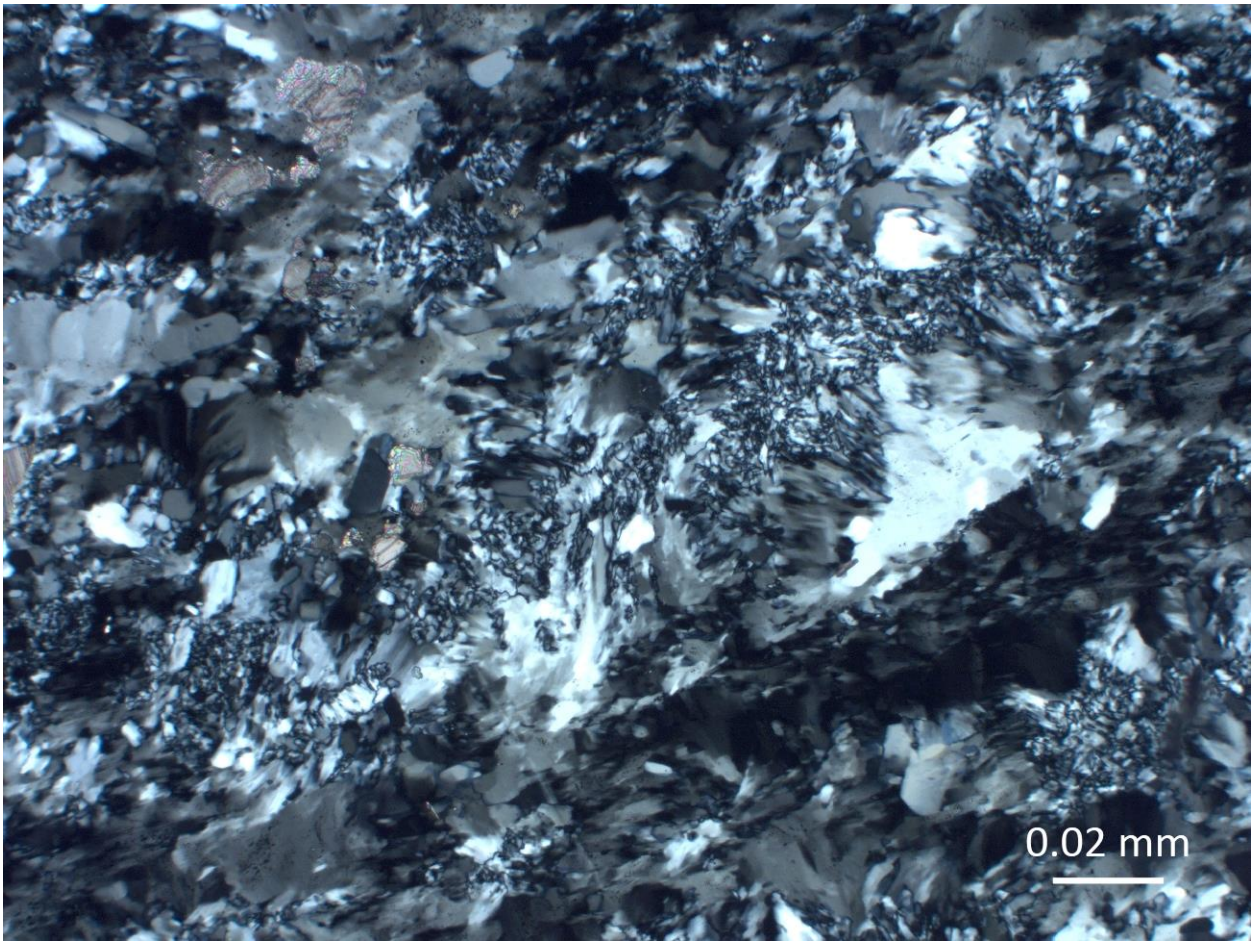

Figure 23. Photomicrograph of the Jurassic Minas Viejas Formation gypsum. Rehydration from anhydrite eliminated any tectonic microstructures that may have been present.

Deformation microstructures are rarely preserved within the Jurassic Minas Viejas Formation gypsum. Though the evaporite was most likely deposited as gypsum during the Jurassic, subsequent burial resulted in dehydration, transitioning the gypsum to anhydrite. Given the thickness of overlying strata, the evaporite was most certainly anhydrite during Late-Cretaceous to Paleogene thin-skinned and thick-skinned shortening, typically requiring only 50–60°C for anhydritization to occur (Warren, 2006), and burial depths of between 0.4 to 4.0 km, depending on lithology of overlying and underlying strata (Jowett and Cathles, 1993). Most recently, erosion of overlying strata and the exhumation of anhydrite resulted in rehydration back to gypsum, and though many macrostructures have been preserved (gypsum nodules,

interbeds of carbonates, folds, boudins of more resilient carbonates), microstructures in the gypsum reveal no preservation of tectonism, such as grain-shape fabrics, dynamic recrystallization, or shear sense indicators (Figure 23). Though the conversion of anhydrite to gypsum results in volume gain, there is no evidence of sedimentary fabrics or structures being disturbed by hydration, which is consistent with previous studies that demonstrate anhydrite volume is preserved through the removal of excess gypsum in solution (Holliday, 1970; Shearman et al., 1972; Testa and Lugli, 2000).

12.3. Lower Décollement and the La Nieve Member Shear Zone

In the northern portion of the study area near Tranquitas, where the basal stratigraphic section consists of evaporite, the stratigraphically lowest evaporite (La Nieve Member) contains the highest concentration of shear strain within the décollement, comprising a non-coaxial mylonitic shear zone ~35–150 m thick (Cross, 2012). Within this shear zone lineations defined by elongate carbonate inclusions trend NE-SW to ENE-WSW (Cross, 2012), and shear bands and foliation patterns record top-NE to top-ENE shear (Figure 9d). Sulphate nodules and the "chicken-wire" texture within the shear zone have been strained beyond recognition during development of mylonitic fabrics.

Within the La Nieve Member shear zone the average foliation plane (n=28), corresponding to E_1, is oriented 151°/27° (Figure 20a). Given the eigenvalues, a relatively high P-value of 0.55 and a lower G-value and R-value (0.18 and 0.27 respectively) suggest there was minimal folding of the La Nieve Member shear zone where measured. Moreover, E_3, oriented 248°, 27° (Figure 20a), does not match that of the overburden folds.

In the central and southern portions of the Potosí uplift, the base of the Minas Viejas Formation is the Río de San José Member, which consists of calcareous shale, as opposed to the nearly entirely evaporitic La Nieve Member. As a result of the lithologic differences, the lower part of the décollement is a mixed brittle-ductile shear zone with evidence of brittle thrust faults and bedding-parallel slip planes in addition to development of shear fabrics associated with moderately to well-developed cleavage. Thin-section samples indicate that cleavage is defined by aligned white mica grains and contain weakly- to moderately-developed strain fringes. Inclination of cleavage with respect to sheared bedding in outcrop and hand samples indicate top-to-the-northeast shear. Within Cañón El Alamar at the northern end of the canyon, the Río de San José Member appears at least ~34 m thick, though the base is not exposed and appears to have undergone structural thickening via thrust faulting (Figure 12a).

Bedding orientations (n=14) collected in the Río de San José Member basal shale share similarities with the La Nieve Member shear zone foliation orientations, with the average bedding plane oriented 139°/28° (compared with an average foliation oriented 151°/27°) (Figure 20b). A calculated P-value of 0.64 and a moderate G-value and low R-value, 0.24 and 0.12 respectively, suggests similar deformation as the La Nieve member shear zone with minimal folding where measured. The moderate girdle distribution occurs about an axis oriented 174°, 17° (Figure 20b).

13. Structures within the Sub-Décollement Triassic-Jurassic red beds

Outcrop- and map-scale structures were recorded across the entirety of Triassic-Jurassic red bed exposures within the Potosí uplift (Figure 14; Plate 1). Bedding, cleavage, fault, fold, and fracture orientations were recorded and analyzed for kinematics relating to thick-skinned

shortening. Structural data from the sub-décollement red beds near Tranquitas (Figure 14; Plate 1) include 66 bedding orientation measurements from Cross (2012), who mapped the area at 1:10,000-scale. Barite veins, slip surfaces on barite veins, and faults containing barite mineralization are all presented separately from faults without barite mineralization. It is also assumed that deformation to sub-décollement strata occurred during thick-skinned uplift and was unaffected by thin-skinned folding, an assumption common to thin-skinned systems with a large rheologic strength difference between layers (Stewart, 1999).

13.1. Map Exposures and Unit Relationships

In most areas the Minas Viejas Formation overlies the red beds in a gently dipping depositional contact, but locally these two formations are juxtaposed along high-angle faults with tens to hundreds of meters offset (Plate 1). The largest exposures of red beds are near Tranquitas, Santa Clara, and Cañón El Alamar (Figure 14; Plate 1).

Near Tranquitas, Jurassic red beds of La Joya Formation are predominantly in stratigraphic contact with the overlying Jurassic Minas Viejas Formation (Figure 14). The Anticlinal Tranquitas, previously identified by Cross (2012), is a horizontal upright open fold within the red beds trending NNW-SSE with gently-to-moderately dipping limbs (up to 36° with an average of ~16°). Locally the red beds are juxtaposed against the Minas Viejas Formation along E- to NE-striking subvertical faults with apparent north-side-up displacement and barite mineralization (Figure 14). In northern Tranquitas (Figure 14), a fault with a ~6 m-thick barite core places red beds on the north against Minas Viejas Formation on the south and contains multiple planes of slip within the barite dipping 65–80° S. In north-central Tranquitas (Figure 14), a fault dipping ~87° to the

southeast with a 2–3 m-thick core of barite places red beds on the north against the La Nieve Member of the Minas Viejas Formation on the south. The Tranquitas Member carbonate overlies the red beds on the northern side of the fault, indicating a salt weld as a result of evacuation of the La Nieve Member, present only on the south side of the fault. Significant ductile flow of the La Nieve Member requires that temperatures during this faulting were above the brittle-plastic transition of anhydrite (>80°C, Davis and Engelder, 1985). In southern Tranquitas (Figure 14), a poorly exposed NE-striking fault places red beds on the north against the Minas Viejas Formation on the south.

Surrounding Santa Clara, gently-dipping (~5–10°) red beds are in stratigraphic contact with the overlying Minas Viejas La Nieve Member evaporite (Figure 14). However, red beds at the southwestern-most exposure dip ~70° SW and are overlain by gently dipping Minas Viejas carbonate across a concealed contact. These variations in dip direction are consistent with the bedding orientations observed in the red beds, as there are small-scale parasitic folds within the more broad-scale anticlinorium (Plate 1). The parasitic folds observed surrounding Santa Clara typically indicate west-vergence and locally overturn red beds at decameter scale.

A relatively small exposure of red beds crops out in the upper part of Cañón Santa Barbara (Plate 1). At the northeastern end of this exposure the red beds are depositionally overlain by the Río de San José Member of the Minas Viejas Formation. This contact is sheared with <1 m of bedding-parallel brecciation above the contact. Poorly-developed cleavage in the red siltstone below the contact dips ~20–32° WSW suggesting top-ENE shear along the contact. The southwestern contact of the red beds in Cañón Santa Barbara is a subvertical E-W striking fault with minor barite mineralization that places carbonates and calcareous shales of the lower Minas

Viejas Formation on the south adjacent to red beds on the north. Steepening of the carbonate beds adjacent to the fault is consistent with apparent north-side-up displacement.

Relationships from Cañón El Alamar (Figure 14) are consistent with those in Tranquitas and Santa Clara, with predominantly stratigraphic contacts between the Triassic-Jurassic red beds and the overlying Río de San José Member of the Minas Viejas Formation. The contact between the two formations is clearly visible along the canyon walls (Figure 12c). Near the northeastern end of the Cañón El Alamar (Figure 14), uppermost red beds are juxtaposed against the Río de San José Member of the Minas Viejas Formation along a moderately ENE-dipping normal fault. As there is no visible offset of carbonate overlying the Río de San José Member, the fault presumably roofs into a bedding-parallel slip plane (Figure 12a). Elsewhere along the canyon, the stratigraphic contact between the red beds and the Minas Viejas Formation dips ~5–30° southwest and northeast. Red beds in the southwestern-most exposures in Cañón El Alamar consistently dip ~10–35° SW (Plate 1). Though data were not collected on the eastern wall of the southern Cañón El Alamar, the clearly visible contact between the red beds and the Minas Viejas Formation appears to be conformable, gently-dipping, and most likely stratigraphic (Figure 14).

West of the Cañón El Alamar red bed exposures two prominent exposures of Triassic-Jurassic red beds crop out on the road towards Pablillo (Plate 1). Red beds here are in stratigraphic contact with a basal carbonate section of the Jurassic Minas Viejas Formation (Figure 24). The southernmost exposure of red beds near the village of La Purísima (Figure 14) is characterized predominantly by gently ENE-dipping strata (~10–25°), and the stratigraphic contact with the overlying Minas Viejas Formation is not exposed.

Figure 24. Triassic-Jurassic red bed exposures west of Cañón El Alamar indicate stratigraphic contact between the red beds and the Jurassic Minas Viejas basal carbonate within the Río de San José Member (Section 9.1). This stratigraphic sequence was also observed at the southern rim of Cañón El Alamar where interbedded shales and carbonates underlie the thick shale interval of the Río de San José Member. Graduate student Skyler Mavor for scale.

13.2. The Potosí Anticlinorium

Triassic-Jurassic red beds in the Potosí uplift are exposed for ~36 km along trend of the uplift, from Tranquitas to La Purísima, and ~9.5 km perpendicular to the trend (Figure 14). Exposures form a NNW-trending anticlinorium with overall gentle western dips and gentle to moderate eastern dips, with layer-parallel shortening accommodated through smaller-scale folds, thrust and strike-slip faulting, and cleavage development. Given the historical name of the uplift, previous identification of this structure as the "Potosí anticline" (Padilla y Sánchez, 1978; Moor, 1980), and following suit of the well-studied Huizachal-Peregrina anticlinorium (Zhou et al., 2006), I propose the name of "Potosí anticlinorium" for this structure. The hinge of the Potosí anticlinorium roughly correlates with the mapped axial traces of the following anticlines: the

Anticlinal Tranquitas, the Anticlinal Santa Clara, the Anticlinal Cráneo, and the Anticlinal Paraíso (Plate 1).

Based on red bed exposures in Cañón El Alamar and Tranquitas and the elevation differences of overlying Jurassic-Cretaceous strata across the uplift, it is apparent that the western flank of the anticlinorium dips gently WSW, whereas the northeastern flank dips moderately ENE (Plate 1, Cross Section D-D'). Overburden folds (synclinal keels, anticlinal crests) are ~640 m higher within the uplift to the WSW and ~3,100 m higher within the uplift to the ENE in comparison to the elevation of these structures east and west of the uplift flanks. These estimations of overburden detachment fold geometries are based on average amplitude and wavelengths (Section 1) determined by Padilla y Sánchez (1985), and Ramírez-Peña and Chávez-Cabello (2017), in conjunction with field observations and contact locations.

Across the Potosí uplift the anticlinorium is upright to steeply inclined southwest with a subhorizontal fold axis. All bedding measurements in the red beds indicate an overall fold axis oriented 330°, 04° (Figure 25). Though there are minor tight parasitic folds within the red beds, the overall fold structure is open, with most beds dipping ≤45° (Figure 25). The consistently gentle to moderate dip of bedding yields a high P-value (0.60) with moderate girdle distribution (G-value of 0.30), and very little random spread (R-value of 0.09). The minor parasitic folds are exposed in Santa Clara and Cañón El Alamar (Plate 1). These fold axial traces trend parallel to the anticlinorium and locally have overturned limbs, though bedding typically dips moderately on the limbs.

Cleavage developed in finer-grained intervals of the Triassic-Jurassic red beds is defined by dissolution seams and aligned white micas. Cleavage is typically perpendicular to bedding, the

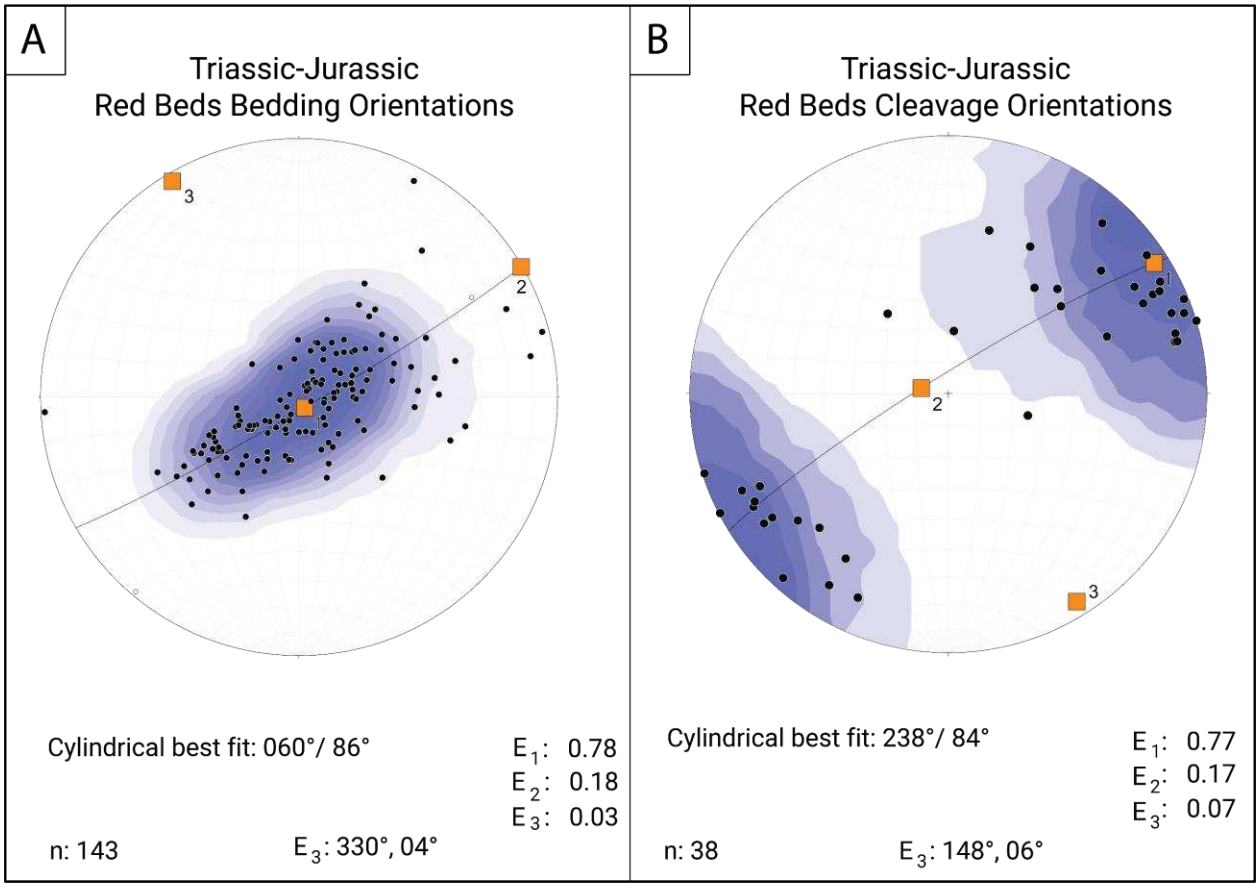

Figure 25. Stereoplots of Triassic-Jurassic red bed structural orientations, plotting poles-to-planes, best fit great circle, and eigenvectors. Annotated below are great circle orientations, eigenvalues, number of measurements, and E_3 orientations. (A) Bedding orientations within the red beds. (B) Cleavage orientations within the red beds.

mean cleavage plane (n=38) is oriented 148°, 84° (Figure 25) with a relatively high P-value (0.60) compared to the G- and R-values (0.20 and 0.21, respectively). The girdle distribution corresponds to an axis oriented 148°, 06° (Figure 25).

13.3. Faults in Triassic-Jurassic Red Beds

Triassic-Jurassic red beds record multiple distinct fault populations. Altogether 214 total faults were measured, not including slickensided barite veins or faults with barite mineralization (n=125), with 55 strike-slip faults, 59 thrust/reverse faults, 12 low-angle strike-slip faults (<30°

dip with a slickenline rake of <45°), 5 normal faults, 4 high-angle reverse faults (>60° with a slickenline rake of >45°), and 83 faults of unknown slip. Slip sense on these faults was determined using offset markers, quartz slickenfibers, and/or Riedel shears. Most strike-slip and thrust faults are outcrop-scale, and where rare offset markers were observed indicate cm-scale displacement.

Strike-slip faults (Figure 26a-e) were designated as fault planes dipping >30° with slickenlines raking <45°. Of the 55 strike-slip faults measured, 34 were of known slip sense (Figure 26a). From these known faults, it is clear that most strike-slip faults are compatible as conjugate pairs, with the average right-lateral and left-lateral faults oriented 014°/82° and 079°/65°, respectively. Based on this pattern, a slip sense was assigned to strike-slip faults with unclear kinematics. I assumed right-lateral faults strike between 359–029° and 179–209° and left-lateral faults strike between 64–94° and 244–274°, with a slickenline rake of <45° (Figure 26b). NE-striking right-lateral strike-slip faults are much more abundant than the left-lateral set, making up 74% of the faults with a known sense of slip (25/34) and most likely ~69% of (38/55) of the total measured strike-slip fault population. The mean P-axis (incremental shortening axis) from all strike-slip faults is oriented 236°, 03°, and the mean T-axis (incremental extension axis) is oriented 326°, 06° (Figure 26d-e). The mean right-lateral and left-lateral fault plane solutions from these data are oriented 014°/78° and 089°/69°, respectively (Figure 26e).

Thrust/reverse faults (Figure 26f-j) were designated as fault planes dipping <60° with slickenlines raking >45°. Of the 59 dip-slip faults with <60° dip, 34 record thrust slip sense (Figure 26f). The remaining <60° dip-slip faults were assumed to have a thrust sense of slip (Figure 26g). Low-angle (<30°) faults with slickenline rakes <45° were separated as low-angle strike-slip faults, and no measured normal faults dip <65°. This criterion resulted in high confidence in the assumed

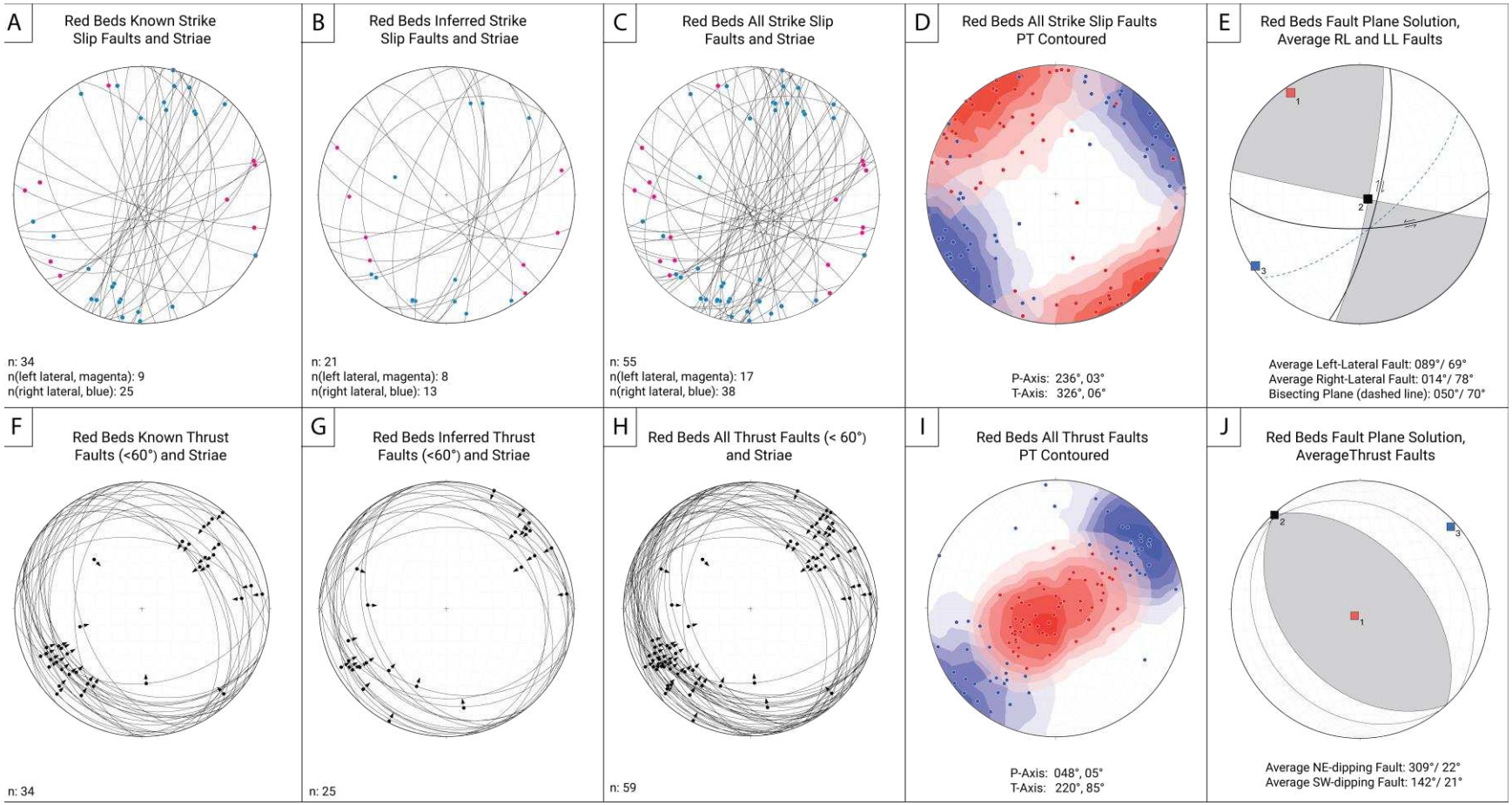

Figure 26. Stereoplots of the Triassic-Jurassic red bed faults. Strike-slip and thrust faults are distinguished by those where slip sense is known, slip sense is inferred, and the aggregate of both known and inferred faults, P-axes (blue) and T-axes (red) were calculated using FaultKin (Marrett and Allmendinger, 1990; Allmendinger et al., 2011; Allmendinger, 2016)*, and fault-plane solutions from linked Bingham mean P- and T-axes are presented alongside average conjugate faults for both fault types.*

slip sense for thrust faults. The total thrust fault dataset records a mean P-axis oriented 048°, 05° and a T-axis oriented 220°, 85° (Figure 26i). One notable apparent ENE-vergent thrust fault exposed on the southeastern wall of Cañón El Alamar is associated with a fault-bend fold in the red beds (Figure 27). Estimated thrust displacement of this fault is ~40 m.

Strike-slip and thrust faults appear to mutually cross-cut one another. Examples include waypoint S573 (UTM: 14 R 408250 2719035), where a strike-slip fault oriented 113°/80° is cut by a thrust fault oriented 232°/29°. Further south, at waypoint S578 (UTM: 14 R 408263 2718811), a thrust fault oriented 231°/06 is cut by a right-lateral strike-slip fault oriented 001°/87°. Neither of these faults contain barite mineralization. These relationships and the consistent NE-SW trending shortening axes suggests that strike-slip and thrust faulting were coeval, and that σ_2 and σ_3 must have been similar in magnitude during shortening.

Other faults (Figure 28) measured include: 8 faults with strike-slip slip sense along shallowly-dipping planes (<30°)(Figure 28a), 5 normal faults (Figure 28c), 4 high-angle (>60°) reverse faults (Figure 28d), and 83 faults with unknown slip sense, including 48 without measured slickenlines (Figure 28b). Low-angle strike-slip faults have NE-SW trending slickenlines and are most likely either gently-dipping portions of undulating thrust faults or lateral ramps of minor thrust faults. Two of the 83 faults with unknown slip sense are bedding parallel.

Measured normal faults all dip steeply (66–86°) and occur adjacent to high-angle reverse faults. The high-angle normal and reverse faults all have low-magnitude offset (<3 m) and are concentrated at specific areas in Cañón El Alamar (Plate 1). At multiple localities in Cañón El Alamar, high-angle normal faults cut bedding-parallel slip surfaces.

Figure 27. Fault-bend fold within the Triassic-Jurassic red beds on the eastern wall of Cañón El Alamar. Estimated offset is ~40m, recording ENE vergent thrust fault slip. The pictured fault is one of the largest of the study area.

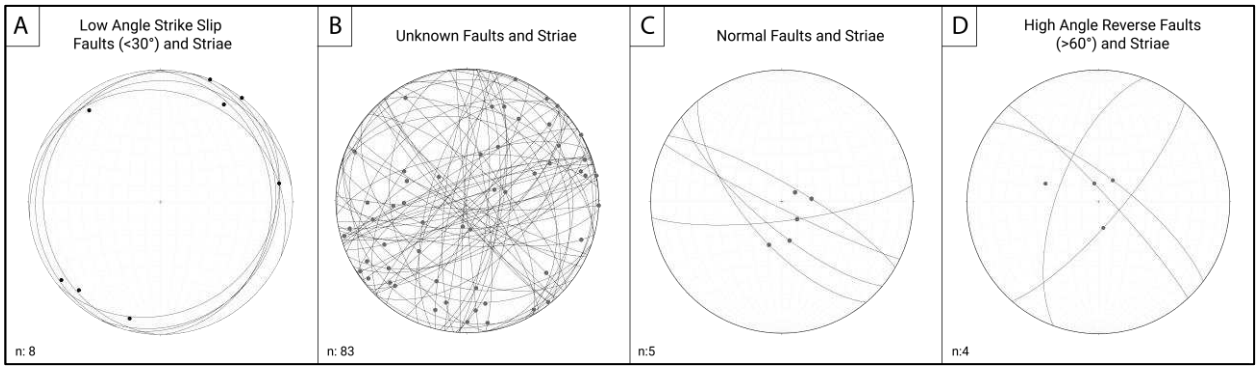

Figure 28. Stereoplots of other faults measured within the Triassic-Jurassic red beds, plot planes and slickenlines and annotated with number of measured faults. (A) Low-angle strike-slip faults. (B) Unknown faults and slickenlines. (C) Normal faults and slickenlines. (D) High angle reverse faults.

The previously mentioned normal fault at the mouth of Cañón El Alamar dips moderately to the NE. Slickenlines were not observed, but the fault exposes as a ~1.5 m thick gouge zone. Apparent offset of the Río de San José Member of the Minas Viejas Formation against the red

beds is most likely in the range of 50–70 m. This normal fault appears to sole into a bedding-parallel slip surface within the Río de San José Member, as it does not cut overlying strata (Figure 29). Given the thickness attenuation in the hanging wall and the proximity to gypsum immediately northeast of the normal fault, the unit labeled as the Río de San José Member in Figure 29 likely contains evaporite, though does not appear present in the footwall.

13.4. Regional Structural Variations the North and South Potosí Uplift

Triassic-Jurassic red bed structures vary between the northern and southern Potosí uplift. Bedding, cleavage, extension fractures, and fault orientations record different mean values, and barite veins are more prevalent near the northern end of the Potosí uplift, while minor faults are more abundant in the southern end.

The northern Potosí uplift is designated by exposures of red beds in Tranquitas and Santa Clara (Figure 14). Average bedding (n=104) in the northern Potosí uplift is oriented 184°/06° (Figure 30a). Bedding is locally overturned within meter-scale folds, though overall most beds dip gently to the ENE or WSW, with only 8 of the 104 measurements dipping >45°. Poles to bedding form a point maxima with a P-value of 0.70, with some distribution along a weakly developed girdle (G-value of 0.18) corresponding with an axis oriented 342°, 02° (Figure 30a).

Cleavage is present in finer-grained intervals of the Triassic-Jurassic red beds in the northern Potosí uplift, specifically surrounding Santa Clara (Figure 14). The mean cleavage plane (n=13) is oriented 332°/82°, with a regionally consistent orientation given a P-value of 0.82. A minor girdle distribution (G-value of 0.16) corresponds to an axis oriented 339°, 38° (Figure 30b).

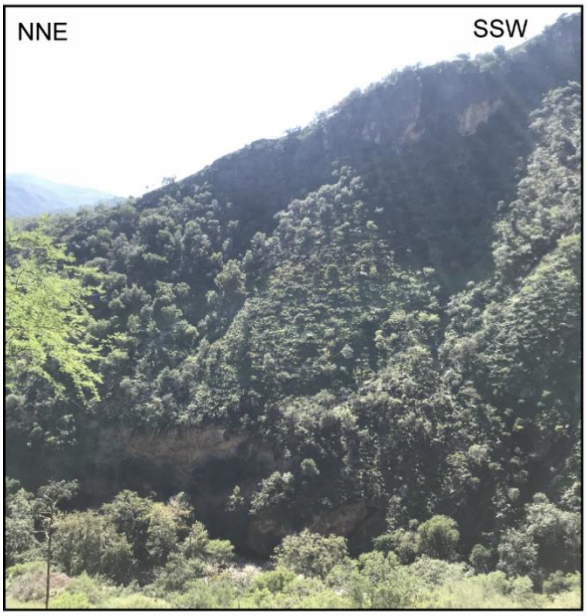

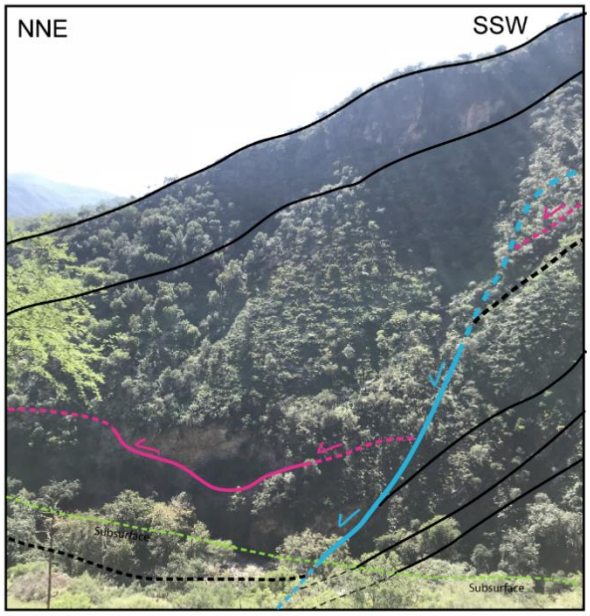

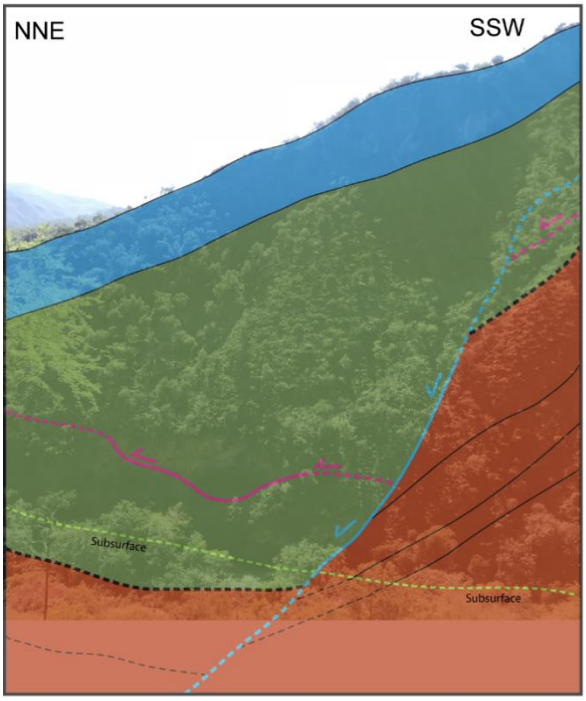

Jurassic Minas Viejas Formation carbonate

Jurassic Minas Viejas Formation - Rio de San Jose Member

Triassic-Jurassic red beds

Figure 29. The mouth of Cañón El Alamar exposes a normal fault, displacing the Jurassic Rio de San Jose Member of the Minas Viejas Formation. This fault (blue) appears to offset a thrust fault (pink) which has structurally thickened the Rio de San Jose Member. The contact with the Triassic-Jurassic red beds do not crop out but are suspected to be at depth (below the green line) in the hanging wall, and is likely present in the footwall. It is also likely that the normal fault roofs into a bedding-parallel slip plane as the overlying carbonates within the Minas Viejas Formation do not appear offset at the rim of the canyon.

The mean joint set (n=56) in the northern Potosí uplift is oriented 071°/89° and forms a high point maxima (P-value 0.86), with minimal girdle or random distribution (G-value and R-value are 0.08 and 0.06, respectively) (Figure 30c). A second joint set (n=10) with a mean orientation of 312°/79° is weakly developed and less prevalent, and joint-intersections with the ENE-striking set indicate this second joint set is younger.

The southern Potosí uplift is designated by exposures of red beds in Cañón El Alamar, La Purísima, and surrounding localities (Figure 14). Within the southern Potosí uplift, average bedding (n=91) is oriented 258°, 03° (Figure 30e). Bedding overall is gently to moderately dipping with only 4 of the 91 measurements dipping >45°. Bedding distribution forms a girdle with consistent dip directions to the northeast and southwest, but given the low dip magnitude these data have a high P-value (0.65). The G-value and R-value are 0.28 and 0.06, respectively. The girdle corresponds with a fold axis oriented 326°, 03° (Figure 30e).

The average cleavage plane (n=22) in the southern Potosí uplift is oriented 142°/74° (Figure 30f). Cleavage has a consistent orientation with a P-value of 0.58, though it appears to have been gently folded about a subhorizontal NW-trending axis oriented 322°, 03° (Figure 30f), yielding a G-value of 0.24.

The most well-developed joint set (n=51) measured in Cañón El Alamar are consistently oriented ENE-WSW; the average plane is oriented 245°/88° (Figure 30g). A perpendicular joint set in this area appears to be younger, less developed, and less prevalent – similar to the younger joint set in the northern Potosí uplift.

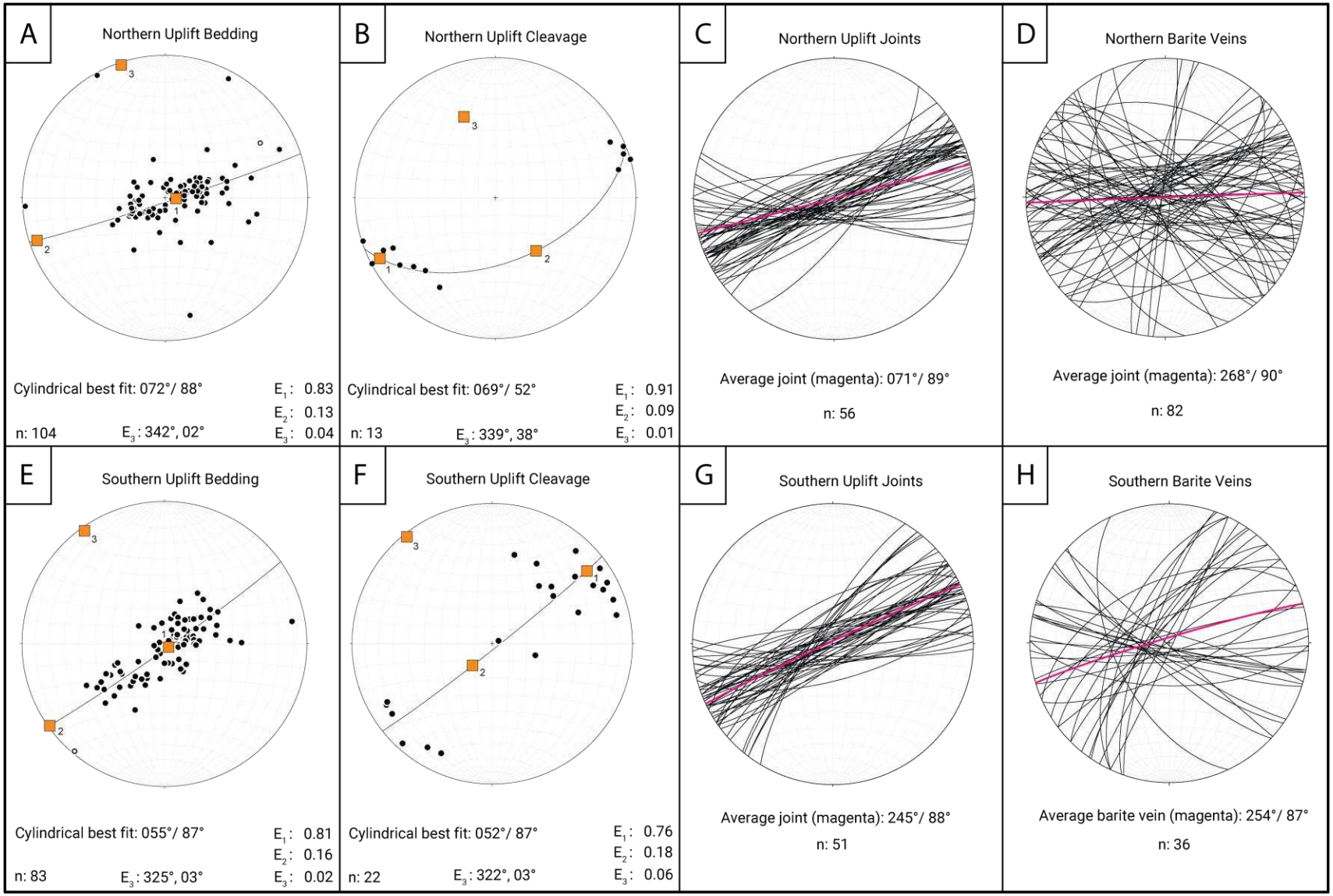

Figure 30. Stereoplots highlighting regional structure variations between the northern and southern parts of the Potosí uplift, including orientations of bedding, cleavage, joint sets, and barite veins.

13.5. Barite Mineralized Faults

Barite veins in the Triassic-Jurassic red beds are most prevalent in the northern Potosí uplift near Tranquitas and Santa Clara. These veins vary in thickness, ranging from millimeter-scale to multiple meters thick (Figure 31). They locally parallel extensional fracture orientations and are typically high-angle planar structures, with only 4 of the measured 125 planes dipping less than 45° (Figure 32a). Most of the veins strike ENE-WSW, perpendicular to the trend of the anticlinorium. A rose diagram of the strikes of barite veins indicates a mean vector trending 068°, but the strikes form a moderately bimodal distribution, with the two dominant orientations striking ~77° and ~95° (Figure 32c). Based on the maximum eigenvector of poles to veins, the average plane is oriented 263°/89° (Figure 32b).

Slickensides are nearly always present along vein margins, frequently with multiple orientations. The most common slickenline orientation indicates strike-slip motion, even in cases with apparent dip-slip offset across the mineralized zone. Clear kinematic indicators are rarely preserved within the barite. While slickensides are very common on the vein margins within the barite, they are rarely present along the red beds wall rock and are not associated with brecciation or other fault rock. Some barite vein slickensides exhibit a glassy or polished appearance, and locally barite mineralization is associated with quartz and sulfides. Analysis of the “mirror polished” surface with a Portable X-ray Fluorescence device indicates 68.5% silica values and 25.7% light elements, with minor aluminum, and magnesium.

E-W to NE-SW striking fault zones associated with barite veins commonly place Triassic-Jurassic red beds adjacent to Jurassic Minas Viejas evaporite, previously mentioned in

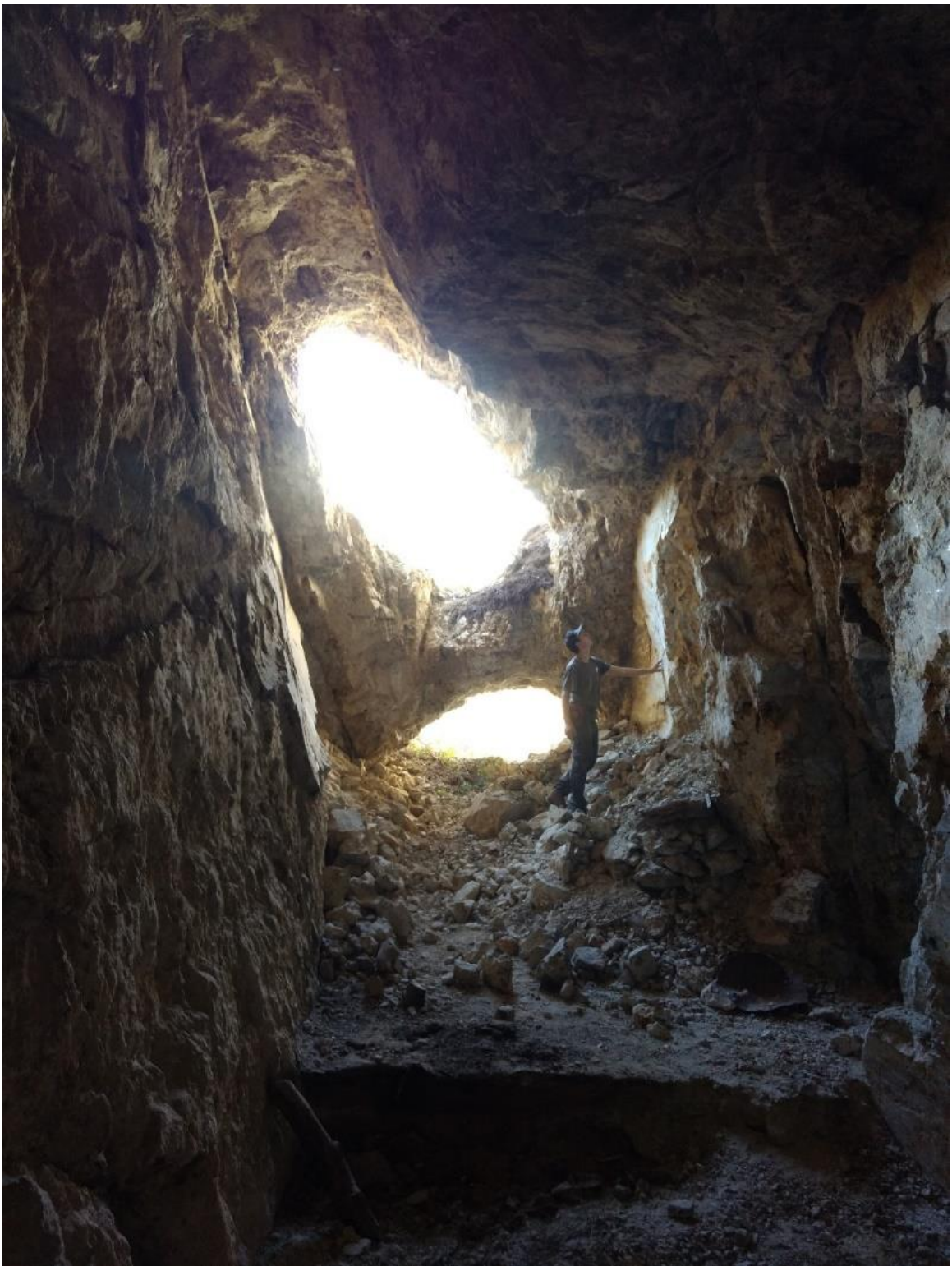

Figure 31. Barite vein located near Tranquitas (Plate 1), ~3 m thick. Graduate student Skyler Mavor for scale with hand on one of many slickensides within the vein.

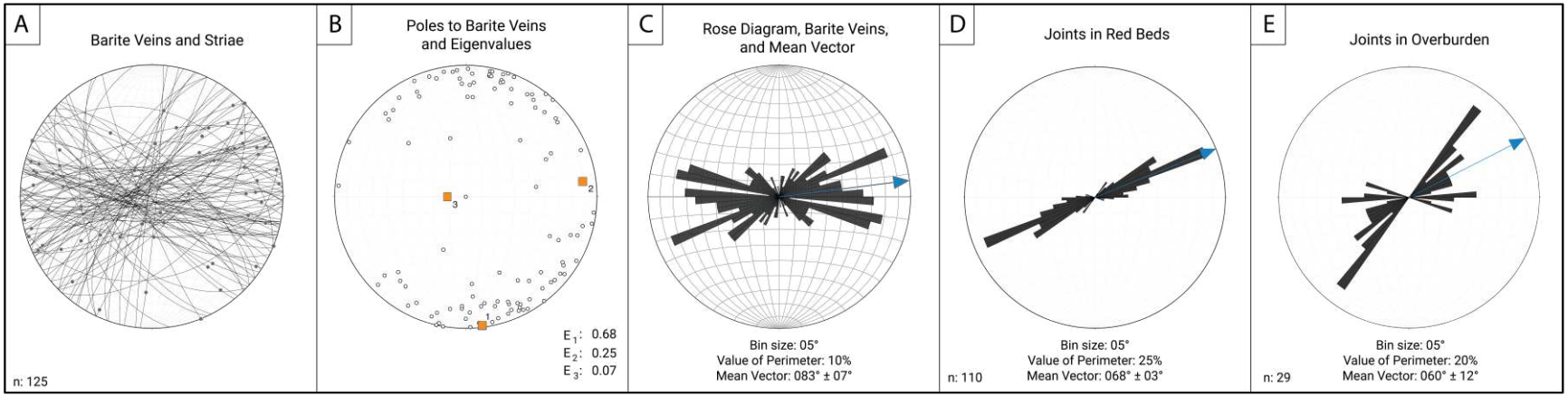

Figure 32. Stereoplots of barite veins and joints within the Triassic-Jurassic red beds. (A) Barite vein planes and slickenlines. (B) Poles-to-planes of barite veins and corresponding eigenvalues and eigenvectors. (C) Rose diagram of barite vein orientations. (D) Rose diagram of joints in red beds. (E) Rose diagram of joints in overburden.

section 13.1. Barite veins consistently cut previously described thrust faults and bedding-parallel slip planes, and the inverse has not been observed at any locality within the study area.

14. Burial and Exhumation History

14.1. Vitrinite Reflectance and Maximum Burial Depth

In Cañón Santa Barbara, a ~3 km-thick section of the Jurassic Minas Viejas Formation is exposed, structurally thickened within an anticline hinge. Approximately 1.3 km stratigraphically down section, an organic rich seam of black shale was identified and analyzed for vitrinite reflectance, an indication of the maximum burial temperature experienced at that specific stratigraphic level. The sample was found to be high rank amorphous kerogen, possibly containing bitumen. Sixty points within the mounted slide were analyzed for $\%R_0$ values, yielding 10 points of suspected contaminants with an average $\%R_0$ value of 0.76, 13 points of recycled vitrinite with an average $\%R_0$ value of 2.18, 15 points of inertinite with an average $\%R_0$ value of 2.53, and 22 points of indigenous sample yielding an $\%R_0$ value of 1.92 (Figure 33).

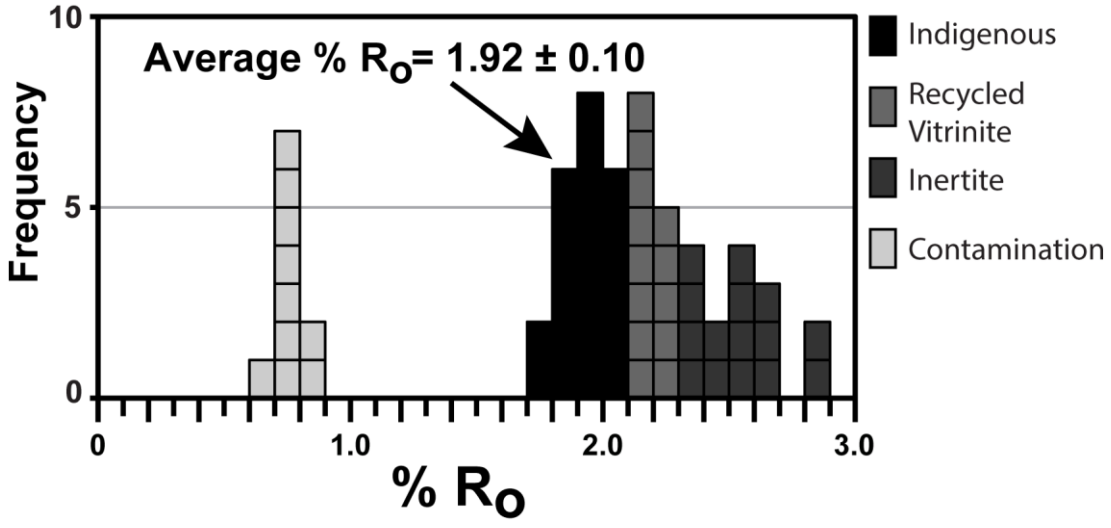

Figure 33. $\%R_o$ results from vitrinite reflectance analysis done by National Petrographic Service Inc.

14.2. (U-Th)/He Thermochronometry Results

Preliminary results of (U-Th)/He thermochronometry within this study were previously reported in Prior et al. (2018) and are further expanded on here. Four samples from the Potosí uplift are from sandstones within the Triassic-Jurassic El Alamar Formation, one sample from the Jurassic La Joya Formation, one sample within a thin sandstone interval within the Jurassic Minas Viejas, one sample within the La Primavera Member in the Minas Viejas Formation, and a sample from a sandstone interval in the Jurassic-Cretaceous La Casita Formation near the contact with the overlying Cretaceous Taraises Formation (Table 1). The oldest ZHe date within the Potosí uplift is 66.4 ± 11.7 Ma, from El Alamar Formation sample SMO18-4 located near La Purísima (Figure 34) in the at the southern end of the Potosí uplift. The youngest ZHe date is 42.5 ± 3.5 Ma, from La Joya Formation sample SMO18-4 located in the northern part of the Potosí uplift near Tranquitas (Figure 34). Two samples overlie the red bed samples, La Casita sample SMO18-6 from the northern end of Cañón de Tomates has a ZHe date of 55.9 ± 9.1, and a Minas Viejas sandstone sample SMO17-MVSS which has a ZHe date of 48.6 ± 3.9. ZHe dates in the Potosí uplift are well correlated with distance along an uplift-parallel transect (R^2=0.746), with the oldest cooling ages in the southeast and the youngest in the northwest (Figure 34, 35). Two samples were also collected within the Aramberri uplift ~50 km south of the Potosí uplift. One sample from a thin metasandstone interval within the metamorphic basement, sample S493 with a ZHe date of 62.7 ± 12.7, and one sample sandstone in the El Alamar Formation, sample SMO18-3 with a ZHe date of 53.9 ± 11.6.

Table 1: Summary of Thermochronology Data from the Potosí and Aramberri uplifts, NE Mexico

Sample	UTM Easting	Northing	Geologic Formation	Lithology	Distance along transect (km)	Mean ZHe Age (Ma)	Std Dev (Ma)	2 Std Err (Ma)
SMO17-MVSS	387921	2732918	Minas Viejas	tan-brown med-grained sandstone	0.7	48.6	4.4	3.9
SMO17-5-29	386103	2730901	La Primavera	pink-gray welded tuff	1.5	42.5	3.5	3.5
SMO17-5-1	388546	2731969	La Joya	red med-coarse grained sandstone	1.8	43.8	3.5	3.2
SMO18-6	401201	2731724	La Casita	Tan med-grained sandstone	8.3	55.9	10.2	9.1
SMO18-1	394461	2726352	El Alamar	red med-coarse grained sandstone	9.6	49.0	10.2	10.2
J156	403283	2721056	El Alamar	red med-coarse grained sandstone	18.6	49.4	9.1	10.5
SMO17-5-43	408313	2719277	El Alamar	red med-coarse grained sandstone	22.7	59.7	10.2	9.1
SMO18-4	415387	2713287	El Alamar	red med-coarse grained sandstone	31.4	66.4	13.2	11.8
S493	410569	2667363	Esquisto Aramberri	gray fine-med grained metasandstone	N/A	62.7	14.1	12.7
SMO18-3	422647	2672542	El Alamar	red med-coarse grained sandstone	N/A	53.9	13.0	11.6

UTM coordinates in WGS 1984

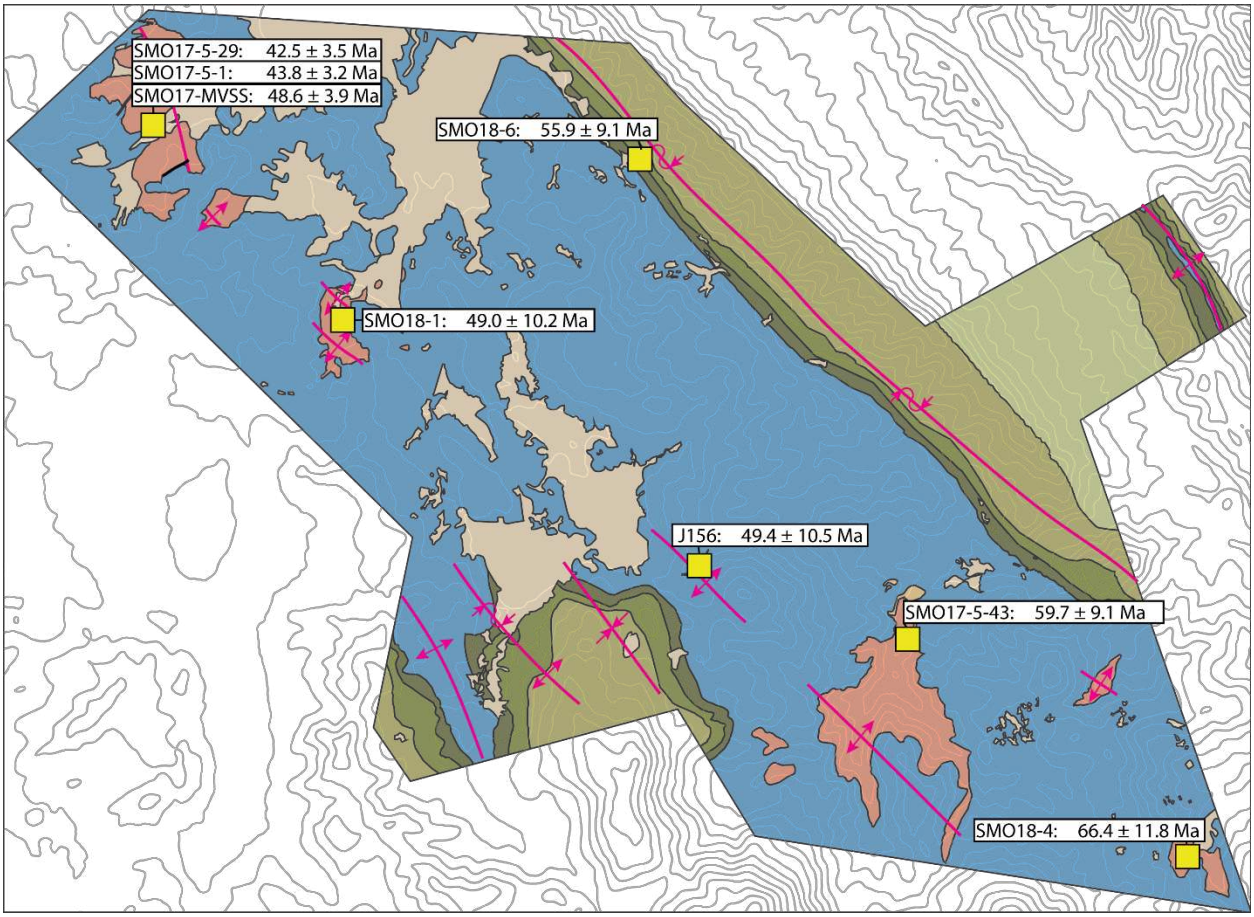

Figure 34. Thermochronology sample names and locations within the Potosí uplift. Reported are ZHe ages reported to two standard error.

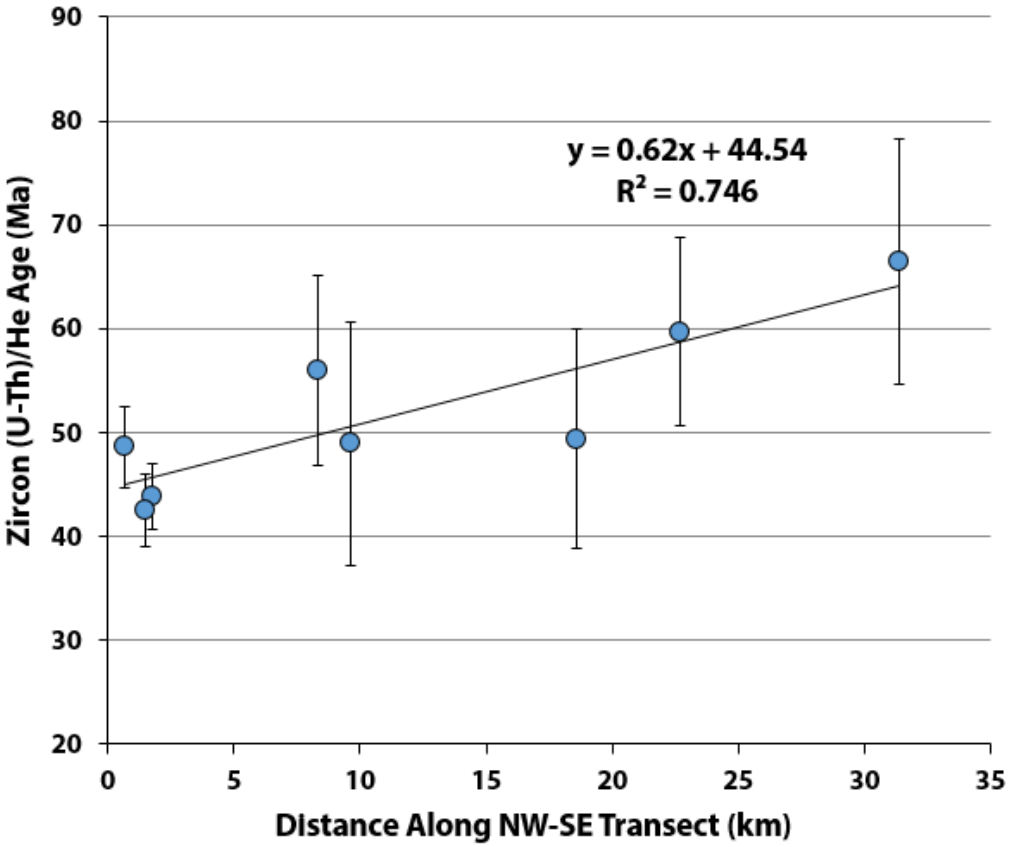

Figure 35. Zircon helium ages of samples vs. distance along NW-SE transect, parallel to the trend of the Potosí anticlinorium (150°-330°) with distance 0 set to the northwestern most Triassic-Jurassic red bed exposures. Does not include Aramberri samples.

DISCUSSION

15. Thin-skinned shortening

Development of the thin-skinned fold-thrust belt was achieved through the formation of a ductile décollement within the Jurassic Minas Viejas Formation. Shortening was primarily accommodated by detachment folding within the Jurassic-Cretaceous overburden strata. In addition, overburden strata record layer-parallel shortening via pressure solution that formed stylolites perpendicular to the shortening trend. These stylolites are consistently oriented perpendicular to rotated bedding, suggesting they formed during early stages of thin-skinned shortening, prior to folding. Post-stylolite extensional fractures record NNW-SSE extension that is kinematically compatible with WSW-ENE thin-skinned shortening (Figure 16).

Variations in the basal stratigraphy within the Jurassic Minas Viejas Formation resulted in different styles of deformation within the décollement. Where the basal member is evaporite, such as the La Nieve Member in the northern end of the uplift, the lower décollement boundary developed as a non-coaxial shear zone. Where the basal member is the shale-rich Río de San José Member in the southern part of the uplift, deformation was brittle-ductile. Though these two mechanisms are different, they both accommodated translation of overburden strata and thin-skinned detachment folding with minimal deformation to the subdécollement red beds. Mean orientations in the basal stratigraphy suggest geometric compatibility with one another (mean foliation within the La Nieve Member shear zone oriented 151°/27°, and mean bedding within the Río de San José Member oriented 139°/28°), and kinematic indicators (foliation orientations and microstructures such as strain fringes) in both basal sections record top-to-the ENE shear,

accommodating translation of overburden strata towards the foreland. While geometry and kinematics mirror one another, magnitude of strain are not the same. Foliation within the La Nieve Member shear zone is at a low angle (<10°) to bedding, and evaporite nodules have been completely transposed into mylonitic fabrics; meanwhile, foliation in the Río de San José Member is at a higher angle (~20–30°) to bedding and concentrated only in finer-grained intervals, with original sedimentary structures preserved through most of the member. These observations suggest the La Nieve Member shear zone records significantly larger strain magnitudes while the Río de San José Member, though sheared, records less strain, despite being at the same stratigraphic level.

Given the thickness variations of the Minas Viejas Formation beneath overburden synclines and anticlines, evacuation and/or shear-related attenuation aided in removing the mechanically weak gypsum. Within the synclinal keel just west of Anticlinal Craneo (Plate 1), no exposure of gypsum was found in the Minas Viejas Formation; instead, only carbonate and shale intervals appear to be present between the red beds and Jurassic-Cretaceous La Casita Formation, requiring evacuation of nearly all gypsum that may have been in between. A tuffaceous interval similar to the La Primavera Member of the Minas Viejas Formation was identified in Cañón Santa Barbara (Plate 1) only ~40 m stratigraphically above the red bed contact. In Tranquitas, the La Primavera Member is ~400 m above the red bed contact, with ~215 m of carbonate and ~185 m of evaporite. Assuming complete evacuation of evaporite, this thickness variation would still require significant depositional differences within the carbonate interval (thinner to the south), a likely possibility given the basal stratigraphic differences

between the La Nieve Member and the Río de San José Member, or significant thinning of carbonate intervals, which has not been observed throughout the uplift.

While the La Nieve Member records a discrete non-coaxial shear zone in the northern part of the uplift, where it marks the lower décollement, throughout the central and southern part of the uplift it is clear that shear was not localized along a single discrete shear zone, but rather throughout the entirety Jurassic Minas Viejas Formation. The lack of strain localization most likely reflects variation in mechanical stratigraphy, wherein a lack of evaporite at the stratigraphically lowest section resulted in more distributed non-coaxial strain throughout the entire formation. While stratigraphic strength variations would theoretically cause a "jump" up or down to the next weakest boundary parallel to the pre-existing structure, the lack of the basal La Nieve Member evaporite in the southern part of the uplift and presence of the laterally discontinuous Río de San José Member shale likely caused perturbations to the stress-strain fields that resulted in more distributed strain throughout the Minas Viejas Formation, as opposed to concentrating it at the stratigraphically deepest level.

16. Thick-skinned shortening

16.1. The Potosí Anticlinorium Geometry and Overall Kinematics

The NNW-SSE trending Potosí anticlinorium records systematic folding and cleavage development in response to ENE-WSW shortening. In most localities, bedding consistently dips gently E to NE or W to SW. These beds have been folded along an average fold axis oriented 330°, 04° (Figure 25). The overall fold axis, the symmetrical spread of data about that fold axis, and the magnitude of overall bedding dips indicates that the uplift is a broad-scale horizontal upright or

steeply inclined anticlinorium with open-to-close interlimb angles. Red bed exposures across the uplift are nearly all located within ~4–5 km of the anticlinorium hinge (Figure 14), and do not fully represent the geometry of the anticlinorium. The limbs of the anticlinorium are not well exposed within the Potosí uplift and as such, bedding data do not record asymmetry. However, mapped contacts with the Minas Viejas Formation and Jurassic-Cretaceous overburden strata record an elevation difference across the uplift. This elevation variation is the result of asymmetry in the underlying strata, where exposures in Cañón El Alamar (Figure 14) and overburden elevations indicate a gently-dipping WSW anticlinorium limb, and overburden elevations indicate a moderately-dipping ENE limb (Plate 1). This geometry would indicate overall ENE-vergent shortening.

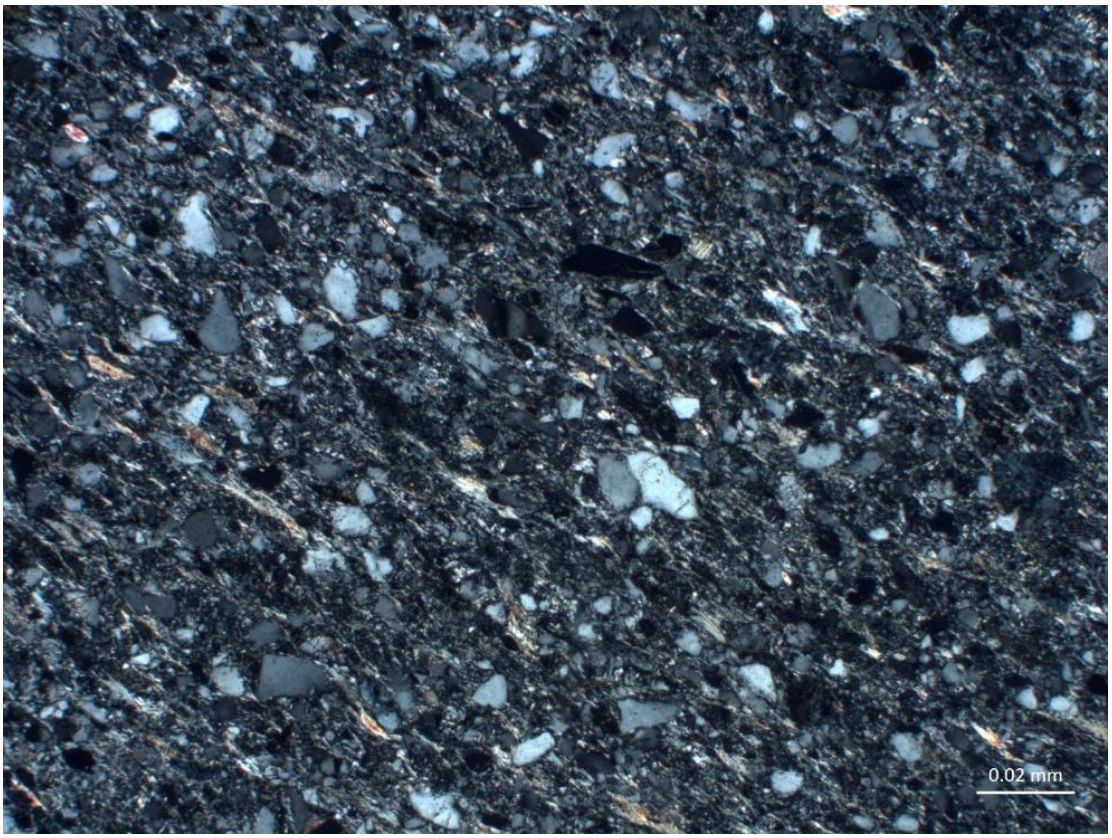

Figure 36. Photomicrograph of fine-grained sandstone in the El Alamar Formation from Cañón El Alamar (sample S570; Figure 14; Plate 1). Aligned white micas weakly define the steep NW-striking cleavage observed at the outcrop

Cleavage within the red beds is defined by metamorphic white mica growth as well as pressure solution seams (Figure 36). Cleavage likely formed during development of the anticlinorium and was slightly reoriented as folding progressed, as indicated by the moderate G-value (0.20) about an axis oriented 148°, 06°. This trend is nearly identical to the overall fold axis determined by bedding, 330°, 04°, with the mean cleavage plane, oriented 148°/84°. This plane strikes nearly parallel to the trend of the upright to steeply SW inclined anticlinorium, indicating that cleavage developed axial planar to the broad-scale anticlinorium.

Minor fault data analyzed within the red beds indicate NE-SW subhorizontal shortening. The strike-slip fault population indicates a mean P-axis oriented 235°, 02° and a T-axis oriented 325°, 06° (Figure 26d). The thrust fault population indicates a mean P-axis oriented 046°, 06° and a T-axis oriented 214°, 84° (Figure 26i). Both strike-slip and thrust faults are kinematically compatible with the overall geometry of folding within the red beds, which indicate NE-SW horizontal shortening. The perpendicular NW-SE and subvertical extensional directions recorded by coeval strike-slip and thrust faults suggest that finite strain was predominantly uniaxial during thick-skinned shortening, with flattening along a subhorizontal NE-SW axis.

16.2. Barite Mineralization and Outer-arc Extension

Kesler et al. (1988) suggest barite mineralization occurred ~30 Ma based on the Rb/Sr isotopic ratio in both the barite and the Triassic-Jurassic red beds, with no error given. However, based on the same assumptions used by Kesler et al. (1988), I could not duplicate the same timing, instead producing a poorly-constrained age of ~55–135 Ma. This calculation is based on the Rb-Sr PPM concentrations reported in Kesler et al. (1988), the subsequent ratio of $^{87}Rb/^{86}Sr$

by using their atomic weights (0.2783 and 0.0986, respectively), and creating an isochron in Isoplot (2011). This isochron suggests an initial $^{87}Sr/^{86}Sr$ concentration (0.7102 ± 0.0018) and an age (161 ± 32 Ma). Plotting these values, along with the barite $^{87}Sr/^{86}Sr$ concentrations from Kesler et al. (1988), within one standard deviation gives a range of ~55–135 Ma for barite mineralization based on the intersecting values.

Barite veins and slip surfaces are dominantly oriented perpendicular to the strike of the anticlinorium (Figure 32a-b; Plate 1), locally recording significant dilation with the larger veins up to 5 m thick. This orientation indicates extension perpendicular to the strike of the anticlinorium in the majority of barite veins. Barite vein structures originated as predominantly opening mode fractures, indicated by their relatively thick nature and lack of brecciation and fault plane indicators on the wall rocks. Shear along the barite vein margins is most likely related to the low coefficient of friction for the barite, ~0.48 (Shimamoto and Logan, 1981), and possible high fluid pressure. Slickenlines within the barite veins are typically subhorizontal, indicating strike-slip motion, thought offset strata primarily suggest high-angle normal offset and minor high-angle reverse offset.

Regional elevations of red bed exposures require a non-cylindrical, doubly-plunging fold geometry to the anticlinorium (Plate 1), with the red beds at ~1300m in La Purísima at the southern end of the uplift, ~2000m in Tranquitas, near the suspected center of the uplift, and inferred to be ~900-1300m north of the study area near Galeana based on regional cross sections (Padilla y Sánchez, 1985; Götte, 1988; SGM, 2010a). During folding of a competent layer, outer-arc extension is typically accommodated by the formation of extension fractures parallel to the trend of the fold (Figure 37). If folding is non-cylindrical, it is expected that outer-arc extension

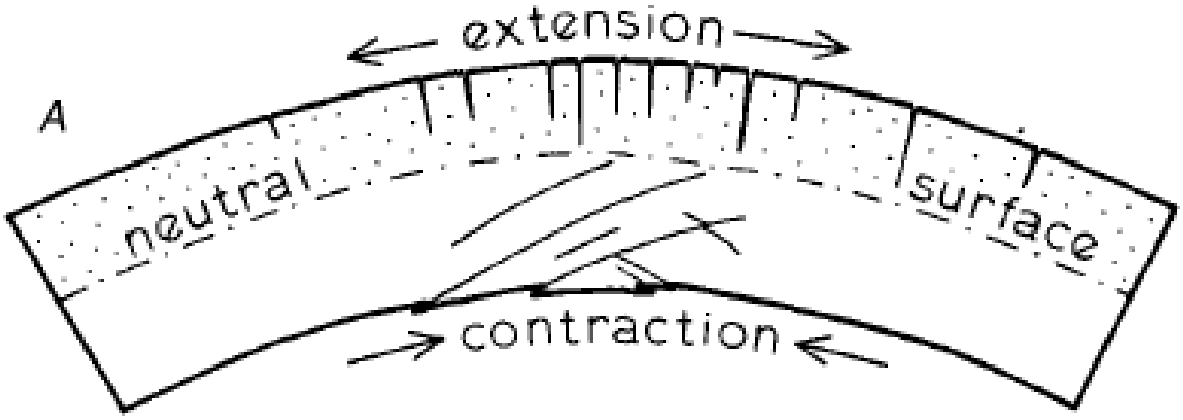

Figure 37. Relationship between folding, extension fractures, and the neutral surface. Figure from (Bradley and Kidd, 1991)

may accommodate extension both parallel and perpendicular to the trend of the fold if the extent of folding is large enough in either direction (Figure 38). Recent studies have suggested that extension can also be accommodated not only by extension fractures, but also minor faulting nearest the hinge, named “bending-moment faults”, or “extrados faults” (Bradley and Kidd, 1991; Fiorini and Tibaldi, 2012; Livio et al., 2018, 2019; Tibaldi and Bonali, 2018). Bending-moment faults are outer-arc extensional structures typically associated with large-scale tectonic settings such as subduction zones and often bound fault blocks in the outer-arc with minimal horizontal-axis rotation, accommodating extension through fault slip (Bradley and Kidd, 1991). Bedding orientations throughout the anticlinorium do suggest cylindrical folding about a subhorizontal axis, as there is no observed fold axis plunge in the northern nor southern uplift. Certain fault blocks, however, may dip towards the hinge of the arc, others away, and commonly fault blocks retain the same subhorizontal dip orientation from a pre-deformational state relative to the neutral surface of the fold (Fiorini and Tibaldi, 2012; Livio et al., 2018, 2019; Tibaldi and Bonali, 2018). Folded bedding and cleavage in the Santa Clara area (Figure 30; Plate 1) records fold axes

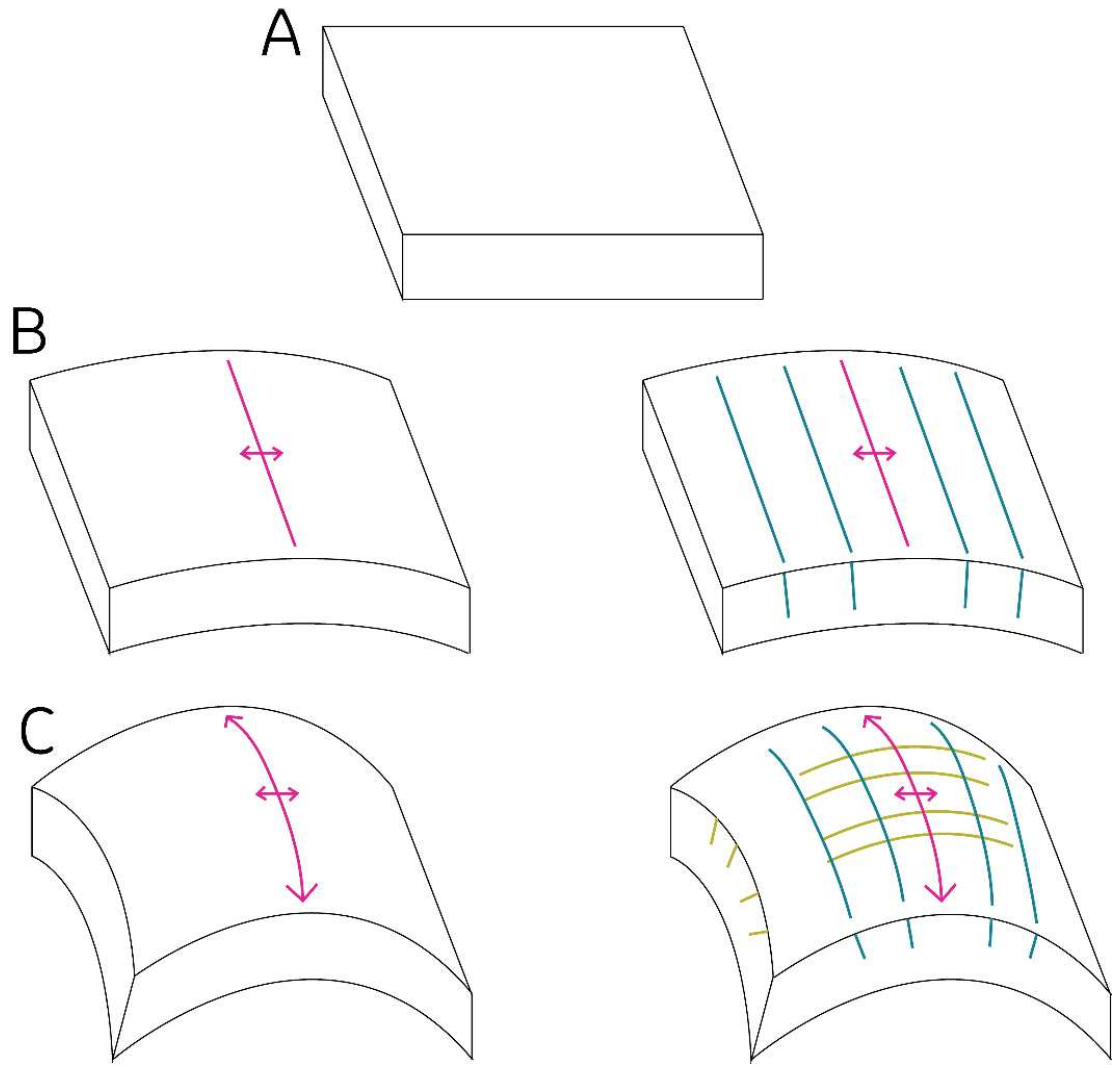

Figure 38. Expected extension fracture orientations in cylindrical and non-cylindrical folds. (a) a neutral flat block. (b) a block that has been folded along a cylindrical axis (pink), creating extension perpendicular to the fold axis through outer-arc extension (blue). (c) a block that has been folded along a non-cylindrical axis (pink), creating extension both parallel (green) and perpendicular (blue) to the primary fold axis, which is plunging on both sides. Though extension fractures and their orientations can be much more complex, this extremely simplified model may still apply to the Potosí uplift.

plunging gently-to-moderately northwest, suggesting anticlinorium folding is not perfectly cylindrical along the uplift. A non-cylindrical fold geometry combined with bending-moment faults would allow for extension perpendicular to the trend of the uplift without plunging the northern or southern extents of the uplift, as observed within the study area (Figure 39). Early development of the anticlinorium resulted in outer-arc extension, creating vertical to subvertical

extension fractures and minor dilation parallel to the anticlinorium axis. Following fracture development in the red beds, fluids containing barium from the Triassic-Jurassic red beds and sulfate from the Jurassic Minas Viejas Gypsum mixed, mobilize, and precipitated barite (Kesler et al., 1988). The low coefficient of barite allowed for extension fractures to slip under low shear stress, forming strike-slip faults and bending moment dip-slip faults. Bending-moment faulting further accommodated extension with minimal tilting of bedding to the NNW or SSE, supported by predominantly normal-sense offset across high-angle barite veins, though certain fault blocks rotated to some degree (i.e., in the Santa Clara area). After normal-sense offset, the barite veins continued accommodating subhorizontal shortening through strike-slip motion, resulting in predominantly subhorizontal slickenlines within the barite.

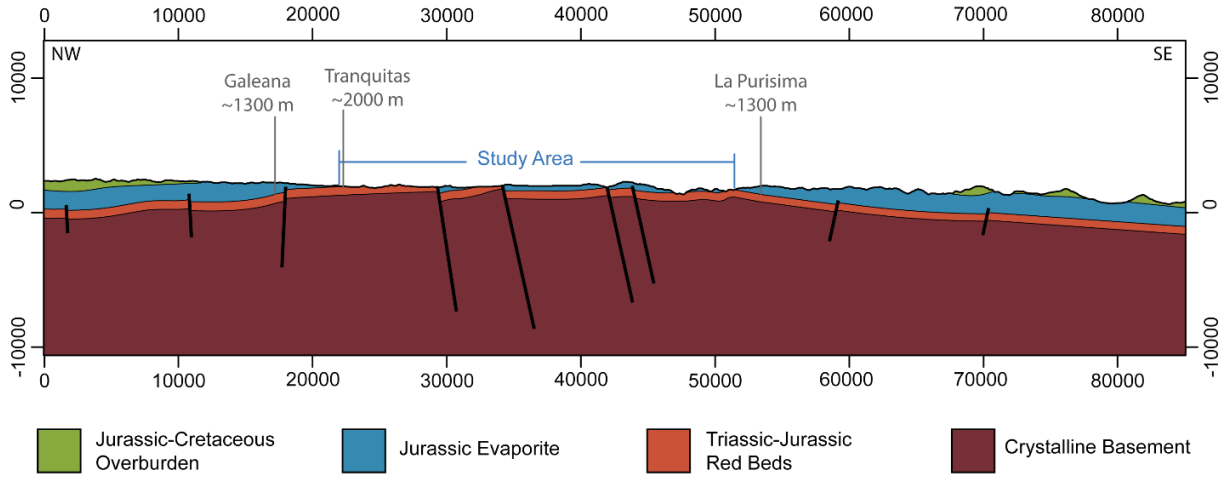

Figure 39. Diagram of the Potosí uplift highlighting extent of Triassic-Jurassic red bed exposures and likely geometry of the anticlinorium to allow for bending-moment faults to form and slip. In the given orientations, subhorizontal bedding within the fault blocks would suggest cylindrical folding, though the regional exposures and depths of red beds would suggest non-cylindrical folding given the current elevation of Jurassic-Cretaceous overburden to the north and south of the Potosí uplift. Shown in grey are elevations above sea level of red bed contacts with the overlying Minas Viejas Formation, which requires either fault offset or a doubly-plunging fold.

I suggest that outer-arc, axis-parallel extension associated with the development of the non-cylindrical, doubly-plunging Potosí anticlinorium accommodated barite veining. Barite

mineralization allowed these planes to slip, forming bending-moment faults that accommodated additional minor extension, as evidenced by rotation of bedding and cleavage fold axes in the Santa Clara area. While red beds near Santa Clara appear to record rotation associated with outer-arc extension, other outer-arc fault blocks have remained sub-horizontal.

16.3. Thick-Skinned Modification of Overburden Folds

Jurassic-Cretaceous overburden detachment folds formed during thin-skinned deformation have been modified by thick-skinned deformation across the Potosí uplift. Assuming detachment folding resulted in equal elevations of detachment fold hinges (Padilla y Sánchez, 1982, 1985; Fischer and Jackson, 1999; Marrett and Aranda-García, 2001; Higuera-Díaz et al., 2005), it is clear that the regional syncline and anticline hinge elevations have been raised within the uplift (Plate 1).

Chevron folds in Jurassic-Cretaceous overburden within the southwestern limb of the Synclinal Providencia are incompatible as parasitic folds for thin-skinned folding. These chevron folds also record folding of cleavage, interpreted as being axial planar to thin-skinned detachment folding within the La Casita Formation, forming a girdle distribution for poles-to-cleavage with a G-value of 0.44 about an axis oriented 147°, 12° (Figure 19). The location of the chevron folds on the flank of the uplift as well as the geometry and elevations of Jurassic-Cretaceous overburden folds adjacent to the uplift suggest that these chevron folds are the result of secondary deformation associated with thick-skinned uplift. Chevron folds on the eastern flank of the uplift appear to extend for ~25 km NNW from the northeastern corner of the study area (Plate 1), north of Galeana. As uplift occurred to the southwest of the Synclinal

Providencia, and strata were rotated in a top-to-the northeast sense along a subhorizontal axis trending parallel to the strike of the anticlinorium. The Anticlinal Giro Pequeño, located southwest of the anticlinorium hinge (Plate 1), is another example of chevron folding incompatible with thin-skinned folding as parasitic folds. The Anticlinal Giro Pequeño also records a top-to-the-northeast sense of rotation.

Thick-skinned uplift of the anticlinorium refolded thin-skinned structures. Subvertical synclinal limbs were preferentially refolded, while anticline hinges primarily experienced simple translation. This discrepancy may be the result of the ability of the Jurassic Minas Viejas evaporite to dampen and absorb strain within anticline cores, while synclinal keels were more proximal to the uplifting red beds without the evaporite buffer.

16.4. How Thick-skinned Uplift was Accommodated

Shortening associated with thick-skinned uplift was predominantly achieved through the development of the anticlinorium, with layer-parallel shortening accommodated by minor thrust faulting and strike-slip faulting, and cleavage development. While magnitude was not measured, layer-parallel shortening through pressure solution in siliciclastics typically ranges from 3–21%, depending on extent of deformation and lithology (Whitaker and Bartholomew, 1999; Henry et al., 2003). Minor thrust faults all indicate shortening at low angles to bedding (Figure 26). The largest observed structure in the study area is a previously described ENE-vergent thrust fault in Cañón El Alamar associated with a ramp-flat geometry with ~40 m of offset and contained entirely within the red beds (Figure 27). Timing of minor faulting in relation to the development of the anticlinorium is not well constrained. Within Cañón El Alamar, thrust faults are typically

dipping 10-30° steeper than bedding, suggesting early formation of thrust faults relative to the tilting of strata, but more data and correlation are required to confidently indicate a systematic relationship that could suggest relative timing of faulting and folding. The lack of steeply inclined strata (<50°) does not allow for the observation of late-stage thrust faults or rotation of early-stage thrust faults.

In an effort to find exposure of speculated or previously mapped high-angle reverse faults, I explored the area surrounding Galeana and found no evidence of either a high-angle reverse fault or a down-dropped graben, and instead discovered stratigraphic overturned contacts of the Jurassic Minas Viejas Formation with overlying Cretaceous strata. The likelihood of Götte's (1988) graben with 3.1 km of net vertical offset being present in the area, a singular anomalous structure, is highly unlikely for the same argument that can be made against the singular anomalous horst interpretation of Padilla y Sánchez (1985): this region is outside of the extent of the Basin and Range and no significant NNW-SSE striking normal faults are recorded in the area with. As it stands, there is no evidence of high-angle reverse fault reactivation of normal faults, either as the main structure itself or synthetic structures one would expect to find, such as widespread and smaller-scale normal faults.

The anticlinorium, previously described in section 16.2 as a doubly-plunging non-cylindrical fold, required extension both perpendicular and parallel to the fold axis. While barite-bearing veins accommodated outer-arc extension parallel to the anticlinorium strike, measured normal faults are accommodating outer-arc extension perpendicular to the fold axis. The series of high angle normal and reverse faults in Cañón El Alamar supports the previously described interpretation that red beds were in the outer-arc with a deeper neutral surface.

Eliminating horst-and-graben related uplift, the development of the anticlinorium and present geometry of the Potosí uplift was achieved through two possible processes: 1) a deeper décollement/detachment structurally below the Triassic-Jurassic red beds, or 2) high-angle reverse faults, potentially forming as reactivated normal faults (Figure 40). This study has outlined substantial evidence of faults which are kinematically and structurally compatible with the hypothesis of a deeper thrust detachment. Observed faults, ideally synthetic to the larger structure, all suggest a gently-dipping thrust fault at depth with no evidence that high-angle reverse faults are the cause of the thick-skinned uplift or played a role in developing the Potosí anticlinorium. It is likely that the Potosí anticlinorium is rather a large-scale fault-propagation fold or fault-bend fold in the hanging wall of an ENE-vergent detachment at depth. The ENE-vergent geometry of the anticlinorium, the subhorizontal shortening directions recorded by faulting and cleavage, and the observation that the largest fault in the field area is a low-angle ENE-vergent thrust fault all support the hypothesis of a ENE-vergent low-angle detachment.

16.5. Kinematic Variations within the Study Area

In the northern part of the uplift (Figure 30), bedding has been folded into an upright fold about an axis oriented 342°, 02°, suggesting subhorizontal shortening trending 72–252°. The mean cleavage plane is oriented 323°/ 82°, indicating a subhorizontal shortening direction oriented 52–232°. Pole-to-cleavage girdle distribution indicates cleavage was folded slightly about an average axis oriented 339°, 28°. Given the anomalous plunge, it is possible that the in the same direction, albeit smaller in magnitude. Assuming both cleavage development and folding happened prior to development of the NNW plunge, rotating the data to restore an originally

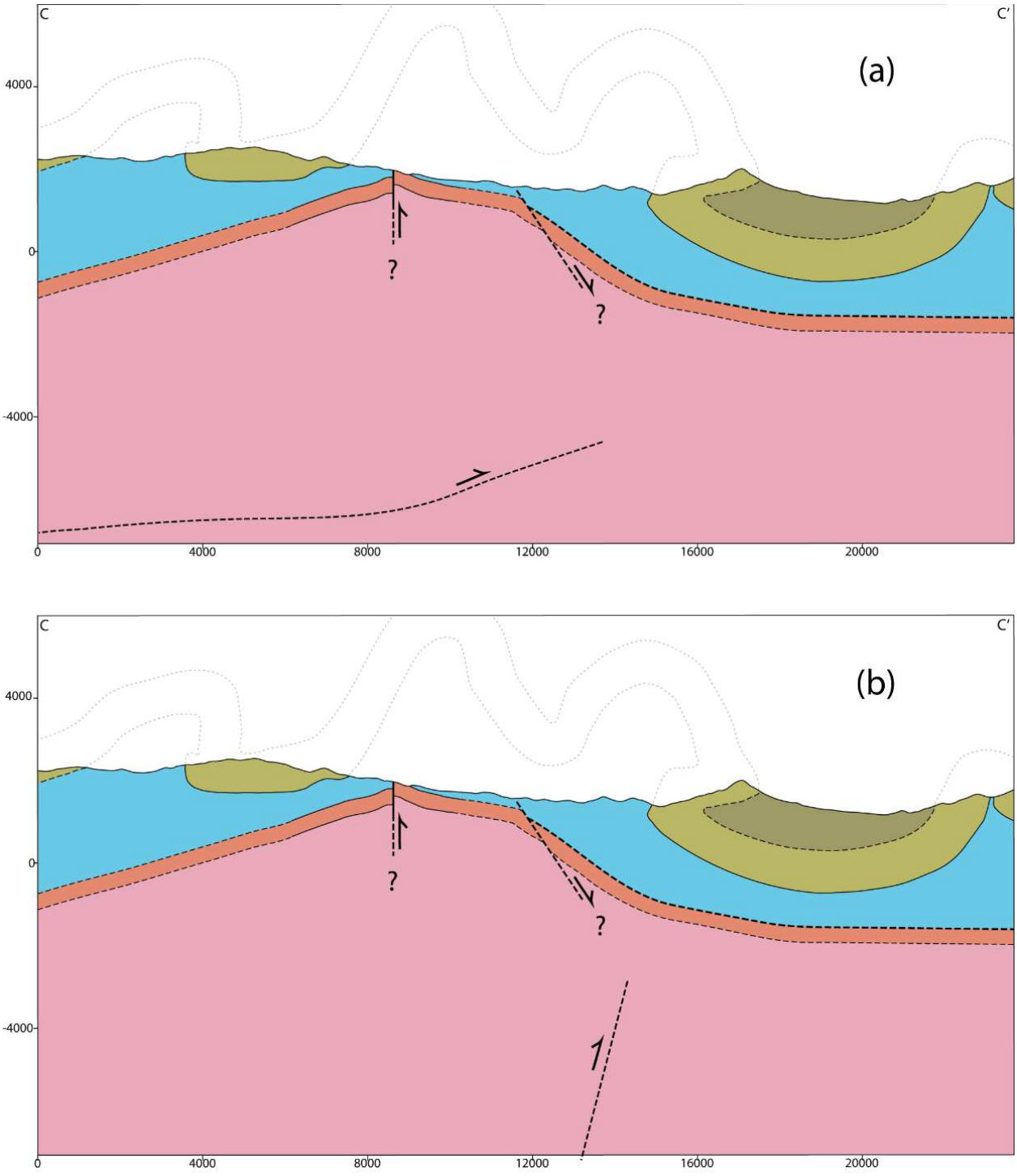

Figure 40. Two proposed models for driving thick-skinned uplift. (a) Thick-skinned uplift is driven by a ENE-vergent low-angle thrust at depth creating a fault-propagation fold that results in the development of the Potosi anticlinorium. (b) Thick-skinned uplift is driven by a high-angle reverse fault, creating a fault-propagation fold that results in the development of the Potosi anticlinorium. In either of these scenarios, the fault would likely not cut the Minas Viejas Formation, which would have ductiley absorbed most or all of the strain.

horizontal fold axis oriented 159°, 00° results in the mean pole-to-cleavage oriented 249°, 10°. With cleavage being axial planar, the given horizontal fold axis would correlate to a horizontal shortening direction trending 69°.

NE- to ENE-striking, steeply-dipping joints in the northern portion of the uplift (Figure 30) within the red beds do not appear to have undergone rotation nor shear, distinguishing them from shear fractures which would form oblique to the shortening direction. The parallelism between the joint strike and the subhorizontal shortening direction from other structures such as cleavage and pressure-solution seams (stylolites) and thrust- and strike-slip faults suggest the joints are kinematically compatible with subhorizontal thick-skinned shortening perpendicular to the anticlinorium trend.

In the southern part of the uplift (Figure 30), bedding has been folded about an axis oriented 325°, 03°, suggesting subhorizontal shortening trending 55–225°. The mean cleavage plane in the southern part of the uplift is oriented 142°/ 74°, indicating a subhorizontal shortening direction of 052–232°. Pole-to-cleavage girdle distribution record gentle folding about an average axis oriented 322°, 03°.

Joints in the southern part of the uplift (Figure 30) are similar to those in the north in that they lack evidence of rotation or shear. These joints are kinematically compatible with subhorizontal extension parallel to the anticlinorium trend and subhorizontal shortening perpendicular to the trend. The mean extensional fracture is oriented 065°/ 90°, indicating horizontal extension trending 335°, and compatible with horizontal shortening trending 65°.

Overall the structures in the Potosí uplift (Table 2) suggest a horizontal shortening direction trending ~077° in the northern part of the uplift and ~062° in the southern part. This 15° variance records a systematic difference in strain between the two ends of the uplift.

Table 2. Structural orientation variations in the northern and southern study areas determined by bedding, cleavage, and extensional fractures within Triassic-Jurassic red beds. See Figure 26 for detailed orientations.

Northern Section	
Horizontal shortening axis determined by bedding	078°
Mean cleavage pole trend	069°
Mean joint set strike	071°
Mean barite vein strike	088°
Southern Section	
Horizontal shortening axis determined by bedding	055°
Mean cleavage pole trend	052°
Mean joint set strike	065°
Mean barite vein strike	074°

16.6. Timing of the Potosí Anticlinorium Exhumation

The vitrinite reflectance $\%R_0$ value of 1.92 from the upper part of the Minas Viejas Formation suggests a burial temperature of ~185°C (Barker and Pawlewicz, 1994; Bird et al., 1999). The vitrinite reflectance indicates the burial depth of the Minas Viejas Formation, giving insight into the thickness of the overlying sedimentary package, structurally thickened from thin-skinned folding. At a standard geothermal gradient of 25–30°C/km, the entirety of the Minas Viejas Formation was buried under ~7.5–9 km of sediment, with the underlying red beds buried ≥8.5 km.

Zircons from underlying strata should have fully reset to helium diffusion prior to thick-skinned exhumation. Given that these zircons were fully reset and that thin-skinned shortening could not have exhumed subdécollemont strata, the zircon (U-Th)/He cooling ages must record thick-skinned or younger exhumation.

ZHe dates indicate thick-skinned uplift and exhumation likely initiated in the Paleocene in the south. The southernmost samples passed through the zircon helium closure temperature, ~180–190°C (Reiners et al., 2002, 2004; Wolfe and Stockli, 2010), at ~66 Ma (Figure 34, 35). As uplift propagated northward, the northernmost samples passed through the zircon helium closure temperature in the Eocene at ~49–44 Ma (Figure 34, 35). Timing of the exhumation in southern Potosí uplift coincides with timing of exhumation in the Aramberri uplift to the south, which passed through the zircon helium closure temperature during the Paleocene, ~63–54 Ma. Given the timing estimates for thin-skinned deformation in the Sierra Madre Oriental, (Section

1), the ZHe dates suggests that deformation was likely a progression from thin-skinned to thick-skinned and not two distinct deformation events with a hiatus in between. Thin-skinned shortening and thick-skinned uplift were locally coeval across the orogen, with thin-skinned deformation continuing in the Monterrey Salient while thick-skinned uplift initiated in the Potosí uplift.

17. The Transition between Thin-Skinned Shortening and Thick-Skinned Uplift

Mechanical stratigraphy and significant modification of the décollement during thin-skinned folding required a change in deformation styles to most efficiently continue shortening, resulting in the incision of shortening to deeper structural levels and transition of motion from the décollement within the Jurassic Minas Viejas Formation to a deeper décollement. During thin-skinned folding, significant flow away from synclinal keels into anticlinal hinges resulted in structural thinning of the Minas Viejas evaporite. The southern portion of the uplift, relative to the northern portion, consists primarily of calcareous shale and carbonate rather than evaporite in the basal décollement, and structural thinning resulted in the elimination of a planar basal weak zone, essentially strengthening the décollement. This modification of décollement mechanical stratigraphy is most striking in Cañón Santa Barbara where exposures of Triassic-Jurassic red beds are in structural contact of the Río de San José Member, and only carbonate appears to be present between the red beds and the Jurassic La Casita Formation, suggesting salt welding through extensive evacuation of evaporite within the synclinal keel of Synclinal Cienuguillas (Plate 1).

The (U-Th)/He zircon cooling dates across the uplift suggest that thick-skinned exhumation initiated in the south ~66 Ma and propagated to the north ~49–44 Ma (Figure 34, 35). This transition from thin-skinned to thick-skinned was a progressive evolution of deformation, not two distinct events (Section 16.6). The onset of thick-skinned exhumation began in the south during the Paleocene as a result of a stronger thin-skinned décollement due to the presence of the Río de San José Member of the Minas Viejas Formation and substantially thinner evaporite intervals in the basal Minas Viejas Formation (Section 9.1). This exhumation resulted in the end of thin-skinned deformation during uplift. As thick-skinned uplift progressed in the south, the weaker décollement to the north continued to accommodate thin-skinned shortening coeval with thick-skinned shortening, resulting in continued translation of overburden strata towards the foreland as a result of a thicker evaporite sequence. Regional strain variations across the Sierra Madre Oriental are well-recorded, with the extent and thickness of the evaporite exerting the primary control on strain. Where this variation is most apparent is in the development of the Monterrey Salient; thick intervals of Jurassic evaporite near Monterrery created a weak décollement, allowing thin-skinned shortening to propagate farther laterally (Marrett and Aranda-García, 2001). Development of the salient rotated the regional stress fields, with shortening to the NW of the salient oriented N–S, and shortening to the SE of the salient oriented E–W. Within the Potosí uplift, thick-skinned uplift rotated the overall local stress field clockwise about a vertical axis as translation of overburden strata above the stronger décollement to the south was more limited. Thick-skinned exhumation propagated northward, where the clockwise rotation of the maximum horizontal stress direction resulted in more ENE-

directed shortening. Eventually, thick-skinned uplift in the north progressed to a point in which thin-skinned shortening could not be accommodated, and exhumation began in the Eocene.

It is also possible that during continued thin-skinned shortening on a much larger scale, the development of the Monterrey Salient created a regional clockwise rotation after the formation of the Potosí anticlinorium, resulting in the ~15° vertical rotation between the northern and southern portions of the uplift. Overburden folds would have also undergone this rotation. However, based on published regional maps (SGM, 2010a, 2010b, 2010c) and measured overburden folds within this study, there is no evidence of a systematic orientation difference between overburden folds in the northern and southern portions of the Potosí uplift.

To summarize, while thick-skinned exhumation occurred to the south in the Paleocene with shortening directed toward ~62°, thin-skinned shortening continued in the north. As thick-skinned exhumation propagated northward in the Eocene, the shortening direction rotated clockwise to ~77°, likely a result of the along-strike differences in the strength of the décollement.

Thermochronometric analysis of Triassic-Jurassic red beds and relative timing of structural features of the thick-skinned Potosí uplift suggests a continuous progression of deformation from thin-skinned shortening to thick-skinned uplift. I can only speculate as to the existence or degree of which the deeper décollement located structurally below the Triassic-Jurassic red beds was active during previous thin-skinned deformation, but given the geometry and extent of thick-skinned shortening during the Potosí uplift, a deeper décollement is the most likely cause of the development and exhumation of the Potosí anticlinorium. In many ways, this proposed structural model for the Potosí uplift is similar to models for the Jura Mountains in the French-Swiss Alps, where Triassic evaporite hosting a thin-skinned shear zone has subsequently

been cut by thick-skinned uplift through reactivation of inherited rift structures above a deeper décollement driven by crustal underplating (Lacombe and Bellahsen, 2016). While the regional variations in the Potosí uplift are likely the result of along-strike changes in décollement mechanical stratigraphy across the uplift, the fundamental cause of the transition to thick-skinned shortening was the loss of a continuous planar weak zone in the décollement during thin-skinned folding. Thus, transitions in deformational styles (e.g., thin-skinned shortening to thick-skinned uplift), may be an inevitable result of a continuous progressive shortening and subsequent thinning in evaporite décollements, and may not necessarily reflect a shift in tectonic boundary conditions (e.g., changes in subducting slab geometry). The effect of décollement mechanical stratigraphy is evident by continued thin-skinned deformation in the Monterrey salient into the Eocene, where the evaporite sequence is substantially thicker than to the south (Fitz-Díaz et al., 2016, 2017). Thin-skinned evaporite décollements may inherently contain an upper limit of shortening (based on thickness of the evaporite interval) before decreased efficiency results in a change in the style of deformation.

CONCLUSION

The Potosí uplift in the Sierra Madre Oriental records evidence of progressive deformation, transitioning from thin-skinned folding above a décollement and development of a fold-thrust belt to thick-skinned uplift involving sub-décollement strata in the early Paleogene. This transition was the result of changes in mechanical stratigraphy, wherein modification of the evaporite décollement during thin-skinned folding locally eliminated planar weak zones and exhausted its ability to efficiently translate overburden strata, resulting in incision of shortening to deeper structural levels.

Differences in timing and shortening directions during the thick-skinned uplift were most likely the product of stratigraphic variations between the northern and southern parts of the uplift, with a stronger thin-skinned décollement to the south causing thick-skinned uplift to begin there in the early Paleocene and migrate to the north. During this migration, thin-skinned folding and foreland-propagation of the overburden continued in the north, locally rotating the stress field clockwise due to the strain being relatively “pinned” to the south. This along-strike variation resulted in shortening differences with trends of ~62° to the south and ~77° to the north.

Thick-skinned uplift was achieved through the development of the El Alamar anticlinorium, a broad ENE-vergent fold within the Triassic-Jurassic red beds of the El Alamar and La Joya Formations. This anticlinorium most likely formed above a thick-skinned décollement, with widespread minor axis-parallel extension associated with barite mineralization during the late-stages of folding. These extensional structures were activated as bending-moment faults, cutting through pre-existing thrust faults, during or after extensive barite mineralization.

REFERENCES

Allmendinger, R., 2016, Faultkin:

Allmendinger, R., 2019, Stereonet:, http://www.geo.cornell.edu/geology/faculty/RWA/programs/stereonet.html.

Allmendinger, R.W., Cardozo, N., and Fisher, D., 2011, Structural geology algorithms: Vectors and tensors:

Altman, D.G., and Bland, J.M., 2005, Standard deviations and standard errors: BMJ, v. 331.

Anderson, T.H., McKee, J.W., and Jones, N.W., 1991, A northwest trending, Jurassic fold nappe, northernmost Zacatecas, Mexico: Tectonics, v. 10, p. 383–401.

Barboza-Gudiño, J.R., Molina-Garza, R.S., and Lawton, T.F., 2012, Sierra de Catorce : Remnants of the ancient western equatorial margin of Pangea in central Mexico: The Geological Society of America, Field Guide, v. 25, p. 1–18, doi:10.1130/2012.0025(01).

Barboza-Gudiño, J.R., Zavala-Monsiváis, A., Venegas-Rodríguez, G., and Barajas-Nigoche, L.D., 2010, Late Triassic stratigraphy and facies from northeastern Mexico: Tectonic setting and provenance: Geosphere, v. 6, p. 621–640, doi:10.1130/ges00545.1.

Barker, C.E., and Pawlewicz, M.J., 1994, Calculation of Vitrinite Reflectance from Thermal Histories and Peak Temperatures: ACS Symposium Series, v. 570, p. 216–229.

Barragán, R., and Maurrasse, F.J.M.R., 2008, Lower Aptian (Lower Cretaceous) ammonites from the basal strata of the La Peña formation of Nuevo León State, northeast Mexico: biochronostratigraphic implications: Revista Mexicana de Ciencias Geologicas, v. 25, p. 145–157.

Belcher, R.C., 1979, Depositional Environments , Paleomagnetism , and Tectonic Significance of Huizachal Red Beds (Lower Mesozoic), Northeastern Mexico: University of Texas at Austin.

Berkeley Geochronology Center, 2011, Isoplot:

Bird, K.J., Burruss, R.C., and Pawlewicz, M.J., 1999, The Oil and Gas Resource Potential of the 1002 Area, Arctic National Wildlife Refuge, Alaska, by ANWR Assessment Team, U.S. Geological Survey Open File Report 98-34; Chapter VR - Thermal Maturity.:

Bradley, D.C., and Kidd, W.S.F., 1991, Flexural extension of the upper continental crust in collisional foredeeps: Geological Society of America Bulletin, v. 103, p. 1416–1438.

Campa U., M.F., 1985, The Mexican thrust belt: Tectonostratigraphic terranes of the circum-Pacific region, v. 1, p. 299–313.

Cardott, B.J., 2012, Introduction to Vitrinite Reflectance as a Thermal Maturity Indicator (Lecture), *in* Search and Discovery, p. 823–830, doi:10.1520/D7708-11.

Centeno-García, E., 2017, Mesozoic tectono-magmatic evolution of Mexico: An overview: Ore Geology Reviews, v. 81, p. 1035–1052, doi:10.1016/j.oregeorev.2016.10.010.

Cross, G.E., 2012, Evaporite deformation in the Sierra Madre Oriental, northeastern Mexico : décollement kinematics in an evaporite-detached thin-skinned fold belt: The University of Texas at Austin, 547 p., https://repositories.lib.utexas.edu/handle/2152/ETD-UT-2012-05-5877.

Cuéllar-Cárdenas, M.A., Nieto-Samaniego, A.F., Levresse, G., Alaniz-Álvarez, S.A., Solari, L., Ortega-Obregón, C., and López-Martínez, M., 2012, Límites temporales de la deformación por acortamiento Laramide en el centro de México: Revista Mexicana de Ciencias Geologicas, v. 29, p. 179–203, doi:10.13140/RG.2.1.4459.2724.

Davis, M.H., 2005, The Tectonics of Tranquitas: A Field Study of Rift through Passive Margin Development and Laramide Deformation in Triassic and Jurassic Strata of the Sierra Madre Oriental, NE Mexico: University of Texas at Austin.

Davis, D.M., and Engelder, T., 1985, The role of salt in fold-and-thrust belts: Tectonophysics, v. 119, p. 67–88, doi:10.1016/0040-1951(85)90033-2.

Dickinson, W.R., and Snyder, W.S., 1978, Plate tectonics of the Laramide orogeny: GSA Memoir, v. 151, p. 355–366, doi:10.1130/MEM151-p355.

Dodson, M.H., 1973, Closure temperature in cooling geochronological and petrological systems: Contrib. Mineral. Petrol., v. 40, p. 259–274.

Eguiluz de Antuñano, S., Aranda García, M., and Marrett, R., 2000, Tectonica de la Sierra Madre Oriental, Mexico: Boletin de la Sociedad Geologica Mexicana, v. 53, p. 1–26.

Esri, 2017, Arcmap:, https://www.esri.com/en-us/arcgis/about-arcgis/overview.

Fiorini, E., and Tibaldi, A., 2012, Quaternary tectonics in the central Interandean Valley , Ecuador : Fault-propagation folds , transfer faults and the Cotopaxi Volcano: Global and Planetary Change, v. 90–91, p. 87–103, doi:10.1016/j.gloplacha.2011.06.002.

Fischer, M.P., and Jackson, P.B., 1999, Stratigraphic controls on deformation patterns in fault-related folds: A detachment fold example from the Sierra Madre Oriental, northeast Mexico: Journal of Structural Geology, v. 21, p. 613–633, doi:10.1016/S0191-8141(99)00044-9.

Fitz-Díaz, E., Hall, C.M., and van der Pluijm, B.A., 2016, XRD-based40Ar/39Ar age correction for fine-grained illite, with application to folded carbonates in the Monterrey Salient (northern Mexico): Geochimica et Cosmochimica Acta, v. 181, p. 201–216,

doi:10.1016/j.gca.2016.02.004.

Fitz-Díaz, E., Lawton, T.F., Juárez-Arriaga, E., and Chávez-Cabello, G., 2017, The Cretaceous-Paleogene Mexican orogen: Structure, basin development, magmatism and tectonics: Earth-Science Reviews, doi:10.1016/j.earscirev.2017.03.002.

Fletcher, P., and Gay, N.C., 1971, Analysis of Gravity Sliding and Orogenic Translation: Discussion: Geological Society of America Bulletin, v. 82, p. 2677–2682, doi:10.1130/0016-7606(1971)82[2677:aogsao]2.0.co;2.

Götte, M., 1988, Estudio geologico - Estructural de Galeana/N.L (Mexico) y sus alrededores: , p. 61–87.

Götte, M., 1990, Halotektonische Deformationsprozesse in Sulfatgesteinen der Minas Viejas-Formation (Ober- Jura) in der Sierra Madre Oriental, Nordost-Mexiko: University of Darmstadt.

Gray, G.G., and Lawton, T.F., 2011, New constraints on timing of Hidalgoan (Laramide) deformation in the Parras and La Popa basins, NE Mexico: Boletin de la Sociedad Geologica Mexicana, v. 63, p. 333–343, doi:10.18268/BSGM2011v63n2a13.

Gray, G.G., Pottorf, R.J., Yurewicz, D.A., Mahon, K.I., Pevear, D.R., and Chuchla, R.J., 2001, Thermal and chronological record of syn- to post-Laramide burial and exhumation, Sierra Madre Oriental, Mexico: C. Bartolini, R. T. Buffler, and A. Cantu-Chapa, eds., The western Gulf of Mexico Basin: Tectonics, sedimentary basins, and petroleum systems: AAPG Memoir 75, v. 75, p. 159–181.

Henry, P., Jouniaux, L., Screaton, E.J., Hunze, S., and Saffer, D.M., 2003, Anisotropy of electrical conductivity record of initial strain at the toe of the Nankai accretionary wedge: Journal of

Geophysical Research: Solid Earth, v. 108, p. 1–12, doi:10.1029/2002jb002287.

Higuera-Díaz, I.C., Fischer, M.P., and Wilkerson, M.S., 2005, Geometry and kinematics of the Nuncios detachment fold complex: Implications for lithotectonics in northern Mexico: Tectonics, v. 24, p. 1–19, doi:10.1029/2003TC001615.

Holliday, D.W., 1970, The petrology of secondary gypsum rocks: A review: Journal of Sedimentary Petrology, v. 40, p. 734–744.

Huízar-Alvarez, R., and Oropeza-Orozco, O., 1989, Geomorfología kárstica de la región de Galeana, estado de Nuevo León: Revista del Instituto de Geología UNAM, v. 8, p. 71–83.

Humphrey, W.E., and Díaz, T., 2003, Jurassic and Lower Cretaceous Stratigraphy and Tectonics of Northeast Mexico: 100–104 p.

Jordan, P., 1992, Evidence for large-scale decoupling in the Triassic evaporites of Northern Switzerland: an overview: Eclogae Geologicae Helvetiae, v. 85, p. 677–693.

Jowett, E.C., and Cathles, L., 1993, Predicting Depths of Gypsum Dehydration in Evaporitic Sedimentary Basins: AAPG Bulletin, v. 77, doi:10.1306/BDFF8C22-1718-11D7-8645000102C1865D.

Kesler, S.E., Jones, L.M., and Ruiz, J., 1988, Strontium and sulfur isotope geochemistry of the Galeana Barite district, Nuevo Leon, Mexico: Economic Geology, v. 83, p. 1907–1917, doi:10.2113/gsecongeo.83.8.1907.

Kroeger, K.F., and Stinnesbeck, W., 2003, The Minas Viejas Formation (Oxfordian) in the Area ofGaleana, Northeastern Mexico: Significance ofSyndepositional Volcanism and Related Barite Genesis in the Sierra Madre Oriental: AAPG Memoir, v. 79, p. 515–528.

Lacombe, O., and Bellahsen, N., 2016, Thick-skinned tectonics and basement-involved fold-

thrust belts: Insights from selected Cenozoic orogens: Geological Magazine, v. 153, p. 763–810, doi:10.1017/S0016756816000078.

Laubach, S.E., and Ward, M.E., 2006, Diagenesis in porosity evolution of opening-mode fractures, Middle Triassic to Lower Jurassic La Boca Formation, NE Mexico: Tectonophysics, v. 419, p. 75–97, doi:10.1016/j.tecto.2006.03.020.

Lawton, T.F., Bradford, I.A., Vega, F.J., Gehrels, G.E., and Amato, J.M., 2009, Provenance of Upper Cretaceous-Paleogene sandstones in the foreland basin system of the Sierra Madre Oriental, northeastern Mexico, and its bearing on fluvial dispersal systems of the Mexican Laramide Province: Bulletin of the Geological Society of America, v. 121, p. 820–836, doi:10.1130/B26450.1.

Liu, L., Gurnis, M., Seton, M., Saleeby, J., Müller, R.D., and Jackson, J.M., 2010, The role of oceanic plateau subduction in the Laramide orogeny: Nature Geoscience, v. 3, p. 353–357, doi:10.1038/ngeo829.

Livio, F., Ketterman, M., Reicherter, K., and Urai, J.L., 2019, Growth of bending-moment faults due to progressive folding: Insights from sand-box models and paleoseismological implications: Geomorphology, v. 326, p. 152–166.

Livio, F., Kettermann, M., Reicherter, K., and Urai, J.L., 2018, Geomorphology Growth of bending-moment faults due to progressive folding : Insights from sandbox models and paleoseismological implications: Geomorphology, doi:10.1016/j.geomorph.2018.02.012.

Marrett, R.A., and Allmendinger, R.W., 1990, Kinematic analysis of fault-slip data: Journal of Structural Geology, v. 12, p. 973–986.

Marrett, R., and Aranda-García, M., 2001, Regional Structure of the Sierra Madre Oriental Fold-

Thrust Belt , Mexico: Genesis and Controls of Reservoir-scale Carbonate Deformation, Monterrey Salient, Mexico; Guidebook 28, p. 31–55.

Marshall, J.D., and Pirrie, D., 2013, Carbonate concretions-explained: Geology Today, v. 29, p. 53–62, doi:10.1111/gto.12002.

Meiburg, P., Chapa-Guerrero, J.R., Grotehusmann, I., Kustusch, T., Lentzy, P., Leon-Gomez, H. de, and Mansilla-Teran, M.A., 1987, El basamento precretácio de Aramberri – estructura clave para comprender el décollement de la cubierta jurásica/cretácica de la Sierra Madre Oriental, México? Actas de la Facultad de Ciencias de la Tierra de la Universidad Autonoma de Nuevo Leon Linares, v. 2, p. 15–22.

Michalzik, D., 1991, Oriental (NE Mexico) and its relation to the early opening of the Gulf of Mexico: v. 71, p. 243–259.

Michalzik, D., and Schumann, D., 1994, Lithofacies relation and paleoecology of a Late Jurassic to Early Cretaceous fan delta to shelf depositional system in the Sierra Madre Oriental of north-east Mexico: Sedimentology, v. 41, p. 463–477.

Mixon, R.B., 1963, Geology of the Huizachal Redbeds, Sierra Madre Oriental, Mexico. Recommended Citation: Louisiana State University, https://digitalcommons.lsu.edu/cgi/viewcontent.cgi?article=1818&context=gradschool_disstheses.

Moor, A., 1980, Stratigraphy and Structure of Potosi Anticline, Nuevo Leon, Mexico: University of Texas at Austin.

Ocampo-Díaz, Y.Z.E., Jenchen, U., and Guerrero-Suastegui, M., 2008, Facies y sistemas de depósito del miembro arenoso Galeana (Formación Taraises, Cretácico inferior, NE de

México): Revista Mexicana de Ciencias Geologicas, v. 25, p. 438–464.

Ocampo-Díaz, Y.Z.E., Pinzon-Sotelo, M.P., Chávez-Cabello, G., Ramírez-Díaz, A., Martínez-Paco, M., Velasco-Tapia, F., Guerrero-Suastegui, M., and Barboza-Gudiño, J.R., 2016, Propuesta nomenclatural y análisis de procedencia de la Formación Concepción del Oro (antes Formación Caracol): Implicaciones sobre la evolución tectónica del sur de Norteamérica durante el Cretácico Tardío: Revista Mexicana de Ciencias Geologicas, v. 33, p. 3–33.

Padilla y Sánchez, R.J., 1978, Bosquejo Geologico estructural De La Sierra Madre Oriental: Universidad Nacional Autónoma de México, Instituto de Geologia, v. 2, p. 45–54.

Padilla y Sánchez, R.J., 1982, Geologic Evolution of the Sierra Madre Oriental Between Linares, Concepcion Del Oro, Saltillo, and Monterrey, Mexico: The University of Texas at Austin, doi:10.1016/j.jaci.2012.05.050.

Padilla y Sánchez, R.J., 1985, Las estructuras de la Curvatura de Monterrey, estados de Coahuila, Nuevo Leon, Zacatecas y San Luis Potosi: Univ. Nal. Autón. México, Inst. Geología, v. 6, p. 1–20.

Prior, M.G., Singleton, J.S., Williams, S.A., and Mavor, S., 2018, Timing of thick-skinned exhumation in the Potosi uplift, Sierra Madre Oriental, northeastern Mexico, *in* Abstracts with Programs - GSA 2018, Indianapolis.

Prior, M.G., Stockli, D.F., and Singleton, J.S., 2016, Miocene slip history of the Eagle Eye detachment fault, Harquahala Mountains metamorphic core complex, west-central Arizona: Tectonics, v. 35, p. 1913–1934, doi:10.1002/2016TC004241.

Ramírez-Peña, C.F., and Chávez-Cabello, G., 2017, Age and evolution of thin-skinned deformation in Zacatecas, Mexico: Sevier orogeny evidence in the Mexican Fold-Thrust

Belt: Journal of South American Earth Sciences, v. 76, p. 101–114, doi:10.1016/j.jsames.2017.01.007.

Reid, B.H., and Marrett, R., 2002, Structural analysis of the tranverse zone, part of the San Julian uplift, Sierra Madre Oriental, northern Zacatecas, Mexico:

Reiners, P.W., Farley, K.A., and J., H.H., 2002, He diffusion and (U-Th)/He thermochronometry of zircon: Initial results from Fish Canyon Tuff and Gold Butte: Tectonophysics, v. 349, p. 297–308.

Reiners, P.W., Spell, T., Nicolesc, S., and Zanetti, K., 2004, Zircon (U–Th)/He thermochronometry: He diffusion and comparisons with Ar-40/ Ar-39 dating: Geochimica et Cosmochimica Acta, v. 68, p. 1857–1887.

Rubio-Cisneros, I.I., and Lawton, T.F., 2011, Detrital zircon U-Pb ages of sandstones in continental red beds at Valle de Huizachal, Tamaulipas, NE Mexico: Record of Early-Middle Jurassic arc volcanism and transition to crustal extension: Geosphere, v. 7, p. 159–170, doi:10.1130/ges00567.1.

SGM, 2010a, Galeana G14-C56:

SGM, 2010b, Iturbide G14-C67:

SGM, 2010c, San Jose de Raices G14-C66:

Shearman, D.J., Mossop, G., Dunsmore, H., and Martin, M., 1972, Origin of gypsum veins by hydraulic fracture: Transactions of the Institution of Mining and Metallurgy, v. 81, p. 149–155.

Shimamoto, T., and Logan, J.M., 1981, Effects of Simulated Fault Gouge on the Sliding Behavior of Tennessee Sandstone: Nonclay Gouges: Journal of Geophysical Research, v. 86, p. 2902–

2914.

Stewart, S.A., 1999, Geometry of thin-skinned tectonic systems in relation to detachment layer thickness in sedimentary basins: Tectonics, v. 18, p. 719–732, doi:10.1029/1999TC900018.

Stewart, J.H., 1998, Regional characteristics, tilt domains, and extensional history of the late Cenozoic Basin and Range province, western North America: Geological Society of America Special Paper, v. 323, p. 47–74.

Tardy, M., Longoria, J.F., Martínez-Reyes', J., Mitre S., L.M., Patiño A., M., Padilla y Sánchez, R.J., and Ramírez R., C., 1975, Observaciones generales sobre la estructura de la Sierra Madre Oriental: La aloctonia del conjunto cadena alta-altiplano central, Entre Torreon, Coah. y San Luis Potosi, S.L.P. Mexico.: Revista del Instituto de Geología UNAM, v. 75, p. 1–11.

Testa, G., and Lugli, S., 2000, Gypsum-anhydrite transformations in Messinian evaporites of central Tuscany (Italy): Sedimentary Geology, v. 130, p. 249–268, http://www.sciencedirect.com/science/article/pii/S0037073899001189/pdfft?md5=54cdaf37c2f0ba6cc500964cbed42828&pid=1-s2.0-S0037073899001189-main.pdf%5Cnpapers2://publication/uuid/A29DA7B8-AB09-4008-B6C7-AE0B38986685.

Tibaldi, A., and Bonali, F.L., 2018, Contemporary recent extension and compression in the central Andes: Journal of Structural Geology, v. 107, p. 73–92, doi:10.1016/j.jsg.2017.12.004.

Vega-Vera, F.J., Mitre-Salazar, L.M., and Martínez-Hernández, E., 1989, Contribución al conocimiento de la estratigrafía del grupo difunta (Cretácico superior-terciario) en el noreste de Mexico: Univ. Nal. Autón. México, Inst. Geología, v. 8, p. 179–187.

Vollmer, F.W., 1990, An application of eigenvalue methods to structural domain analysis:

Bulletin of the Geological Society of America, v. 102, p. 786–791, doi:10.1130/0016-7606(1990)102<0786:AAOEMT>2.3.CO;2.

Vollmer, F.W., 2018, EllipseFit:

Warren, J.K., 2006, Evaporites: Sediments, resources and hydrocarbons: 1–1035 p., doi:10.1007/3-540-32344-9.

Whitaker, A.E., and Bartholomew, M.J., 1999, Layer parallel shortening: A mechanism for determining deformation timing at the junction of the central and southern Appalachians: American Journal of Science, v. 299, p. 238–254, doi:10.2475/ajs.299.3.238.

Wolfe, M.R., and Stockli, D.F., 2010, Zircon (U-Th)/He thermochronometry in the KTB drill hole, Germany, and its implications for bulk He diffusion kinetics in zircon: Earth Planet. Sci. Lett., v. 295, p. 69–82.

Yonkee, W.A., and Weil, A.B., 2015, Tectonic evolution of the Sevier and Laramide belts within the North American Cordillera orogenic system: Earth-Science Reviews, v. 150, p. 531–593, doi:10.1016/j.earscirev.2015.08.001.

Zell, P., Beckmann, S., Stinnesbeck, W., and Götte, M., 2015, Mollusks of the Upper Jurassic (upper Oxfordian-lower Kimmeridgian) shallow marine Minas Viejas Formation, northeastern Mexico: Journal of South American Earth Sciences, v. 62, p. 92–108, doi:10.1016/j.jsames.2015.05.006.

Zhou, Y., 2005, Structural evolution of the Sierra Madre Oriental fold-thrust belt , east central Mexico: University of Houston.

Zhou, Y., Murphy, M.A., and Hamade, A., 2006, Structural development of the Peregrina-Huizachal anticlinorium, Mexico: Journal of Structural Geology, v. 28, p. 494–507,

doi:10.1016/j.jsg.2005.11.005.

APPENDICES

Appendix 1: Measurements of fold axial traces from SGM (2010a, 2010b) maps

W (mm)	H (mm)	L (km)	Azimuth
33.69	48.341	1.58	55.13
34.396	55.096	1.74	58.02
26.458	17.738	0.85	33.84
23.283	36.767	1.16	57.66
15.522	13.539	0.55	41.10
29.986	42.427	1.39	54.75
4.41	15.156	0.42	73.78
55.739	90.356	2.84	58.33
7.232	6.826	0.27	43.35
7.056	43.224	1.17	80.73
19.403	45.637	1.33	66.97
35.278	134.666	3.72	75.32
0	17.738	0.47	90.00
6.35	17.823	0.51	70.39
25.047	22.903	0.91	42.44
21.519	20.321	0.79	43.36
26.458	48.304	1.47	61.29
6.703	40.726	1.10	80.65
15.169	40.641	1.16	69.53
21.872	129.501	3.51	80.41
223.387	180.387	7.68	38.92
80.257	161.396	4.82	63.56
90.674	116.843	3.96	52.19
37.394	76.202	2.27	63.86
2.469	38.059	1.02	86.29
6.526	27.983	0.77	103.13
38.453	60.962	1.93	57.76
5.997	22.903	0.63	75.33
10.231	50.802	1.39	78.61
30.692	55.966	1.71	61.26
9.525	45.721	1.25	78.23
1.764	45.636	1.22	87.79
32.103	43.224	1.44	53.40
43.392	68.624	2.17	57.69

W (mm)	H (mm)	L (km)	Azimuth
20.108	27.898	0.92	54.22
26.458	73.704	2.09	70.25
20.461	48.304	1.40	67.04
2.117	27.898	0.75	85.66
47.978	106.683	3.13	65.79
85.019	63.544	2.84	36.77
63.853	66.042	2.46	45.97
22.225	15.24	0.72	34.44
27.517	33.044	1.15	50.21
7.232	19.132	0.55	69.29
32.632	26.589	1.13	39.17
0	7.663	0.20	90.00
50.8	81.282	2.56	58.00
42.333	38.059	1.52	41.96
3.881	43.224	1.16	84.87
14.111	48.219	1.34	73.69
4.233	20.321	0.56	78.23
25.047	40.641	1.28	58.35
13.053	15.24	0.54	49.42
7.056	15.24	0.45	65.16
2.117	17.738	0.48	83.19
2.117	27.898	0.75	94.34
7.761	81.283	2.18	84.55
82.374	111.848	3.72	53.63
10.231	29.154	0.83	70.66
13.758	21.781	0.69	57.72
7.408	13.78	0.42	61.74
0.882	22.401	0.60	92.25
27.164	36.418	1.22	53.28
17.639	19.463	0.70	47.81
2.234	7.761	0.22	73.94
13.17	25.988	0.78	63.13
6.232	6.938	0.25	48.07
11.759	29.046	0.84	67.96
8.584	31.632	0.88	74.82
22.107	54.563	1.57	67.94
0.823	33.031	0.88	88.57
16.228	24.342	0.78	56.31
23.813	21.696	0.86	42.34
33.044	32.22	1.23	44.28

W (mm)	H (mm)	L (km)	Azimuth
6.291	18.227	0.52	70.96
0	20.285	0.54	90.00
7.585	26.471	0.74	74.01
1.764	19.452	0.52	84.82
2.646	10.076	0.28	75.29
7.849	14.111	0.43	60.92

Total:	856.278	1488.6	**0.71**	60.09

Appendix 2: All reduced (U-Th)/He sample data

San Luis Potosi Uplift Samples															
Sample	**Age, Ma**	**err., Ma**	**U (ppm)**	**Th (ppm)**	**147Sm (ppm)**	**[U]e**	**Th/U**	**He (nmol/g)**	**mass (ug)**	**Ft**	**ESR**	**Mean**	**Std Dev**	**2SE**	**n used**
zSMO18-1-1	46.9	3.75	77.9	67.6	1.3	93.4	0.87	20.0	21.10	0.84	76.18	**49.0**	**10.2**	**10.2**	**(4/5)**
zSMO18-1-2	41.5	3.32	28.5	29.1	2.5	35.2	1.02	6.4	11.48	0.80	62.06				
zSMO18-1-3	63.9	5.11	89.1	64.9	2.3	104.1	0.73	30.3	20.64	0.84	74.97				
zSMO18-1-4	43.7	3.49	60.6	32.7	1.6	68.2	0.54	14.0	35.33	0.87	93.40				
zSMO18-1-5*	101.1	8.09	154.8	71.1	2.3	171.2	0.46	78.4	16.54	0.83	71.80				
zSMO18-4-1	74.5	5.96	167.4	135.6	1.2	198.6	0.81	63.3	7.73	0.79	56.49	**66.4**	**13.2**	**11.8**	**(5/5)**
zSMO18-4-2	47.2	3.78	159.6	104.2	1.2	183.6	0.65	39.0	16.05	0.83	70.67				
zSMO18-4-3	77.6	6.21	205.4	159.3	0.0	242.0	0.78	77.5	5.94	0.76	49.03				
zSMO18-4-4	58.0	4.64	235.4	243.6	6.6	291.5	1.03	76.2	15.70	0.83	71.14				
zSMO18-4-5	74.7	5.97	102.0	70.7	1.1	118.3	0.69	38.0	8.33	0.79	57.22				
zSMO18-6-1	41.6	3.33	213.6	102.2	0.8	237.1	0.48	43.7	11.39	0.82	65.21	**55.9**	**10.2**	**9.1**	**(5/5)**
zSMO18-6-2	58.7	4.70	155.9	89.6	0.6	176.5	0.57	46.8	15.32	0.83	71.80				
zSMO18-6-3	65.5	5.24	145.5	90.3	1.5	166.3	0.62	49.8	19.06	0.84	76.88				
zSMO18-6-4	64.4	5.16	223.8	171.6	3.0	263.3	0.77	76.6	15.42	0.83	71.93				
zSMO18-6-5	49.4	3.95	94.4	72.2	0.8	111.0	0.77	24.3	11.79	0.82	65.99				
zS156-1	55.7	4.46	210.7	88.7	1.5	231.1	0.42	59.3	25.65	0.85	80.64	**49.4**	**9.1**	**10.5**	**(3/4)**
zS156-2	53.5	4.28	749.4	236.9	8.7	804.0	0.32	175.1	4.35	0.75	46.60				
zS156-3	38.9	3.11	149.1	91.0	0.0	170.0	0.61	27.7	5.59	0.77	52.44				
zS156-4*	100.0	8.00	115.7	57.1	0.0	128.9	0.49	54.9	6.83	0.78	54.43				
zSMO17-5-1-1	44.4	3.55	263.7	78.7	1.8	281.8	0.30	55.1	10.63	0.81	63.36	**43.8**	**3.5**	**3.2**	**(5/5)**
zSMO17-5-1-2	41.0	3.28	509.3	210.8	21.2	557.9	0.41	98.9	8.53	0.80	58.59				
zSMO17-5-1-3	47.8	3.82	70.6	38.0	7.3	79.4	0.54	16.9	13.06	0.82	67.36				
zSMO17-5-1-4	46.4	3.71	214.6	58.3	1.5	228.0	0.27	44.4	6.49	0.78	51.88				
zSMO17-5-1-5	39.4	3.16	128.7	71.5	-3.0	145.1	0.56	24.9	9.37	0.80	60.91				
zSMO17-5-43-1	73.9	5.91	158.8	56.8	0.0	171.9	0.36	54.3	7.90	0.79	55.80	**59.7**	**10.2**	**9.1**	**(5/5)**
zSMO17-5-43-2	47.4	3.79	252.1	136.9	2.0	283.6	0.54	57.7	9.49	0.79	57.22				
zSMO17-5-43-3	60.2	4.82	53.3	19.8	0.6	57.8	0.37	15.7	16.39	0.83	69.91				
zSMO17-5-43-4	53.2	4.26	90.1	44.6	0.6	100.4	0.49	24.0	15.70	0.83	69.77				
zSMO17-5-43-5	63.8	5.11	100.8	44.6	0.7	111.0	0.44	31.9	14.02	0.83	70.25				

zSMO17-MVSS-1	41.6	3.33	75.9	36.9	2.7	84.4	0.49	15.7	14.18	0.82	68.04	**48.6**	**4.4**	**3.9**	**(5/5)**
zSMO17-MVSS-2	51.6	4.13	305.1	206.4	4.1	352.7	0.68	78.8	9.28	0.80	59.32				
zSMO17-MVSS-3	52.2	4.18	107.7	70.7	1.6	124.0	0.66	28.7	11.85	0.82	66.18				
zSMO17-MVSS-4	47.2	3.78	106.7	70.2	0.7	122.8	0.66	25.8	12.73	0.82	66.93				
zSMO17-MVSS-5	50.5	4.04	142.4	66.8	1.5	157.8	0.47	35.5	12.32	0.82	66.83				
zSMO17-5-29-1*	14.9	1.19	374.8	170.2	6.4	414.0	0.45	24.0	2.95	0.72	41.02	**42.5**	**3.5**	**3.5**	**(4/8)**
zSMO17-5-29-2*	30.4	2.43	214.3	93.6	4.9	235.9	0.44	30.0	5.85	0.77	52.19				
zSMO17-5-29-3*	12.8	1.03	249.7	113.7	5.0	275.9	0.46	14.8	5.68	0.77	51.18				
zSMO17-5-29-4*	23.4	1.87	145.6	72.7	2.4	162.4	0.50	16.3	7.97	0.79	57.55				
zSMO17-5-29-5	44.9	3.59	55.2	50.2	5.0	66.8	0.91	12.8	7.59	0.78	55.28				
SMO17-5-29-6	38.4	3.07	80.7	41.3	3.3	90.3	0.51	14.9	8.34	0.79	57.67				
SMO17-5-29-7	40.9	3.27	86.0	38.0	2.2	94.8	0.44	16.8	8.58	0.80	59.19				
SMO17-5-29-8	45.8	3.67	101.4	49.2	0.0	112.7	0.49	19.8	2.69	0.71	39.26				
Aramberri Uplift Samples															
Sample	**Age, Ma**	**err., Ma**	**U (ppm)**	**Th (ppm)**	**147Sm (ppm)**	**[U]e**	**Th/U**	**He (nmol/g)**	**mass (ug)**	**Ft**	**ESR**	**Mean**	**Std Dev**	**2SE**	**n used**
zS493-2	56.9	4.55	57.8	29.0	2.1	64.5	0.50	16.4	13.39	0.83	68.76	**62.7**	**14.1**	**12.7**	**(5/5)**
zS493-4	53.0	4.24	76.7	58.5	13.3	90.2	0.76	19.9	6.34	0.77	51.28				
zS493-5	48.2	3.86	153.8	32.4	2.8	161.3	0.21	34.2	10.24	0.81	62.68				
zS493-1	75.7	6.06	388.5	139.0	3.5	420.5	0.36	136.8	8.12	0.79	56.43				
zS493-3	79.8	6.39	103.7	32.8	4.5	111.3	0.32	39.9	14.55	0.83	68.74				
zSMO18-3-1	72.1	5.77	138.5	69.6	3.1	154.5	0.50	49.9	14.98	0.82	68.20	**53.9**	**13.0**	**11.6**	**(5/5)**
zSMO18-3-2	36.5	2.92	307.7	156.7	3.5	343.8	0.51	54.2	8.15	0.80	58.35				
zSMO18-3-3	50.4	4.03	89.6	45.8	1.3	100.1	0.51	21.7	7.51	0.79	57.10				
zSMO18-3-4	51.7	4.14	504.7	170.1	2.7	543.9	0.34	118.0	7.02	0.77	51.85				
zSMO18-3-5	58.6	4.69	28.4	24.7	3.3	34.1	0.87	8.8	11.52	0.81	64.24				

*indicates aliquots excluded from mean ZHE age calculation

SE=standard error

Ft=alpha ejection correction factor of Farley et al., 1996

[U]e=effective uranium concentration ([U]e=[U]+0.235[Th])

Appendix 3: Vitrinite reflectance analysis

Measurement #	All Data	Indigenous	recycled	inertinite	contamination?
1	0.67	1.71	2.12	2.31	0.67
2	0.71	1.79	2.13	2.33	0.71
3	0.73	1.80	2.13	2.33	0.73
4	0.75	1.81	2.14	2.36	0.75
5	0.77	1.81	2.16	2.42	0.77
6	0.77	1.83	2.16	2.43	0.77
7	0.77	1.85	2.18	2.50	0.77
8	0.79	1.88	2.18	2.52	0.79
2	0.81	1.91	2.20	2.55	0.81
10	0.85	1.92	2.20	2.57	0.85
11	1.71	1.93	2.22	2.60	
12	1.79	1.93	2.23	2.64	
13	1.80	1.94	2.24	2.67	
14	1.81	1.96		2.82	
15	1.81	1.97		2.89	
16	1.83	1.97			
17	1.85	2.00			
18	1.88	2.01			
19	1.91	2.04			
20	1.92	2.05			
21	1.93	2.08			
22	1.93	2.08			
23	1.94				
24	1.96				
25	1.97				
26	1.97				
27	2.00				
28	2.01				
29	2.04				
30	2.05				
31	2.08				
32	2.08				
33	2.12				
34	2.13				
35	2.13				
36	2.14				
37	2.16				
38	2.16				
39	2.18				
40	2.18				
41	2.20				
42	2.20				
43	2.22				
44	2.23				
45	2.24				
46	2.31				
47	2.33				

Measurement #	All Data	Indigenous	recycled	inertinite	contamination?
48	2.33				
49	2.36				
50	2.42				
51	2.43				
52	2.50				
53	2.52				
54	2.55				
55	2.57				
56	2.60				
57	2.64				
58	2.67				
59	2.82				
60	2.89				
Average VR	1.94	1.92	2.18	2.53	0.76
Std. Dev.	0.59	0.10	0.04	0.18	0.05
# of Points	60	22	13	15	10